Galaxy Formation at Redshift $\sim$ 0.75:

A Low Mass Survey & The Role of Environment

by

Chad Greene

A thesis
presented to the University of Waterloo
in fulfillment of the
thesis requirement for the degree of
Master of Science
in
Physics

Waterloo, Ontario, Canada, 2011

I hereby declare that I am the sole author of this thesis. This is a true copy of the thesis, including any required final revisions, as accepted by my examiners.

I understand that my thesis may be made electronically available to the public.

Abstract

The majority of galaxy formation studies which explore beyond local redshifts do not typically probe down to the dwarf galaxy stellar mass range of $\sim 10^9 M_\odot$. Thus trends in the observed evolution or characteristics of galaxy formation at a particular epoch are based upon populations of massive galaxies. However the currently favored Λ-Cold Dark Matter (Λ-CDM) theory is based upon hierarchical clustering and merging of lower mass systems, which proceed to make the higher mass, complex morphology of galaxies we observe. Thus it is clear that within the dwarf galaxy mass regime there should be a significant phase of galaxy formation and evolution. This work aims to uncover the influence of local environment on the formation and evolution of dwarf and massive galaxies beyond local redshift, probing down to a mass range lower than that which has been explored by previous studies.

A previously successful study titled the Redshift One LDSS-3 Emission line Survey (ROLES), released results for a redshift of $z \sim 1$, which compared the [OII] luminosity and galaxy stellar mass functions ([OII] LF and GSMF respectively), star formation rate density (SFRD), and specific star formation rate (sSFR) relations, with a local SDSS dataset. This led to the expansion of the study to lower redshift (this work) which explored low stellar mass galaxies at a redshift of $z \sim 0.75$. This follow-up study referred to as ROLES75 ($z \sim 0.75$) targeted the same two deep fields explored by the $z \sim 1$ study (GOODS-South, MS1054-03 FIRES), which have extensive public photometry. Low mass targets were selected for study by their K-magnitudes ($22.5 < K_{AB} < 24$) leading to a dwarf mass range of $8.5 \lesssim Log(M^*/M_\odot) \lesssim 9.5$, and which were most likely to be within our redshift range ($0.62 < z < 0.885$). Follow-up multi-object spectroscopy targeted the $[\mathrm{OII}]_{\lambda 3727\text{Å}}$ emission line star formation tracer in these targets allowing us to identify and obtain secure spectroscopic redshifts, SED-fit stellar masses and observed [OII] luminosity calibrated star formation rates down to limits of $\mathrm{Log}(M^*/M_\odot) \sim 8.85$ and $\mathrm{SFR} \sim 0.1 M_\odot yr^{-1}$.

Science results presented here are similar to those published by the ROLES $z \sim 1$ study, however we also studied the influence of the high versus low density environment in which the galaxy populations reside. This study confirmed that while the [OII] luminosity was higher in earlier times, environment does not influence galaxy formation at $z \sim 0.75$. The faint-end slope of the [OII] LF, $\alpha \sim 1.25$ measured here, is also observed to become increasingly more steep with increasing redshift. The [OII] luminous GSMF is observed to not have significantly evolved since $z \sim 2.75$, confirming the result of the previous ROLES work. However the impact of environment on the GSMF is apparent in the high mass end where the imprint of structure from the CDFS field enhances the stellar mass function above the field population. There is also weak evidence of a bi-modal [OII] luminous GSMF indicated by an 'upturn' near $\sim 10^9 M_\odot$ in the low density field population. The SFRD

at $z \sim 0.75$ does not confirm the picture presented by the ROLES $z \sim 1$ study where a constant scale factor was applicable to the local SDSS SFRD to obtain the $z \sim 1$ SFRD. The SFRD in the high mass end at $z \sim 0.75$ is lower than would be expected based upon a constant scale factor, while the low stellar mass end exhibits some consistency with this picture. In the high density environment, this dominant SFRD (over the low density field population) is driven by the high density [OII] luminous GSMF in the high stellar mass end, rather than through an enhancement of the SFR. The normalization of the $sSFR - M^*$ relation at $z \sim 0.75$ is found to lie between those corresponding to $z \sim 1$ and present day. There is a subtle 'upturn' in the $sSFR - M^*$ relation confirming this observation which was also present in the ROLES $z \sim 1$ study but not present in the local SDSS $sSFR - M^*$ relation. The sSFR of active galaxies does not depend upon the local density in which they are forming, confirming the same conclusion based upon the [OII] LF. However, there is redshift evolution of the $sSFR - M^*$ relation with respect to local density. The high density $sSFR - M^*$ relation for star forming galaxies was dominant over its low density counterpart at early times, with the opposite the case at present day. There is suggestion of the crossover or rollover transition occurring at $z \sim 0.75$.

Acknowledgements

The ROLES collaboration would like to thank S. Crawford, T. Dahlen, H. Dominguez, M. Franx, S. Juneau, C. Maier, B. Mobasher, L. Pozzetti, E. Vanzella, and S. Wuyts for providing data and useful correspondence throughout the project.

I would like to thank my family and friends for their support during this endeavour. Most importantly I would like to thank my girlfriend whose patience, understanding, and never-ending source of encouragement have made this possible.

Dedication

This is dedicated to the one person who has never shown any regret in supporting my choice to pursue this degree. Without your support along every step of the way this would not have been possible and I thank you from the bottom of my heart.

Table of Contents

List of Tables

List of Figures

Chapter 1

Introduction

We are currently living in an important era of modern astronomy. Observational technology continues to advance at a steady pace allowing us to probe ever deeper into the Universe, seeing it as it was not long after the Big Bang. While initially driven by an expectation of what might be found in a survey region, current studies often continue to lead to unexpected observational discoveries. Physical theories which aim to explain the phenomena we observe have also advanced to a stage where their predictions of a specific observable can be tested with current observational techniques. Modern astronomy is thus beginning a phase transition of moving from observing regions of the universe and asking physical theory to explain what is seen, to a phase of highly tuned testing of very specific predictions made by current, sometimes competing, theories. We are living in a time when modern astronomy is starting to "catch-up" to the method of exploration which has been the standard for nearly a century for its close cousin, particle physics.

Modern astronomical observations suggest that the Universe is the way we see it due to the dark energy - cold dark matter cosmological (Λ-CDM) theory introduced by Blumenthal et al. (1984). This theory is fundamentally hierarchical, with small mass systems merging to form higher mass systems in an ongoing process throughout cosmic time. The theory also depends critically upon two forms of energy/mass, and inflation, all of which are not completely understood to date but limitations on their characteristics do exist which narrow down their possible nature. The first foundational element of the theory is the concept of dark energy which makes up approximately 73% of the energy density of the universe at present time, and is accepted as being the explanation behind the observed accelerated expansion of the universe. The second is the posited existence of cold dark matter - non-relativistic particles which only interact with each other and regular baryonic matter via gravity. Inflation describes the rapid exponential growth of the Universe over a

short period of time, and when combined with dark matter, helps to explain the existence of structure in the Universe.

As mentioned above, the Λ-CDM cosmological theory suggests that structure formation[1] is hierarchical. Shortly after the Big Bang the matter density field would have experienced tiny fluctuations which with the onset of inflation, would have expanded to cosmic scales. The dark matter (DM) component collapsed under gravitational self-interaction, leading to a 'node' and 'filamentary' network of *seed* locations for regular baryonic matter to collapse and condense into. Further collapse of the dark matter eventually led to the formation of dark matter halos consisting of DM particles whose combined gravitational self-attraction is supported by their collective random motions. Over time the DM halos continued to grow through further DM accretion and via mergers of halos in close proximity, all the while their gravitational influence on the regular baryonic matter growing stronger. The gravitational potential wells manifested by the DM halos attracted the baryonic matter, or gas, allowing it to cool and condense 'down into' the potential wells, thus accreting ever more matter forming the first proto-galaxies.

The ongoing processes of halo merging, and dark and regular matter accretion continued to build-up the proto-galaxies consisting of gas embedded in large dark matter halos. As the gas within the dark matter potential well grew in density, the gas itself began to undergo gravitational collapse eventually igniting the first stars and leading to the massive faint galaxies we observe at the most distant redshifts. At this stage of structure formation, complex interactions dominate the evolution of structure in the early universe with observable phenomena *emerging* from these interactions[2]. Through complex interactions, further merging and accretion, and nuclear processes, the galaxies evolved with cosmic time to form the beautiful range of morphologies we observe throughout the universe.

The study of galaxy formation aims to understand these complex interactions and their evolutionary mechanisms in detail. Galaxies residing at nearby redshifts have been observed in great detail by revolutionary surveys such as the Sloan Digital Sky Survey (`http://www.sdss.org`). The *astronomical* number of galaxies observed in the survey verify the picture of a cosmic network of filamentary structure and nodes, as shown in Figure 1.1. But what about earlier epochs? What does the distribution of galaxies look like then? We certainly expect there to be a mass dependence given the hierarchical nature of the Λ-CDM theory, with the more massive galaxies becoming increasingly rare. Indeed this picture is confirmed in many studies (see Wuyts et al., 2011; Cowie & Barger, 2008, for

[1]For an excellent recent review of structure and galaxy formation starting from first principles, the reader is encouraged to read Benson (2010).

[2]The sheer multitude of particles and interactions involved is an N-body problem which is only tractable through the use of empirical relationships rather than attempting to make predictions analytically.

example) where the total number density of high mass galaxies (referred to as the observed total galaxy stellar mass function, or total GSMF) is much lower than that of their lower mass counterparts out to redshift $z \sim 4$ (Marchesini et al., 2009). Does this evolutionary trend in the total GSMF continue to the dwarf galaxy mass scale? Does it matter if the galaxies are actively or passively forming stars? Most certainly it does, as shown in Figure 11 of Pozzetti et al. (2009, for example) where the GSMFs for each of the total, actively star forming, and passive galaxy populations are presented as a function of redshift. Clearly the high mass end of the total GSMF is dominated by the passive galaxy population which quickly falls off toward low stellar mass, whereas in the low stellar mass regime the actively star forming GSMF begins to dominate near $10^{10} M_{\odot}$. Bundy et al. (2006) show that the contribution of the passive GSMF to the total GSMF increases toward lower stellar masses with decreasing redshift. Unfortunately, for higher redshifts, studies like this were unable to probe below $\sim 10^{9.5} M_{\odot}$, the mass regime populated by dwarf galaxies.

Evidently the stellar mass functions of galaxies evolve with cosmic time and are dependent upon the mass scale considered. What about other galaxy evolution trends? The specific star formation rate (sSFR) tells us about the current star formation rate of a galaxy with respect to the stellar mass it has already formed. Figure 1 of Khochfar & Silk (2011) shows that the sSFR of star forming galaxies decreases with increasing stellar mass, with the slope of the decrease becoming progressively more shallow with redshift[3]. There is also a subtle flattening of the slope toward the high stellar mass end. Similarly, the global star formation rate density (SFRD) has been shown to evolve with redshift. Hopkins & Beacom (2006) show in their Figure 1 that the normalization of the global SFRD increases from the present day out to a redshift of $z \sim 2$, at which point it turns over and decreases. González et al. (2010) also shows in their Figure 5 that the sSFR at a constant stellar mass of $5 \times 10^9 M_{\odot}$ increases with increasing redshift out to $z \sim 2$, after which it remains constant (Damen et al. (2009) have observed a similar trend).

So far it is clear that galaxy formation is dependent upon the epoch of formation and the galaxy stellar masses involved. Given the model of structure formation outlined earlier, the formation of galaxies must also be influenced by the environment in which they are forming. Peng et al. (2010) showed that the density of the environment within which passive galaxies were evolving influenced their GSMF, while the star forming GSMF remained unchanged. They then followed this up with another study (Peng et al., 2011) which further clarified this observation. What they discovered was that of the passively evolving galaxies, the field galaxies residing in a low density environment had a different GSMF when compared with the passive central galaxies residing in high density enviroments. A similar observation

[3]This is a weak observation given the incompleteness of the higher redshift samples shown in their figure.

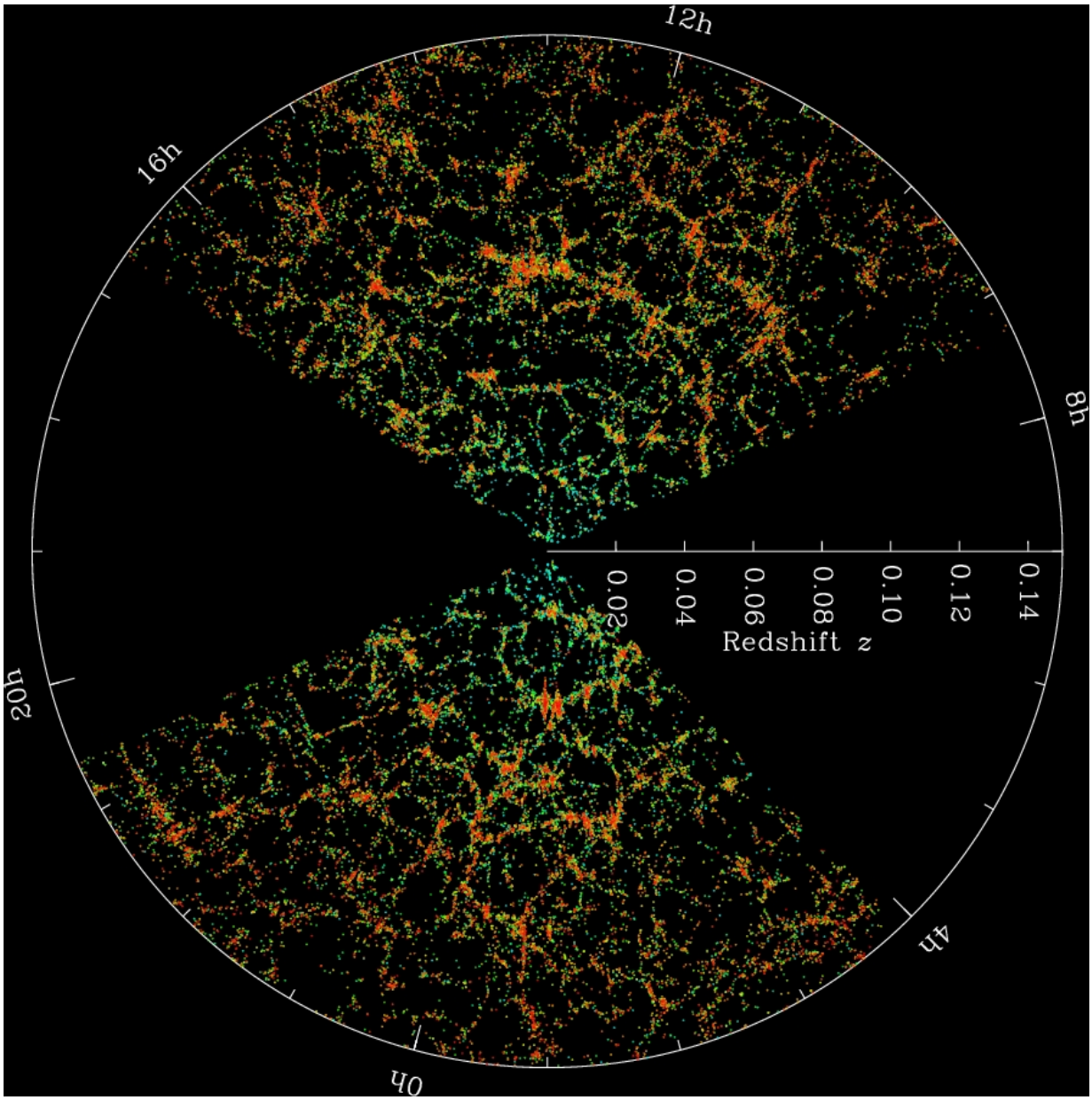

Figure 1.1: The presence of galaxy structure in the local universe as imaged by SDSS. (Image Credit: M. Blanton and the Sloan Digital Sky Survey)

was made by Bolzonella et al. (2010) who found that the GSMF of galaxies evolving in high density environments was lower in normalization in the low stellar mass regime than for galaxies which were evolving in low density environments, out to $z \sim 1$. However, their mass completeness limits did not allow them to probe below $10^{10} M_{\odot}$. The work of Drory et al. (2009) suggested a similar picture as that of Peng et al. except they found that the star forming galaxy population consisted of two components: bright and faint galaxies, which could be interpreted as central and satellite galaxies respectively.

All of these studies suggest further exploration is needed in the low stellar mass domain, as well as segregation by active and passive galaxy samples, in order to fully understand the impact of environment, stellar mass, and epoch of formation on the evolution of galaxies. It should also be obvious at this stage that the evolution of a galaxy is traced through the observed activity of its stellar content. Thus to address the issues mentioned above we require a mechanism to measure and trace the formation of a galaxy's stellar content through its history.

1.1 Star Formation Tracers

There are many different types of tracer for galaxy star formation used in modern astronomy such as those which are calibrated based upon the flux measured from the ultraviolet continuum, radio continuum, infrared, $Lyman - \alpha$ absorption, and the H_{α}, and $[\mathrm{OII}]_{\lambda 3727\text{Å}}$ emission lines. Each has advantages and disadvantages which must be understood when interpreting results based upon them. More importantly in cases such as when using H_{α} or $[\mathrm{OII}]_{\lambda 3727\text{Å}}$, they have an epoch dependent window of applicability. Here we only discuss in detail the latter two tracers of star formation since they are used in the study described in this work.

The most commonly used star formation indicator is the H_{α} emission line. Hot young OB type stars are immersed within gas clouds consisting predominantly of hydrogen with smaller percentages of helium and heavier elements, an environment typically referred to as a stellar nursery. The ultraviolet (UV) radiation emanating from these stars is energetic enough ($\lambda < 912\text{Å}$) to be absorbed by the surrounding hydrogen gas and cause hydrogen atoms to be ionized ($E_{\gamma} \geq 13.6eV$). The liberated electrons can remain free for a timescale which is dependent upon the electron and proton density of the cloud, but which is on the order of hundreds of years. This is much less than the lifetime of the OB stars generating the ionizing radiation implying that the electrons will recombine with the surrounding protons, then be re-ionized and recombine again, eventually reaching an equilibrium state representing a ratio of the number of atoms undergoing photoionization to the number of

those recombining at any given time. During recombination of hydrogen an electron is captured by a proton, with the electron subsequently cascading down the energy levels of the hydrogen atom, releasing characteristic photons along the way. It is the transition from the n=3 to 2 energy state which produces the H_α line at 6563Å. Many stellar nurseries are dominated by H_α emission which is a direct result of hydrogen being ionized, hence these environments are referred to as H_{II} regions.

Since an equilibrium state has been reached in the H_{II} region, the number of ionizing photons necessary to produce the equilbrium state can be determined, which then correlates directly with the total UV luminosity of the OB stars. This assumes that the H_{II} region absorbs *all* of the ionizing photons, a situation referred to as an ionization bounded H_{II} region. Studies have measured these quantities on galaxy scales (for example Robert Kennicutt, Jr. has been a *tour de force* in this area of astronomy; Kennicutt (1983a,b, 1992)) and calibrations have been determined for the conversion from UV luminosity to star formation rate, which is dependent upon the assumed initial mass function for the stellar content of the galaxy.

Thus H_α is an ideal proxy or tracer for star formation in star forming galaxies. However the drawback of using H_α is that at redshifts of $z \geq 0.4$, it is no longer observable in the optical window. For higher redshifts it must be observed in the near-infrared which remains technically challenging. For this reason other star formation proxies are needed which emit at shorter rest frame wavelengths[4]. The $[\mathrm{OII}]_{\lambda 3727\text{Å}}$ emission line is one such proxy for star formation in the mid-to-high redshift universe.

What is commonly referred to as the $[\mathrm{OII}]_{\lambda 3727\text{Å}}$ emission line is actually a *doublet* - two lines spectrally close together at 3736Å and 3729Å. The 'single' $[\mathrm{OII}]_{\lambda 3727\text{Å}}$ line terminology refers to observational conditions where the doublet can not be spectrally resolved. In surveys which attempt to discern global galaxy properties such as luminosity or star formation rate, a high level of resolution capable of resolving the [OII] doublet is unnecessary since it is the total $[\mathrm{OII}]_{\lambda 3727\text{Å}}$ line flux that is used to determine these quantities.

The process which leads to $[\mathrm{OII}]_{\lambda 3727\text{Å}}$ photon emission in star forming regions is significantly different from the emission process of the commonly used star formation tracer of H_α. It is not just H_{II} that exists in the ionized plasma in the surrounding regions of newly formed OB stars. Oxygen is present because of stellar enrichment, and is also ionized (i.e. [OII]) because of the UV radiation released by the hot young OB stars. The plasma contains energetic electrons which will *collisionally excite* the [OII] ($E_{col} \sim 3.3eV$) provided critical temperatures of $T > 10^4 K$ and electron densities of $n_e \sim 10^4 cm^{-3}$ have

[4]See Kewley, Geller & Jansen (2004) for an excellent review of the $H_\alpha$and [OII] star formation tracers.

been reached. The critical temperature corresponds to the kinetic energy imparted by a scattering electron into the [OII] atom, and the critical electron density is defined as the density at which the rate of spontaneous emission for an [OII] atom balances the rate of its collisional excitation (an equilibrium state). The [OII] doublet emission lines are a result of *forbidden* atomic transitions, meaning that an excited ionized oxygen atom cannot de-excite to a lower energy level according to the selection rules of quantum mechanics, and must therefore spontaneously decay or lose its energy through collisions with the surrounding plasma. The former has a very low likelihood of occuring suggesting that in a high density environment, collisional de-excitation is the most probable method for the excited ionized oxygen to lose energy. However the electron density in H_{II} regions is small enough that collisional de-excitation becomes equally or more improbable. Thus the only means for excited [OII] to de-excite is via spontaneous emission, producing photons with the wavelengths of the doublet.

Fortunately the critical electron density and excitation temperature necessary for [OII] to excite and undergo spontaneous emission are commonly met in H_{II} regions. Thus the $[\mathrm{OII}]_{\lambda 3727\text{Å}}$ line flux is indirectly correlated with the UV luminosity of the OB stars. Several studies have calibrated the $[\mathrm{OII}]_{\lambda 3727\text{Å}}$ luminosity to star formation rate (Gallagher, Bushouse & Hunter, 1989; Kennicutt, 1998; RosaGonźalez, Terlevich & Terlevich, 2002), each of which have taken care to account for the effects of reddening due to dust, metallicity, and ionization fraction. Star formation - $[\mathrm{OII}]_{\lambda 3727\text{Å}}$ calibrations are constantly improving, allowing $[\mathrm{OII}]_{\lambda 3727\text{Å}}$ to be an excellent tracer of star formation for redshifts of $z \gtrsim 0.4$.

1.2 Galaxy Formation at $z \sim 0.75$

With the goal of probing down to the dwarf galaxy stellar mass range at mid-to-high redshift to further clarify the picture of galaxy formation at low stellar masses, the Redshift One LDSS-3 Emission Line Survey (hereafter ROLES) was designed to target K-faint star forming galaxies near $z \sim 1$ (Davies et al., 2009). A spectroscopic survey was conducted using the LDSS-3 instrument on the Magellan (Clay) telescope in Chile, obtaining redshifts and [OII] emission line fluxes for galaxies in the mass range of $8.5 < Log\,(M_*/M_\odot) < 9.5$. The survey was divided into two studies: the first targeted a redshift of $z \sim 1$ using the custom made *KG750* filter, and the second explored a redshift of $z \sim 0.75$ using the lower spectral window of the custom made *KG650* filter. The former was analysed previously and results were published in (Gilbank et al., 2010a,b, 2011; Li et al., 2011). The latter is the focus of this work which followed the methodology of Gilbank et al. (2010b).

Here, we add to the luminosity function and star formation rate density results of the

first ROLES method paper (Gilbank et al., 2010b), and the galaxy stellar mass function and specific star formation results in Gilbank et al. (2011), by analysing [OII] luminosities of star forming galaxies in the redshift range of $0.62 < z < 0.885$. We also examine the effect of environment on our mass-complete sample of star-forming galaxies at $z \sim 0.75$ by dividing our sample into high density structure and low density field populations for each of the four main science results. We then compare our sSFR as a function of density with the result published in Li et al. (2011).

This thesis is presented as follows: Chapter 2 describes the survey and image reduction methodology; Chapter 3 details the automated emission line finding algorithm; Chapter 4 outlines the determination of critical values (i.e. SFR, completeness, V_{max}, etc.) needed for the main results; Chapter 5 presents luminosity and mass functions, as well as SFRD and sSFR as functions of mass; Chapter 6 introduces plans for a future follow-up survey; and Chapter 7 closes with concluding remarks. AB magnitudes are used throughout unless otherwise stated and we use a ΛCDM cosmology of $H_0 = 70\ km\ s^{-1}\ Mpc^{-1}$, $\Omega_M = 0.3$, and $\Omega_\Lambda = 0.7$. Finally, all ROLES SFRs have been corrected using the empirical stellar mass dependent relationship determined in Gilbank et al. (2010a)[5].

[5]This empirical correction is discussed in further detail in Chapter 4.

Chapter 2

Observations: Image Acquision, Reduction, and Calibration

The design and implementation of the ROLES KG650 ($z \sim 0.75$) survey (hereafter referred to as ROLES75) was identical to the previous higher redshift ROLES KG750 ($z \sim 1$) survey (Gilbank et al., 2010b, hereafter referred to as ROLES1). In this section we review the target selection criteria, observation strategy, and image reduction steps.

2.1 Target Selection

Targets were selected based upon their K-band magnitudes (as a proxy for stellar mass) and their photometric redshifts (provided by Förster Schreiber et al. (2006, FIRES) and Mobasher & Dahlen (2009, CDFS)). Photometric redshifts were used as a target weight or priority during the initial survey mask design. A Monte Carlo method was used to create many potential versions of the survey masks, optimizing the total target weight of each simulated mask given the geometrical constraints of the circular masks and that all high priority targets had to be placed. Using this strategy, ROLES75 used six masks per pointing (one pointing for FIRES, two pointings for CDFS) for a total of 18 masks. Targets were pre-selected from fields with photometric redshifts (those most probable of lying in the range of $0.62 < z < 0.885$) and deep K-band imaging (limited to $22.5 < K < 24$) corresponding to low stellar masses. These targets were then observed using multi-object spectroscopy (MOS) allowing spectroscopic redshifts and $[\mathrm{OII}]_{\lambda 3727\mathrm{\AA}}$ emission line derived star formation rates (SFRs) to be obtained.

ROLES75 consists of two pointings in the Great Observatories Origins Deep Survey (GOODS) region of the Chandra Deep Field South (CDFS, e.g. Wuyts et al., 2008) and one pointing in the MS1054-03 cluster region of the Faint Infra-Red Extragalactic Survey (FIRES, e.g. Förster Schreiber et al., 2006; Crawford et al., 2011). FIRES actually consists of two pointings: the MS1054-03 cluster at $z = 0.83$ and the Hubble Deep Field South (HDF-S), however we have only targeted the cluster since it is wider in area than HDF-S thus providing more targets to observe, and it allowed us to explore the effect of environment (cluster vs. field) on galaxy downsizing and evolution. Throughout, FIRES will refer only to the MS1054-03 cluster pointing. Extensive multi-color photometry and photometric redshift catalogs exist for all three fields. The three ROLES75 pointings are shown in Figures 2.1 and 2.2 with observational targets overplotted.

2.2 Observations

All spectroscopic observations were obtained using the 6.5 meter Clay telescope, which is one of a pair called the Magellan telescopes, owned and operated by the Carnegie Institution. Multi-object spectroscopy for our 1946 targets was provided by the Low Dispersion Survey Spectrograph 3 (LDSS-3). The LDSS-3 instrument is ideally suited for multiobject spectroscopy with its large CCD and FOV, low read-noise and low dark current (see Table 2.1 for specific values.)[1]. The spectra were produced by the *medium red* grism (300 $lines/mm$) which has a low dispersion of approximately 2.65Å/pixel at 6500Å and a relatively stable (however not flat) throughput across the KG650 wavelength range. Figure 2.3 shows the efficiency of the VPH Medium Red grism at the center of the FOV. Combined with the plate scale of $0.189''$/pixel and survey mask slit width of 0.8", the resolution is 11.2Å FWHM.

The spectral wavelength range was limited to approximately 650 ± 50nm by a filter, herein referred to as KG650. The transmission curve for the KG650 filter is shown in Figure 2.4. Given the spectral wavelength range of 6040Å $\leq \lambda_{obs} <$ 7025Å for this red filter[2] and the explicit targeting of the $[\mathrm{OII}]_{\lambda 3727\text{Å}}$ emission line, the redshift range covered by this survey is $0.62 < z_{ROLES} < 0.885$.

The design of the survey masks was driven by the Nod & Shuffle (N&S) (Glazebrook & Bland-Hawthorn, 2001; Gilbank et al., 2010b) observing strategy. Target slits were 0.8"

[1] See http://www.lco.cl/telescopes-information/magellan/instruments/ldss-3/ldss-3-ccd-system/ccd-system

[2] See http://www.lco.cl/telescopes-information/magellan/instruments/ldss-3/ldss-3-users-guide/users-guide

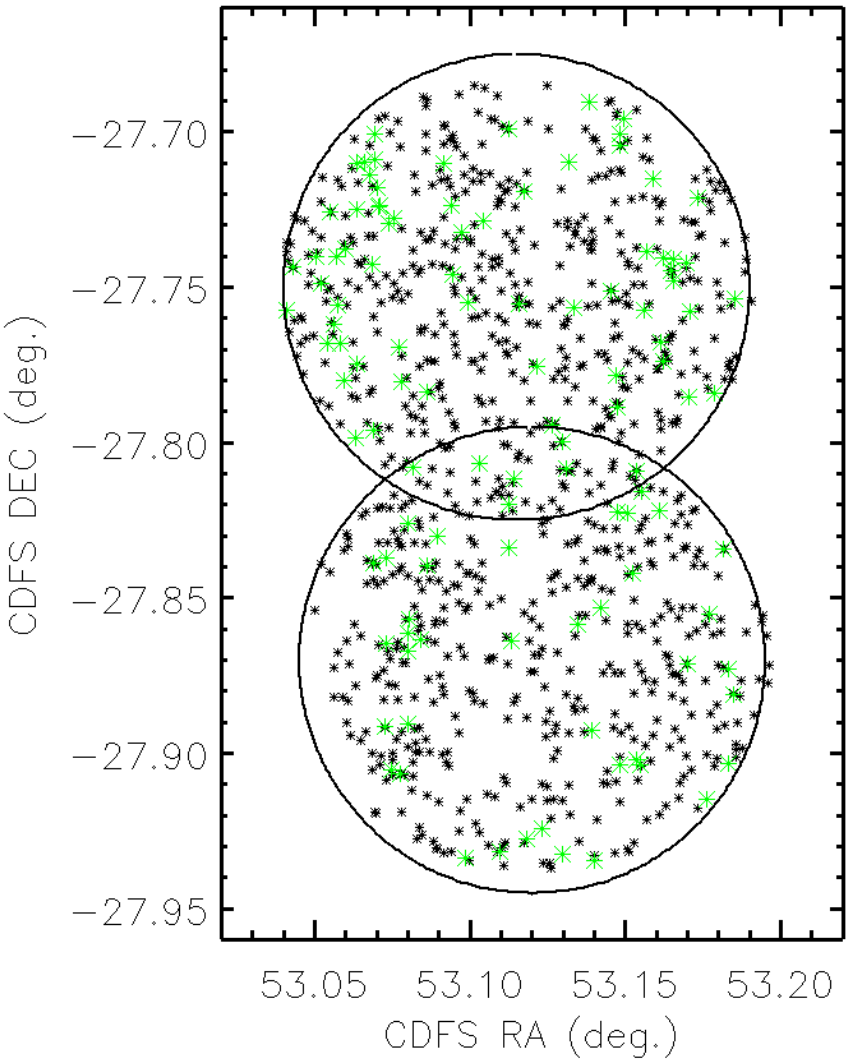

Figure 2.1: ROLES KG650 pointings in CDFS, centered at $(RA, Dec) = (03^h32^m27.6^s, -27^d45^m00^s)$ and $(03^h32^m28.8^s, -27^d52^m12^s)$. Each pointing is limited by the $\sim$ 8.2 arcminute diameter field of view (FOV) of the LDSS-3 spectrograph, shown as the thick black circle. All of the galaxies targeted are shown as black asterisks while those galaxies with observed emission lines (not necessarily [OII]) are overlaid with green asterisks.

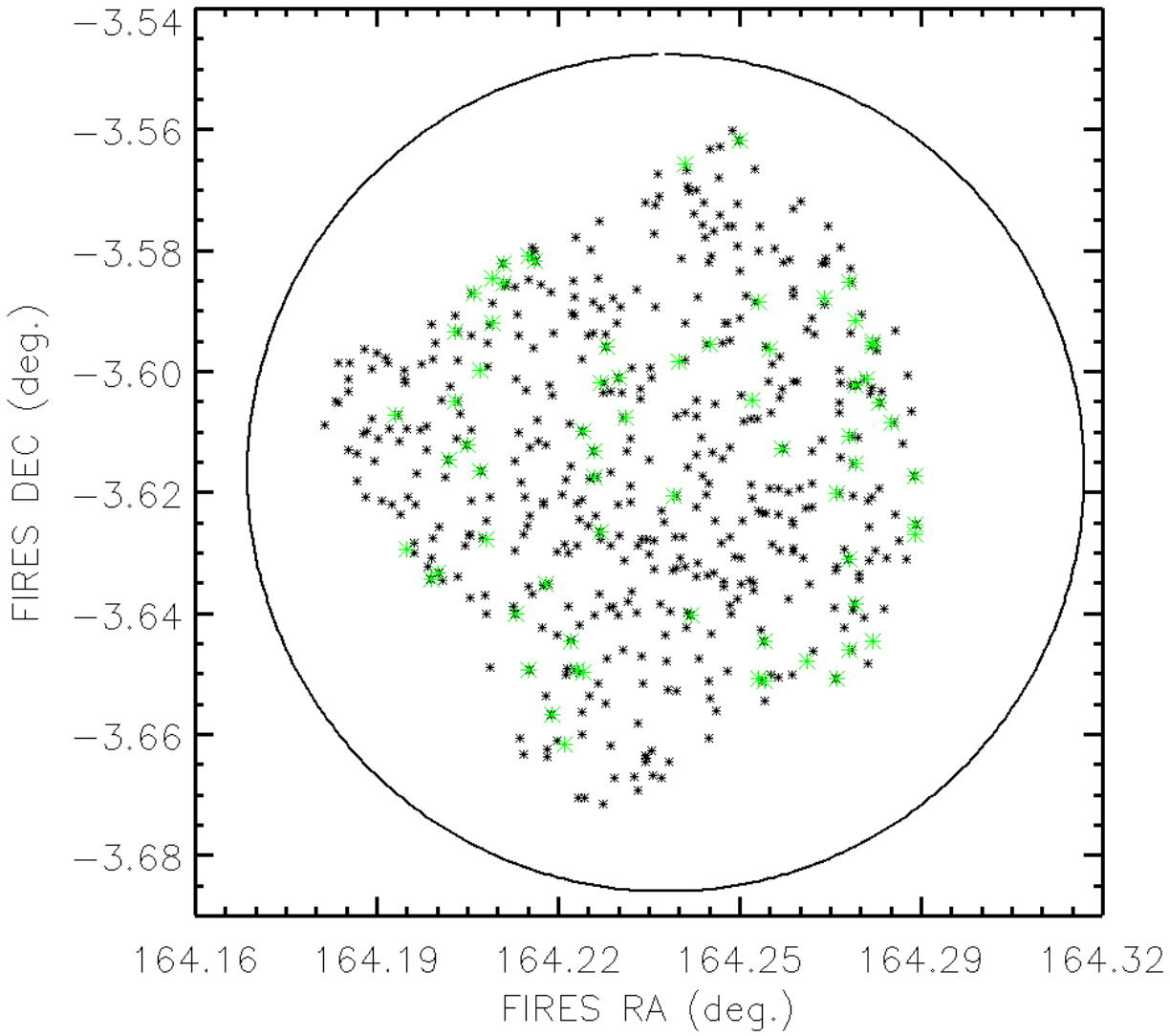

Figure 2.2: ROLES KG650 pointing in FIRES, centered at $(10^h56^m58.26^s, -03^d37^m0.53^s)$. The FIRES area is a 5.5 x 5.3 arcminute region which falls completely within the LDSS-3 FOV of $\sim$ 8.2 arcminutes diameter, shown as the thick black circle. All of the galaxies targeted are shown as black asterisks while those galaxies with observed emission lines (not necessarily [OII]) are overlaid with green asterisks.

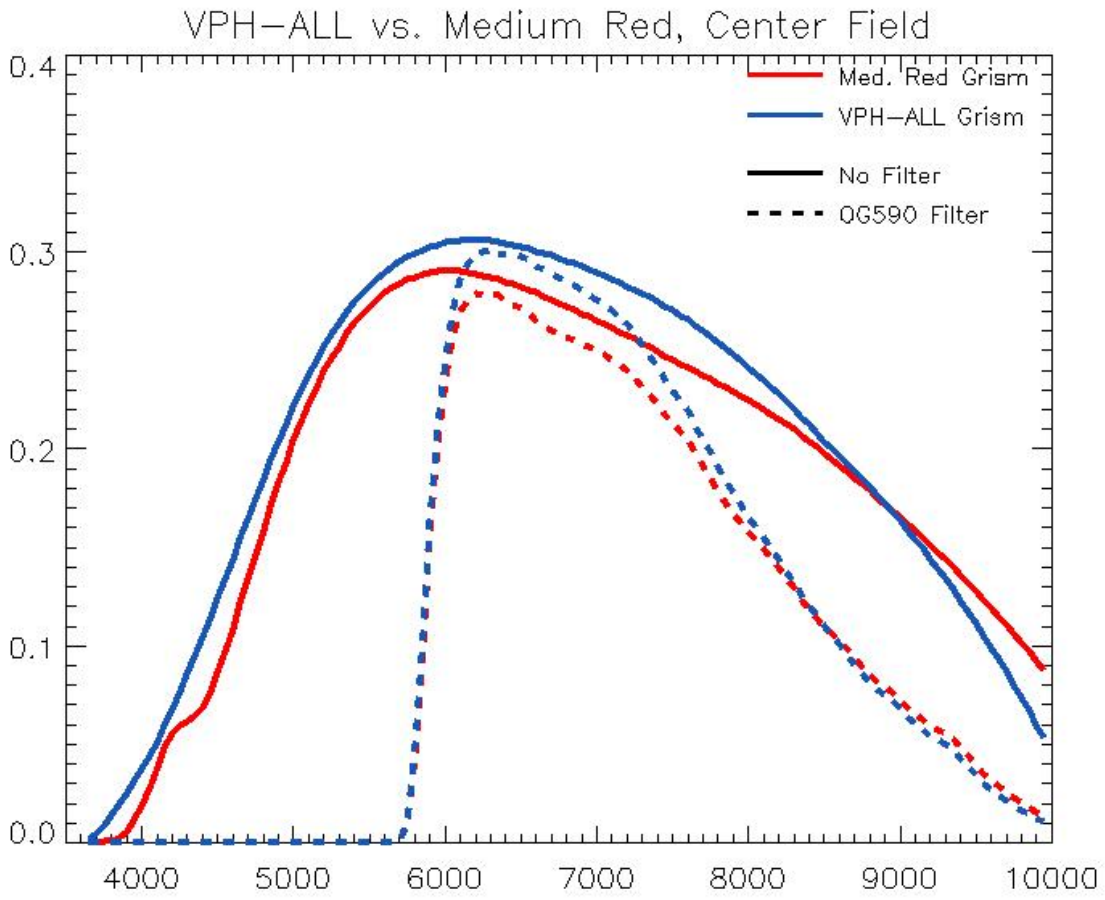

Figure 2.3: The transmission curves for the VPH Medium Red (solid red) and VPH All (solid blue) grisms. For comparison purposes, the same throughput curves are shown with the OG590 filter added to the optical path (dashed curves). The VPH Medium Red efficiency is highly linear in the spectral range of $6000 - 7000$Å. Image courtesy of Las Campanas Observatory Carnegie Institution of Washington.

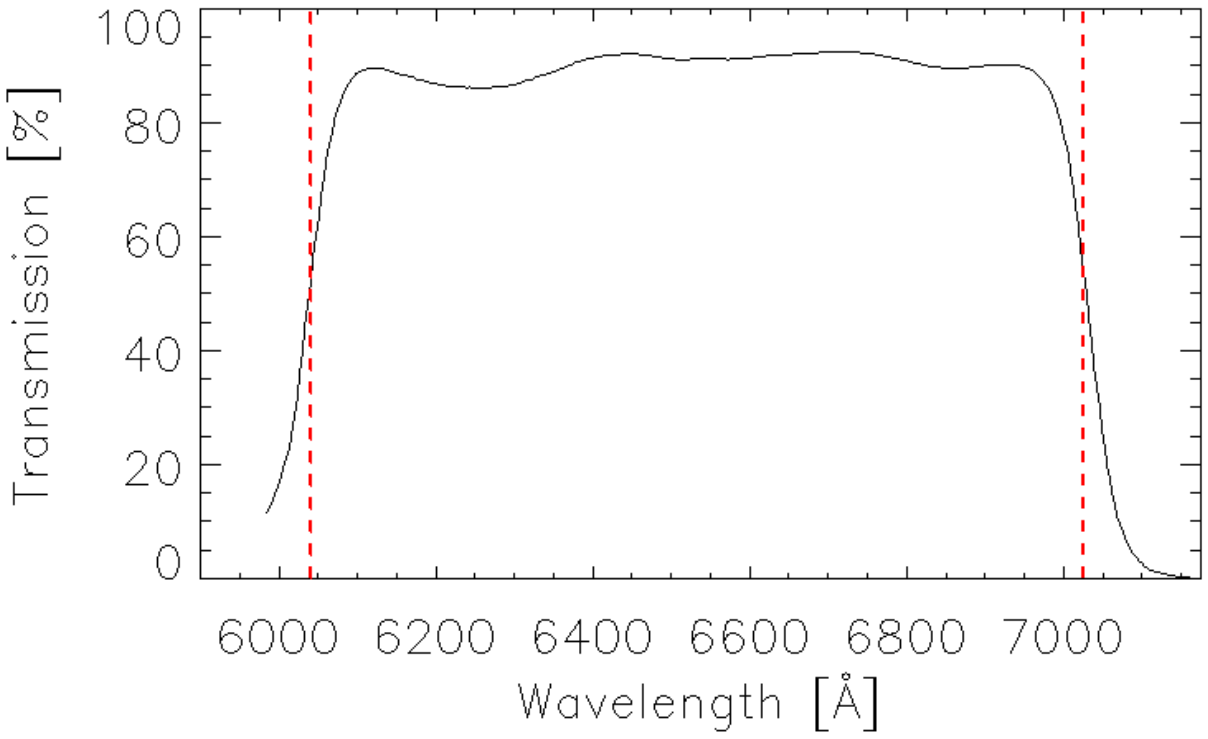

Figure 2.4: The transmission curve for the custom designed KG650 filter. The vertical dashed lines at $\lambda = 6040, 7025$Å indicate the spectral range considered by the ROLES KG650 survey, and correspond to the full width at half maximum (FWHM) locations of the transmission curve. Since the ROLES KG650 survey specifically targeted $[\mathrm{OII}]_{\lambda 3727\text{Å}}$, then the survey redshift range is also restricted by the filter FWHM and is taken to be $0.62 < z_{ROLES} < 0.885$.

Table 2.1: Values for important parameters of the LDSS-3 instrument.

Parameter	Value
Gain	$0.7e^-$/DN
Read Noise	$3.5e^-$
Dark Current	$1.1e^-$/hr when cooled $< -110°$C
Array Configuration	1 row x 2 columns
Array Size	4064 x 4064 pixels
Pixel Size	$15\mu m$
FOV	$8.2'$
Plate Scale	$0.189''$/pixel

wide by 3.0" long, which allowed for nearly 200 objects to be targeted per mask given the LDSS-3 FOV of 8.2' diameter, and the requirement that dispersed object spectra must not overlap. The N&S technique is as follows:

1. The target object is observed at a location (position A) near one end of a slit for a pre-set amount of time (60 seconds for ROLES);
2. After this observing time has elapsed, the telescope is "nodded" such that the target is now positioned at the opposite end of the slit (position B, 1.2" "nod" distance for ROLES);
3. The charge collected on the CCD is "shuffled" a full slit length (3" or 16 pixels for ROLES LDSS-3);
4. The target is again observed for the pre-set amount of time;
5. Once this time has elapsed the telescope is "nodded" back to its original position and the charge accumulated on the CCD is "shuffled" back to its original location;
6. Repeat until the cumulative amount of observing time reaches the exposure time desired for the target object.

The principle advantage of the N&S technique is that it allows for accurate sky subtraction when observing objects dominated by sky counts. Figure 2.5 shows a typical ROLES75 night sky spectrum (1800 second exposure time) with prominent skylines annotated, which must be subtracted from object spectra.

The details of sky subtraction will be covered in a later section but for illustrative purposes, Figure 2.9 provides a pictorial explanation of the technique.

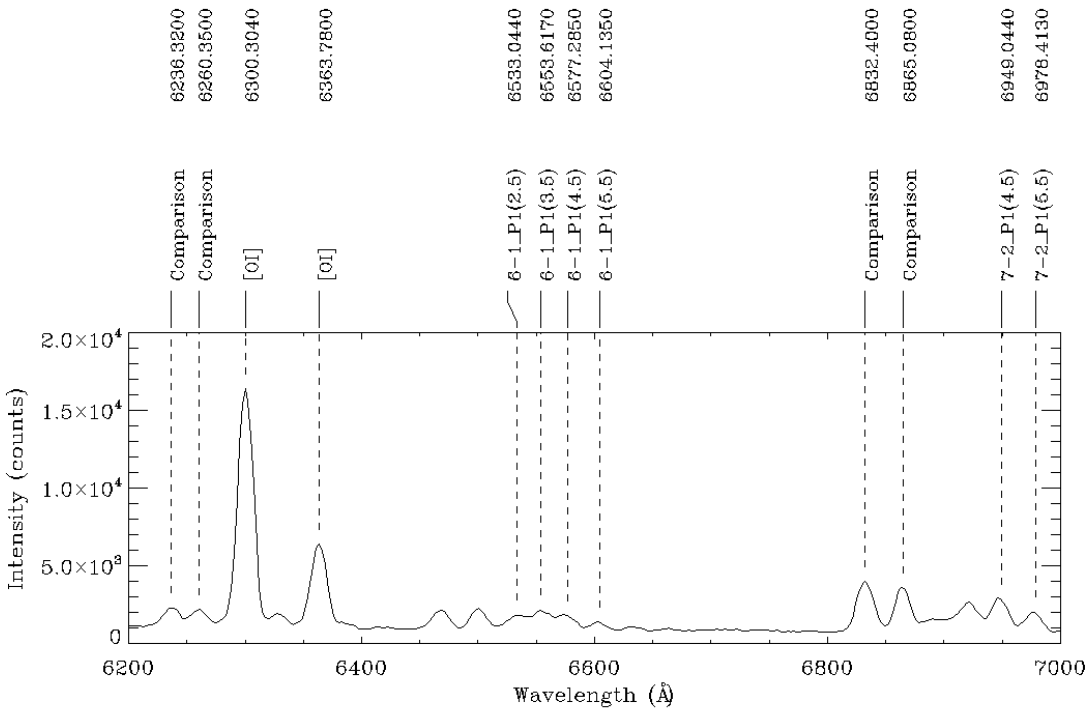

Figure 2.5: A typical night sky spectrum observed through a slit in a ROLES survey mask with an exposure time of 1800 seconds. It is clear that there are many dominating skylines within the ROLES KG650 spectral range such as [OI] and the *comparison* (blended) lines. These features must be removed from targeted galaxy spectra before further analysis.

2.2.1 ROLES Survey Masks

As mentioned in the introduction the ROLES KG650 survey targeted low mass galaxies at a redshift $z \sim 0.75$ in both the CDFS and FIRES fields, selected by their apparent K-band magnitudes ($22.5 < K_{AB} < 24$) and modelled photometric redshifts. Since the survey was only concerned with these targets, masks corresponding to the LDSS-3 FOV were created with slits cut where the target objects were located on the sky. The slits allowed light through from the target objects (and guide stars) and blocked everything else in the FOV.

Mask design is one of optimization, driven by the desire to place the largest number of high priority target objects on the mask while avoiding overlap. A typical mask, imaged through the optical path used in this survey, is shown in Figure 2.6 (Note that it is not dispersed). In the figure a large red circle denotes the LDSS-3 FOV of $\sim 8'$ and the black border around the figure corresponds to the approximate area captured by the LDSS-3 CCD. Contained within the circle are six large dark marks which correspond to locations in the mask where slits have been cut for guide stars used to align the mask to the sky. This is very important since the mask may shift and warp by small amounts while in the optical path due to the movement of the telescope itself, and thus the mask must be re-aligned to the guide stars frequently. The slits cut for these guide stars are large since the stars are much closer to us and appear much brighter in the sky, so the slit is cut larger to capture this light. Ideally the centers of the guide star slits would overlap with the centers of the imaged guide stars themselves. However, this is not always the case due to mask flexion or distortions along the optical path. Since the guide star alignment error (at the time of observing) was always one pixel or less, these distortions were not large enough to require anything more than the corrections applied by software during the image reduction pipeline.

In the example mask there are 173 smaller slits within the LDSS-3 FOV, denoted by the circle, corresponding to the galaxies targeted by this mask. Each slit is 0.8" wide and 3" high (or $\sim 4 \times 16$ pixels using the plate scale of 0.189"/pixel), and each has been placed such that there is no overlap with a *dispersed* spectrum from a neighbouring slit. For most targeted galaxies the slits are cut large enough to allow all of the light from the galaxy through (as observed through the KG650 filter).

As can also be seen in Figure 2.6 there are small marks found outside of the circle denoting the LDSS-3 FOV. These are typically 'hot' pixels which have recorded the passage of cosmic rays or are bad pixels within the LDSS-3 CCD.

The ROLES KG650 survey imaged 576 unique targets in the FIRES field (one pointing centered on the MS1054-03 cluster) and 1370 targets in the two Chandra Deep Field South

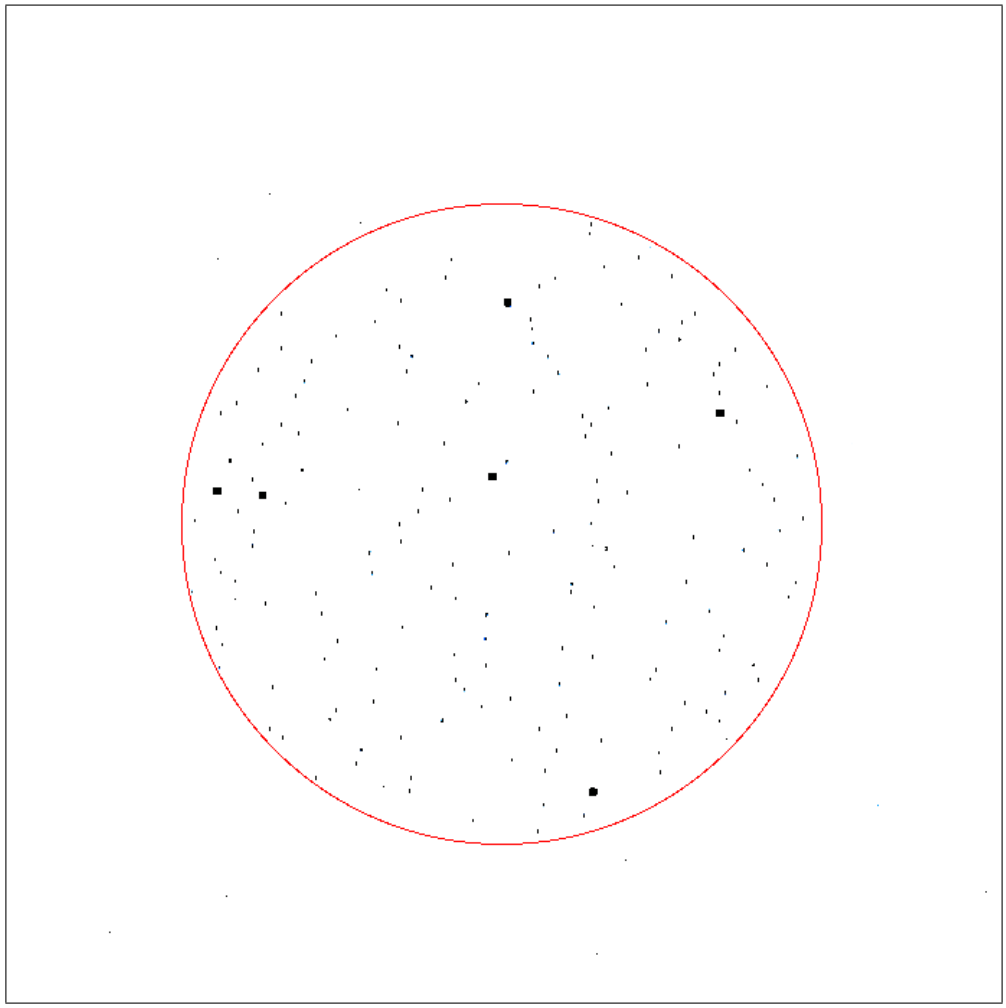

Figure 2.6: An example of a survey mask imaged with the LDSS-3 instrument. The medium red grism was not used for this quick acquisition and thus the image has not been spectrally dispersed. The red circle outlines the LDSS-3 FOV. Black marks outside of the circle are either 'hot' pixels produced by the passage of cosmic rays or bad pixels in the CCD. The six large black marks within the circle correspond to slits cut for the guide stars used to align the mask to the sky as observed by the telescope. The numerous smaller black marks within the circle correspond to slits cut for the target galaxies.

pointings, for a total of 1946 unique galaxies. These targets were distributed across 18 masks, with six masks per pointing. There were cases where slits were cut too close to mask edges, or to each other, and thus yielded unusable spectra. The number of bad slits per mask typically ranged between 2 and 7, with CDFS masks 40 and 41 containing an unusually large number of bad slits, with 13 and 14 respectively. The total exposure time per mask was identical for FIRES and CDFS except for CDFS masks 40 and 41 where we acquired an extra 30 minute exposure for each due to time remaining in the observing programme. Table 2.2 lists the masks with their target counts (including duplicate target galaxies), total exposure time, and typical seeing conditions at the time of observation. For each field pointing an effort was made to place the highest priority targets on a limited number of masks. Any remaining space on a given mask was then filled with lower priority targets. Similarly if there were still lower priority targets not already positioned on a mask, they were then added to a new mask. With all potential targets placed on masks, the observing strategy was then to image the highest priority masks first, and image lower priority masks with whatever allocated survey time was remaining.

2.3 Image Reduction

The FITS image files created by LDSS-3 were processed through an image reduction pipeline similar to that described in the Carnegie Observatories COSMOS (Carnegie Observatories System for MultiObject Spectroscopy) Cookbook[3] specifically applied to LDSS-3 spectra. Since the objects targeted by the ROLES75 survey were faint, many supplemental IDL routines were custom written to process the images, taking special care to ensure accurate noise propagation and wavelength calibration. In some cases, these routines were preferred over some of the tools recommended in the COSMOS Cookbook. Following is a description of the steps taken to create the reduced images which later provided emission lines used to determine the global star formation at $z \sim 0.75$.

2.3.1 Initial Frame Combining

LDSS-3 was set up in a 1x2 CCD array format meaning that each mask exposure consisted of two raw FITS images. These images were combined using the COSMOS "stitch" routine with gain parameters set according to each specific amplifier and dewar parameter set to

[3]See http://obs.carnegiescience.edu/Code/cosmos/Cookbook.html

Table 2.2: The two pointings in CDFS are labelled as CDFS.1 and CDFS.2. The total number of unique ROLES75 targets is 1946. For the FIRES pointing, numbers listed in round brackets represent the total number of targets in the mask including "filler" targets which were part of another survey. The number in square brackets indicates the total number of targets applicable to this survey. Finally, the non-bracketed target counts highlight the number of objects with usable spectra, including duplicates.

Mask ID ID	Field	Number of Targets	Exp. Time (hrs)	Ave. Seeing (")
mask24	FIRES	115 [117] (197)	2	0.5
mask25	FIRES	112 [114] (188)	2	0.6
mask26	FIRES	100 [102] (188)	2	0.63
mask27	FIRES	95 [98] (194)	2	0.53
mask28	FIRES	99 [102] (194)	2	0.6
mask29	FIRES	105 [107] (201)	2	0.72
mask30	CDFS.1	191 [195]	2	1.0
mask31	CDFS.1	180 [186]	2	0.79
mask32	CDFS.1	178 [182]	2	0.8
mask33	CDFS.1	175 [182]	2	1.0
mask34	CDFS.1	178 [186]	2	1.0
mask35	CDFS.1	171 [178]	2	0.66
mask36	CDFS.2	167 [173]	2	0.86
mask37	CDFS.2	167 [173]	2	0.92
mask38	CDFS.2	164 [171]	2	0.88
mask39	CDFS.2	160 [167]	2	1.19
mask40	CDFS.2	156 [169]	2.5	0.82
mask41	CDFS.2	154 [168]	2.5	0.74

LDSS3-2[4]. The "stitch" routine removes bias and corrects for differences between amplifier gains in LDSS-3 so no further bias removal was necessary after this stage.

2.3.2 Bad Pixel Mask from Charge Traps & Cosmic Rays

A bad pixel mask (BPM) was created using "Nod & Shuffle dark frames" (N&S darks) acquired throughout the observing phase of the survey. An N&S dark is a frame acquired with the dome closed and any lights turned off, and uses the same observing strategy (N&S) as that used to acquire the science frames. The resulting image is one which is mostly dark (predominantly read noise counts) with "streaks" of bright pixels indicating "bad pixels" created by charge being trapped by individual pixels in the CCD array. The "streaks" correspond to the charge shuffle distance and direction defined by the N&S strategy. A BPM was made from a N&S dark by dividing the original N&S dark frame by a 1x3 boxcar smoothed version (smoothing done in the direction perpendicular to the shuffle direction) of the same frame. "Bad pixels" appeared brighter in the ratio of the frames and were recorded as being bad in the BPM. Since several N&S darks had been acquired, they were each processed in the same manner and finally median combined into one single BPM. The median combined BPM was later processed through the same steps used to create the stacked science and noise frames (See §2.4).

As many masks were imaged with only three exposures, we used the IRAF "cosmicrays" task to identify the locations of cosmic rays (CR) in each frame based upon user-defined threshold levels and cosmic ray shapes. The pixel locations were recorded as a unique BPM for each exposure, which was propagated through the same image shifts and additions used to create the stacked science and noise frames. This method avoided the issue of excess flux removal by the cosmic ray rejection algorithm built in to the IRAF "imcombine" task, which arose when stacking fewer than four frames. During the median combination step of the image stacking procedure, the N&S and exposure-dependent CR BPMs were applied.

2.3.3 Wavelength Calibration and Image Stacking Final Preparation

Before final images for each mask could be created, the individual science frames to be stacked had to be aligned to a common reference frame (the first frame in the list of mask

[4]For a list of LDSS-3 amplifier gain and read noise see http://www.lco.cl/telescopes-information/magellan/instruments/ldss-3/ldss-3-specs/ldss-3-specs

exposures to be stacked). For most masks the individual exposures to be stacked were acquired on different dates. As masks were interchanged in the optical path frequently and the telescope was at different orientations while tracking the target field at different times of the year, differences in mask (and thus image) flexure, rotation, and shifts were introduced between one exposure and another. The image stacking procedure had to correct for these effects so that the spectra in the reference frame would lie on the same pixels as the corresponding spectra in the other frames to be stacked. Since all spectra within a mask must be wavelength calibrated individually using the pixel location and known wavelength of their bright sky lines, this information was also used to determine each X_{CCD} and Y_{CCD} scaling, shift, and rotation, with respect to the reference image.

In addition to using an arc frame containing spectra with known emission lines generated by a standard helium-neon-argon lamp, the wavelength calibration procedure also used known sky lines. To make the sky lines more prominent for the wavelength calibration algorithm, each science frame was shifted by 16 pixels (the charge shuffle distance) and added to the non-shifted version, resulting in spectra containing the faint target object embedded in dominant sky counts (see the bottom left section of Figure 2.9). The sky lines were clearly visible in these frames and allowed for highly accurate emission line centroiding by COSMOS routines.

The COSMOS "aperture" routine was used to make predictions of initial positions of the slit centers in each mask. These positions were compared to the actual slit center positions as imaged through the optical path and corrected (to less than 1 pixel difference) using the "align-mask" routine. The positions of known arc lines were predicted for the arc calibration frames using the "align-mask", "map-spectra", and "spectral-map" routines. A linear wavelength calibration solution (converting pixels to wavelength) was determined using the "adjust-map" routine which was accurate at centroiding arc emission lines in the spectral direction but inaccurate at centroiding in the spatial direction (along the length of the slit). The inaccuracy of centroiding emission lines in the spatial direction was corrected using a custom-written IDL routine, discussed later. The wavelength calibration solution determined from the arc frame was applied to each science frame in a mask set again using "align-mask", "map-spectra", and "spectral-map."

The COSMOS "adjust-map" routine was adequate for providing an *initial* wavelength calibration solution for most slits in a given mask. However there remained several cases where emission lines in slits were not accurately calibrated according to the arc frame solution. For this reason an IDL routine was used to determine a third order wavelength calibration solution to all of the slits in each mask. The emission line positions predicted by COSMOS were used as an initial solution which was then adjusted by the third order solution (See Figure 2.7). Emission line position residuals were typically $\lesssim 0.7$Å indicating

a highly accurate wavelength calibration solution.

As mentioned earlier the COSMOS "adjust-map" routine is inaccurate at determining the emission line centroid position in the spatial direction. A custom-written IDL routine was used to adjust the line positions in the spatial direction by cross-correlating a $1 - D$ kernel, shaped like the slit (projected in the spatial direction), with each dispersed spectrum in the mask. The cross-correlation was performed at each predicted sky line location along the spatial direction and resulted in a typical shift of 8 pixels (See Figure 2.8).

The transformations between science frames and their common reference frame (the first in the list of frames to be stacked) were determined based upon the common sky emission line centroid positions in each frame. The transformations commonly required a small rotation, shifts in the X_{CCD} and Y_{CCD} directions, and on occassion a scaling. The IRAF task "geomap" computed these transformations while the "geotrans" task was used to apply them to each non-reference frame to be stacked.

The applied "geomap/geotrans" transformations accounted for differences in slit positions from one exposure frame to another, however there were also cases where the target galaxy within a slit varied slightly in position between the frames to be stacked. To rectify this, another IDL program determined and applied any further required shifts in the spectral and spatial directions based upon a list of bright emission lines identified by eye and found in each frame to be stacked. The bright emission lines were located in (and thus the image shifts determined from) the "nod-folded" (sky subtracted, object combined) frames which were non-stacked versions of the final science frame (see the top left and top right sections of Figure 2.9). When deemed necessary, further applied shifts were typically ~ 1 pixel in the X_{CCD} and/or Y_{CCD} directions.

2.4 Creation of Stacked Frames

The wavelength calibrated and frame-aligned exposures were combined or "stacked" such that the full exposure time of the mask was retained. The nature of the Nod & Shuffle concept allowed the frames to be stacked in a very methodical manner which is described below and shown in Figure 2.9. In both the final science and noise frames, a shift of 16 pixels (the shuffle distance), later followed by a shift of 6 pixels (the nod distance) was required, with only an addition or subtraction differentiating the two types of frames.

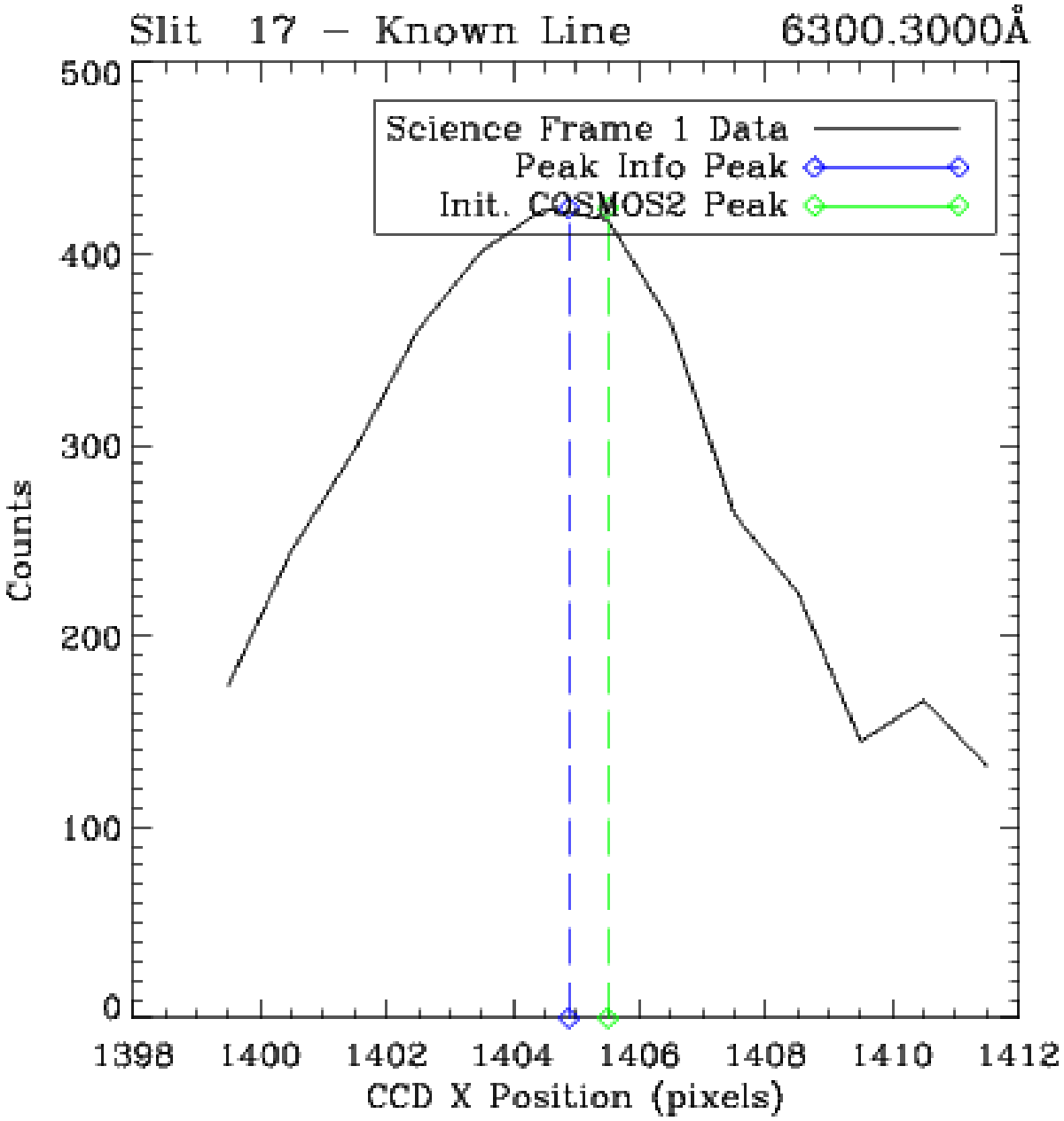

Figure 2.7: IDL custom-written routine vs. COSMOS "adjust-map" centroiding of the bright oxygen sky line at 6300Å. The IDL routine shows a slight centroid shift of $\sim$ 0.5 pixels to lower values in the spectral direction is necessary.

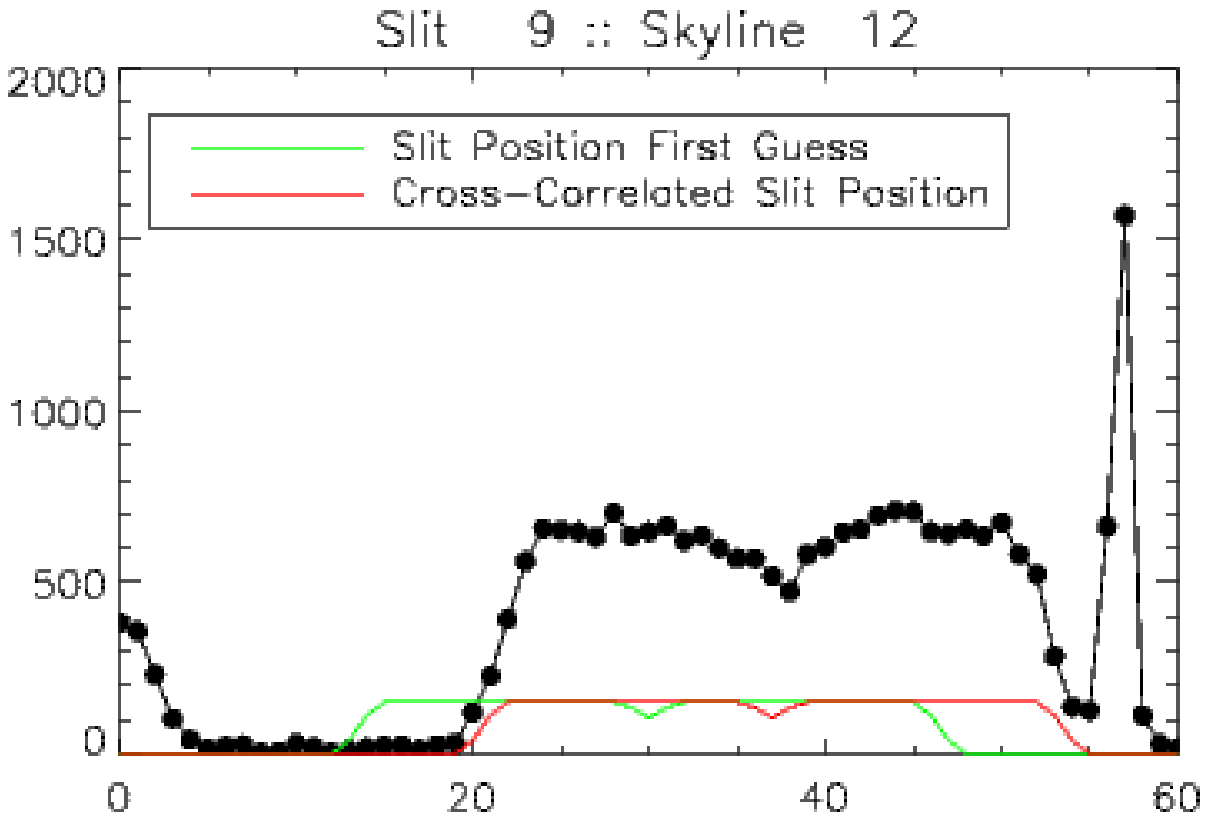

Figure 2.8: IDL custom-written routine vs. COSMOS "adjust-map" centroiding of an OH sky line at $\sim$ 6978.4Å in the spatial direction. The IDL routine shows a centroid shift of $\sim$ 8 pixels to higher values in the spatial direction is necessary.

2.4.1 Stacked Signal Frame

The steps required to create the stacked signal frame were as follows (individual exposure frames are labelled as A and B; the recipe can be extended to N frames):

1. Shift frame A by 16 pixels in the spatial ("y") direction, to get a new frame A_1;
2. Perform the subtraction A - A_1 to get a new frame A_2 (this is the *sky subtracted* frame);
3. Shift frame A_2 by 6 pixels in the spatial ("y") direction, to get a new frame A_3;
4. Perform the subtraction A_2 - A_3 to get a new frame A_4. This frame is the "positive" image frame;
5. Repeat steps (i) through (iv) for all individual exposure frames;
6. Determine if individual frame flux scaling is necessary for each frame based upon the flux level ratios of several *manually* identified emission lines common between the brightest frame and the frame being scaled;
7. Apply further (small) frame shifting if necessary based upon the centroided positions of the identified emission lines used in step 6;
8. Stack (median add) the "positive" image frames, $A_4 + B_4 = C$

The IRAF task "imcombine" was used to median stack the individual "positive" image frames. Since cosmic ray rejection was implemented using a bad pixel mask created using the IRAF "cosmicrays" task, the "imcombine" *crrej* option was disabled. However, the cosmic ray bad pixel mask created in §2.3.2 was utilized by "imcombine" simply by setting the *BPM keyword* to point to the associated cosmic ray BPM in the header of each frame to be stacked, then by setting the "masktype" and "maskvalue" options in "imcombine." Steps (i) to (iv) had already been completed during the wavelength calibration and frame alignment procedure discussed previously. However, they are repeated in the recipe above for clarity. The frame flux scaling mentioned in step (vi) used the same bright emission lines mentioned above which provided the small non-reference-to-reference frame shifts. In the signal frame creation section of Figure 2.9 (top half) the final frame shows a symbol labelled as "2 Object." In this case, "Object" contains half of the exposure time for the frame in question, and hence the final "positive" frame contains the full exposure time.

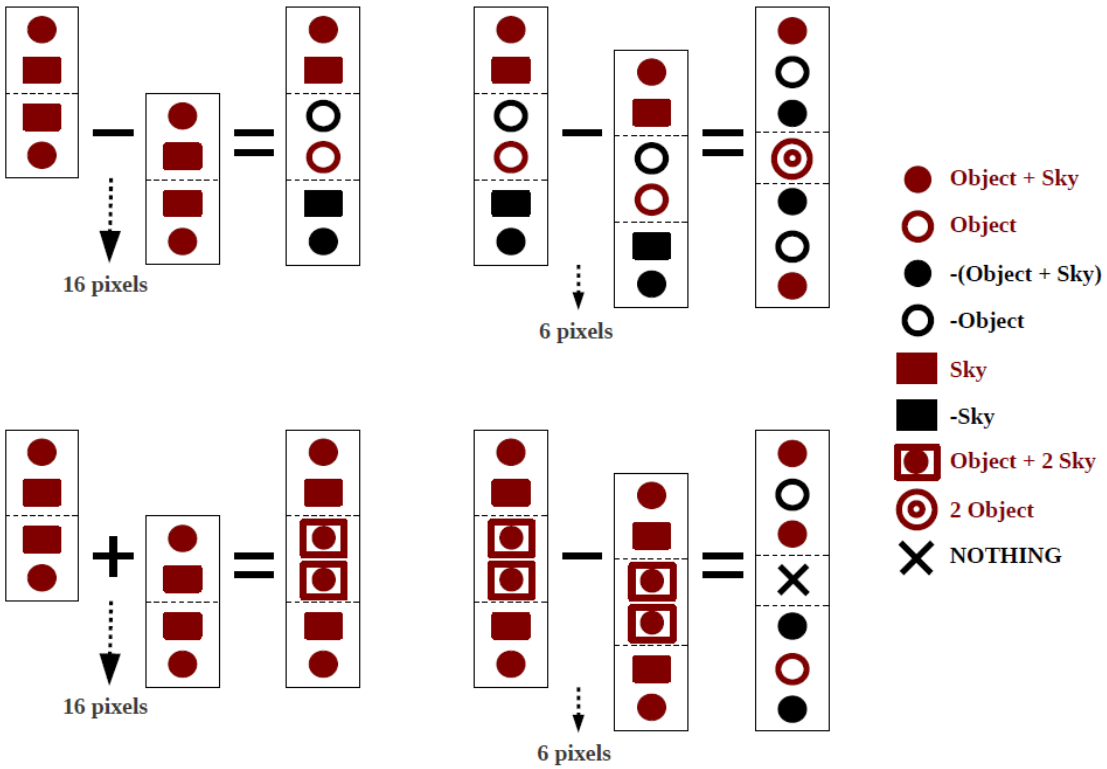

Figure 2.9: The image shifting, addition and subtraction used to obtain the "Nod-Folded" Signal and Noise Frames. The top half of the figure illustrates the steps taken to create the stacked signal frame, while the bottom half shows the basic steps required to create the stacked noise frame.

2.4.2 Stacked Noise Frame

The stacked noise frame was created in a manner similar to the stacked signal frame, except there were additional arithmetic manipulations required. The steps laid out below are identical to those used by Gilbank et al. (2010b) and care has been taken to retain identical naming conventions. Also, in the equations below the subscripts ij refer to the ij^{th} pixel of the frame.

1. Apply the same frame flux scaling, determined in step (vi) of the stacked science frame creation recipe, to each *sky added* frame;

2. Apply the same (small) frame shifts, determined from the locations of common bright emission lines used in step (vii) of the stacked science frame creation recipe, to each *sky added* frame;

3. Stack (median add) the *sky added* image frames to get a new frame, $| < sky > |$;

4. Add in the LDSS-3 read noise, R. The read noise must be added in twice since the median combined frame consists of a shifted frame added to a non-shifted frame, each containing read noise. The read noise adjusted frame is calculated as follows:

$$N_{indiv,ij} = \sqrt{(\sqrt{| < sky > |_{ij}})^2 + 2(R^2)} \tag{2.1}$$

5. Scale frame $N_{indiv,ij}$ by the number of individual science frames used in the median combination, n_{frames},

$$N_{com,ij} = \frac{N_{indiv,ij}}{\sqrt{n_{frames}}} \tag{2.2}$$

6. Shift the frame $N_{com,ij}$ by 6 pixels in the spatial ("y") direction, to get a new frame $N'_{com,ij}$;

7. Perform the quadrature addition of these last two frames to get the final noise frame:

$$N_{ij} = \sqrt{(N_{com,ij})^2 + (N'_{com,ij})^2} \tag{2.3}$$

In the noise frame creation section of Figure 2.9 (bottom half), a large "X" is shown which is labelled as "NOTHING." This implies that there are zero object photons and zero sky photons in this section of the frame. Any counts remaining there are strictly a result of

Poisson counting statistics and are considered the Poisson noise associated with the same pixels in the stacked science frame.

The signal and noise frames were then combined into signal-to-noise frames and searched for emission lines in an automated manner.

Chapter 3

Emission Line Finding

The line-detection procedure was fully dependent upon the measured signal-to-noise of a given mask. For this reason, all of the masks had to have their associated *S/N* frames created at the start of the line-detection procedure. Once this frame was created, it was scanned for detections which were above a user-defined *S/N threshold*. As detections were discovered, they were then run through a series of cutting routines which attempted to remove mis-identified or "spurious" detections from those which were valid. Detections which passed the *S/N threshold* and cutting routine requirements were then catalogued and finally inspected by eye for verification.

3.1 Creation of Signal-to-Noise Frame

After examining the signal frames by eye, it was evident that a typical bright emission line was roughly Gaussian in shape and had a FWHM of ~ 5.5 and 3.5 pixels in the spectral and spatial directions respectively. This information was incorporated into a convolution kernel and used to pick out emission lines in the signal-to-noise (S/N) frame generated for each mask. The creation of S/N frames required a number of steps to estimate continuum and continuum noise, convolved signal and noise, and additional noise factors. These components are described below. Also at this stage, the bad pixel mask determined from the N&S dark frames (see §2.3.2) was applied to the raw science and noise frames before any convolutions were performed.

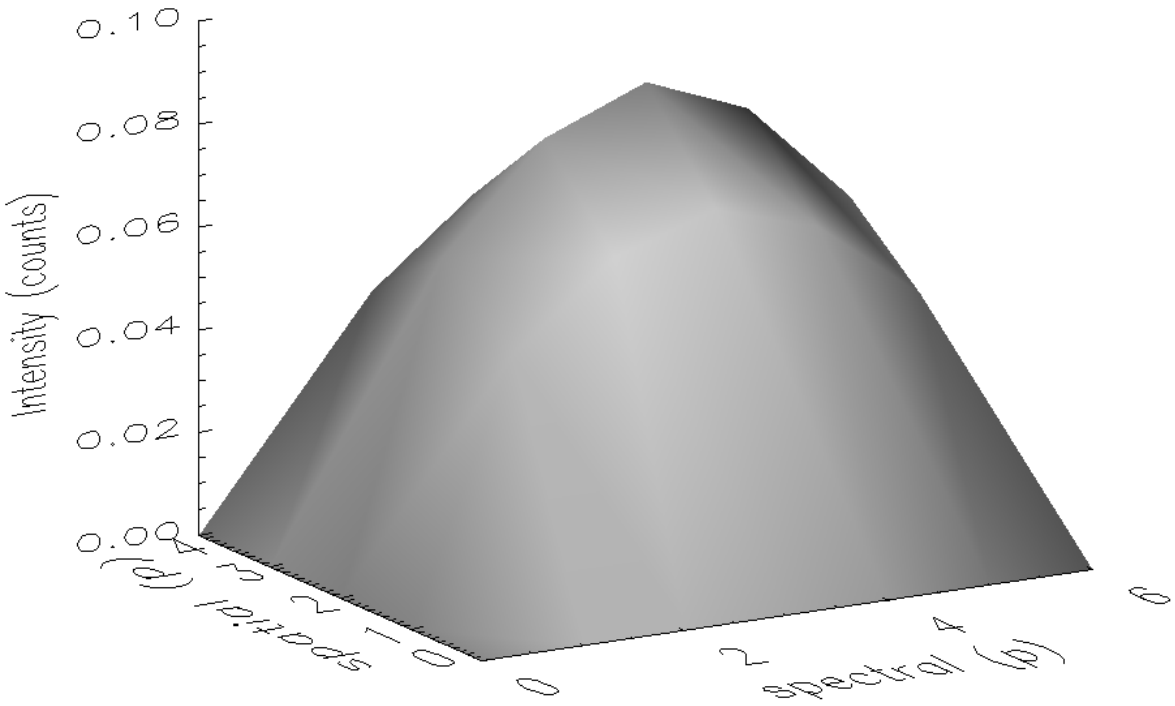

Figure 3.1: The kernel, k_{em}, convolved with the science frames which was used to pick out emission lines. The spectral and spatial pixel intensity distributions are Gaussian with FWHM=[5.5,3.5].

3.1.1 Convolved Signal and Noise Frames

A normalized 2-D convolution kernel, k_{em} (see Figure 3.1), was created which had the same Gaussian shape as a typical bright emission line (FWHM=[5.5p,3.5p]), and was convolved with the signal (S) and noise (N) frames to give flux-conserved, convolved signal and noise frames, according to:

$$S_{conv,ij} = S_{ij} \otimes k_{em} \tag{3.1}$$

$$N_{conv,ij} = \sqrt{N_{ij}^2 \otimes k_{em}^2} \tag{3.2}$$

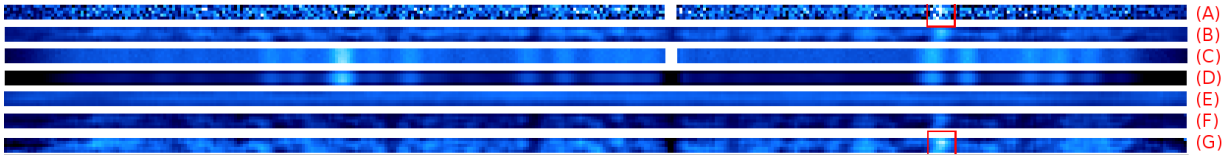

Figure 3.2: A test slit illustrating the: (A) stacked (raw) signal frame; (B) emission line convolved sience frame; (C) stacked (raw) noise section; (D) emission line convolved noise frame; (E) continuum estimation; (F) emission line convolved sience frame with the continuum estimation removed; (G) final signal-to-noise frame. The scales of each image have been selected to make features readily visible and thus are not identical. The white blocks just left of center of images (A) and (C) correspond to bad pixels masked according to §2.3.2. These same features appear as black regions in images (B,D,F,G). An emission line has been highlighted in images (A) and (G).

The benefit of this operation was that it picked out bright and faint emission lines which were buried within the signal frame. The convolution was maximum in sections of the spectra wherever regions of flux closely matched the emission line kernel in shape and intensity distribution (see Figure 3.2).

3.1.2 Estimated Continuum Frame

The next step was to estimate the continuum found in the original signal frame. Similar to the convolution of the signal and noise frames, a convolution was again performed on the raw signal frame,

$$C_{ij} = S_{ij} \otimes k_{cont} \tag{3.3}$$

however the continuum estimation kernel was a 2-D normalized averaging kernel, k_{cont}. The shape of the kernel was motivated by the idea that the continuum was approximately distributed as a Gaussian in the spatial direction and ran the entire length of the dispersed spectra. Any emission lines present would then be considered to be added on top of the already present continuum. Therefore k_{cont} consisted of a *zero* central region (20 pixels spectral by 3 pixels spatial) and two sidebands (also each 20 pixels spectral and 3 pixels spatial). The sidebands had the same Gaussian FWHM of 3.5 pixels in the spatial direction as the emission line kernel for their entire spectral length of 20 pixels. Convolving the kernel with the raw science frame provided an estimation of the continuum for the pixel located at the center of the kernel (in the center of the zero region). The zero region was included so that if there was an emission line present, it did not drag the continuum estimation to

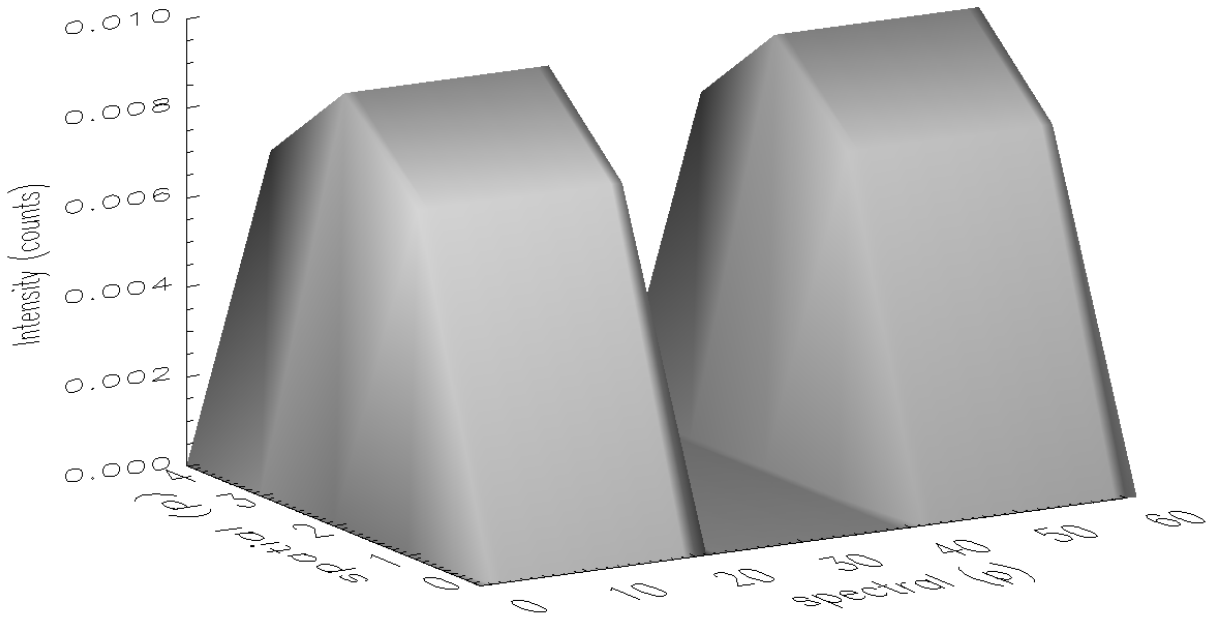

Figure 3.3: The kernel, k_{cont}, was convolved with the science frames and provided an estimate of the continuum. The kernel consisted of a 20 x 3 pixel central zero region, surrounded by two 20 x 3 pixel sidebands. The sidebands had a Gaussian pixel intensity distribution in the spatial direction of FWHM=3.5 pixels, and were uniform in the spectral direction.

a higher value, thus overestimating the continuum at that location. Hence the continuum estimation was essentialy an average of the flux in the spectral and spatial directions, in the "wings" of the pixel for which the continuum was being determined.

One drawback of using the extended averaging kernel was that if a spectrum contained more than one emission line, then the flux from emission lines for which the continuum was *not* being estimated influenced the overall continuum calculation (simply by falling in the sidebands). Additional emission lines were not frequently found in the kernel sidebands, but this effect nonetheless had to be accounted for. To rectify this problem, the convolution was performed twice, with pixel masking occurring before the second convolution. The masked pixels were identified as those which had a signal-to-noise,

$$S/N_{ij} = \frac{S_{conv,ij} - C_{ij}}{N_{conv,ij}} \tag{3.4}$$

greater than six. The convolution was performed again and this result was taken to be the final estimation of the continuum (see Figure 3.2 (E)).

3.1.3 Estimated Continuum Noise Frame

The noise due to the continuum, $N_{cont,ij}$, was calculated by convolving the emission line kernel, k_{em}, with the estimation of the continuum frame, C, as follows:

$$N_{cont,ij} = \sqrt{C_{ij} \otimes k_{em}^2} \tag{3.5}$$

The result was a smoothed version of the estimated continuum frame.

3.1.4 Total Noise Frame

The total noise frame, N_{total}, was calculated by adding in quadrature the convolved raw noise frame with the convolved continuum noise estimate

$$N_{total,ij} = \sqrt{N_{ij}^2 + N_{cont,ij}^2} \tag{3.6}$$

As mentioned in §2.2, the noise was dominated by sky line emission and thus the noise due to the continuum had a minor effect on the overall noise frame.

3.1.5 Noise Correction Factor

At this stage systematic noise had not been fully accounted for in the S/N frame. Systematic noise may have resulted from missed weak charge traps which were not identified by the bad pixel masking routines, skyline remnants from inaccurate sky subtraction due to mis-aligned spectra, or bleeding pixels from overlapping spectra[1].

To determine the presence of this systematic noise, a test was adopted which analysed the science frames looking for excess pixel count fluctuations when compared with the associated pixel values in the noise frames for each mask. The underlying concept was that the average fluctuations from the mean of the stacked science frame should correspond

[1]While unlikely as our analysis only operates on a slit central region of five rows which is well away from the edges of the slit where overlap may occur, it must be considered.

to the average noise value in the stacked noise frame. If this was not the case, then there must exist some systematic effect influencing the noise. To check for this effect, thirty equally spaced "test" locations were chosen along the center line (distributed in the spectral direction) of each slit in a given mask, for both the stacked science and stacked noise frames. The mean pixel value for each slit test location in the science frame was determined by taking the mean of the pixel values within two 60 pixel sidebands, located to either side of the test location. The fluctuation of the test location pixel value from the mean was then simply the actual pixel value subtract the mean value (this was essentially a continuum removal process). For every slit in the mask, the science fluctuation and noise value for thirty test locations were recorded (for a mask with 200 slits, this gave 6000 measurements). Histograms of the science fluctuations and corresponding noise values were then fitted with Gaussians. Finally, the ratio of the best-fit Gaussian standard deviation of the science frame fluctuations and the Gaussian mean of the noise values gave the "noise correction factor", or *NCF* (systematic noise):

$$NCF = \frac{\sigma_{sciencefluctuations}}{\mu_{noise}} \tag{3.7}$$

A typical noise correction factor was ∼1.2, implying that all pixels in the total noise frame had to be multiplied by this factor to account for the sytematic noise.

3.1.6 Signal-to-Noise Frame

The final *S/N* frame was calculated as

$$\left\{\frac{S}{N}\right\}_{ij} = \frac{S_{conv,ij} - C_{ij}}{N_{total,ij} \cdot NCF} \tag{3.8}$$

An example of the result of subtracting the estimate of the continuum from the convolved signal frame (the numerator of Equation 3.8) is shown in Figure 3.2 (F). The final image of the demonstration slit in Figure 3.2 (G) shows the final signal-to-noise frame, where an emission line is evident.

3.2 Emission Line Finding

Once the *S/N* frame for a given mask was created it was scanned for pixels with S/N above the pre-defined *S/N* threshold ≥ 3. Before this could occur, a spectral region

was extracted from each slit. This extracted region was defined as the center five rows and was the full length of the slit (approximately 380 pixels). The center five rows were used since negative "bleeding" pixels commonly entered the spectral region due to the sky subtraction procedure, but rarely impinged upon the center five rows. For every pixel above the S/N threshold, an "n-connected neighbour" search was performed to locate connected neighbouring pixels whose signal-to-noise was also above the S/N threshold, and thus were also a part of the emission line detection[2]. The pixel with the highest signal-to-noise of all connected pixels in a "detection" (group of nearest-neighbour pixels) was set to be the peak pixel. If multiple detections were separated by five pixels or less, then the detections were combined into one large detection, and the peak pixel re-established.

3.2.1 Automated Line Culling

Two line culling steps were implemented during the automated emission line detection process which served to cull the spurious from the real detections.

First, detections found within three pixels of the spectral ends of the slit extraction region were excluded since emission lines were typically $\sim$ 5 pixels wide and thus their entire line profile would not be apparent, making their centroid wavelength and flux difficult to discern.

Second, 0^{th} order spectra were always present toward the left side of the original raw image files (unfortunately the medium red grism combined with the large CCD sensor meant that zeroth order spectra were not dispersed off of the image acquisition area). These unwanted spectra were propagated through the image reduction pipeline and resulted in large ovals or rectangles of high flux. These regions were typically $\sim$ 33 pixels wide in the spectral direction and varied in spatial height depending on whether they perfectly overlapped with an extracted spectral region (at most 5 pixels high). Each detection in the automated emission line list was tested to see if it was actually one of these 0^{th} order spectra by measuring the flux in a 33 x 5 pixel box centered on the detection. The detection was culled if:

1. at least 50% of the pixels in the box had $S/N \geq 3$;
2. the total S/N flux contained inside the box was $\gtrsim$ 40% of the flux the box would have if every pixel had $S/N = 3$.

[2]At least one neighbouring pixel was required to be at or above the S/N threshold in addition to the central pixel.

These line culling levels were determined to be optimal thresholds based upon the ROLES75 spectra.

3.2.2 Detection Culling By Eye

The automated emission line detection process was unable to filter out all spurious detections which may have been created by extensive negative bleeding pixels, overlapping spectra, missed cosmic rays, etc. Thus the detection set was further examined by eye, and any detection which appeared to have been missed by the automated detection culling process was then manually removed from the linelist.

3.2.3 Emission Line Catalog Testing

The 3σ ($S/N \geq 3$) catalog was internally tested in two ways to better understand how many spurious vs. real emission lines our automated line detection algorithm produced. From these tests a final significance cut was applied to the line catalog from which all further analysis was based. These tests and their results were as follows.

The first test examined the recovery rate or reproducibility of emission lines for galaxies which were multiply-imaged. The ROLES75 survey targeted 412 galaxies which were imaged in more than one mask (for a total of 1235 slits). A subset 3σ linelist corresponding to only those galaxies with duplicate targets in other masks was created, and the detection wavelengths were compared between these lines found in multiply-imaged targets. Emission lines were considered to match if their wavelengths were within ± 6.5Å (2.5 pixels) of each other. If a detection was found within all of the masks the galaxy was targeted in, then it was considered fully recovered, otherwise it was considered spurious. As discussed in ROLES1 this is admittedly a very conservative estimate of the number of fully recovered detections in multiply-imaged galaxies since the flux limits across the 18 masks are not all equal and thus a low significance detection found in one mask may not be reproduced in a fainter mask. Also, spurious detection overcounting certainly occurred for the same reason since no exception was allowed for detections which are *partially reproduced* (eg. detections were found in two of three masks, yet all were considered spurious according to this scheme). The results of this test are shown in Figure 3.4 where it is clear that 95% of spurious detections occurred below 5σ.

The second internal test aimed to determine redshifts for targeted galaxies which had more than one emission line in their spectra. The redshifts were determined by searching for detection wavelength ratios which were expected to be observed within the

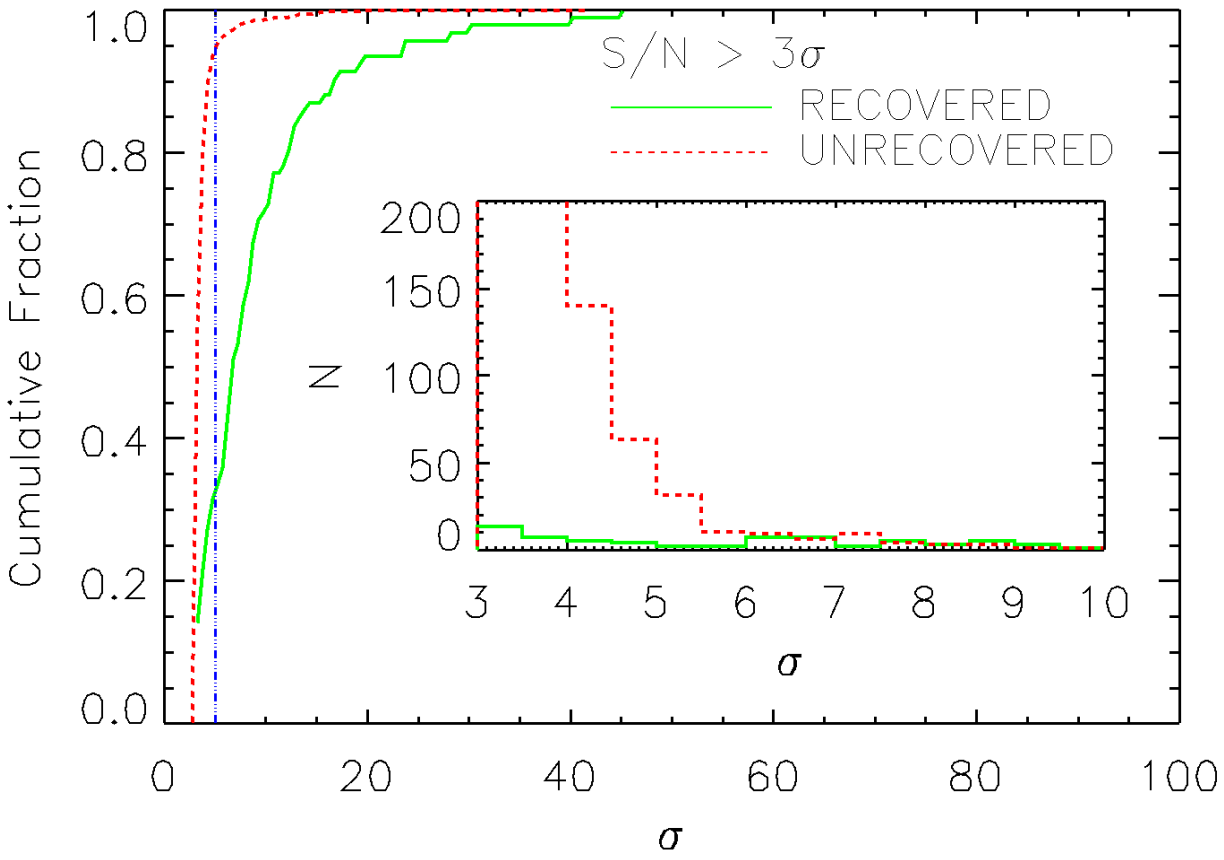

Figure 3.4: (Main Panel) The cumulative fraction of the number of recovered (solid green curve) vs. spurious (dashed red curve) emission lines for galaxies which were targeted in multiple masks, as a function of significance. (Inset) Histogram of the number of recovered and spurious emission lines. It is clear from the cumulative fractions that 95% of spurious detections occur below 5σ (highlighted as the vertical blue '$-\cdots-$' line).

ROLES75 filter window. The emission lines most likely to appear in our survey were the $(H_\beta, [OIII]_{4959}, [OIII]_{5007})$ set (herein known as the $H_\beta - [OIII]$-*complex*) and the $([NeIII]_{3869}, [OII]_{3727})$ combination (referred to as the *[NeIII]-[OII]-pair*)[3]. The algorithm searched slits with two or more detected emission lines and calculated all possible line ratios between them. The lines were then positively identified if their line ratios matched one of the line ratios derived from the expected line combinations. Again, as in ROLES1, emission line combinations which led to self-consistent redshift determinations for the galaxies hosting them were considered as recovered or non-spurious. If a redshift could not be determined from plausible line combinations, then the most significant line was kept as a real line (presumed OII), and all lower significance lines were omitted. To reduce the issue of overcounting of spurious lines, only one emission line was considered to be spurious for a galaxy, regardless of how many actual emission lines were detected and found not to match a plausible line combination. Similar to Figure 3.4, the recovered vs. spurious emission line detection rates, for lines providing self-consistent redshifts for the galaxies hosting them, are shown in Figure 3.5. Again, the cumulative plots show that $\sim 97\%$ of spurious lines occur below 5σ.

Using the set of identified $H_\beta - [OIII]$-complex, [NeIII], and [OII] detections, the second comparison test also allowed the accuracy of the wavelength calibration to be determined. The differences in common identified emission line wavelengths was histogrammed and fitted with a Gaussian. The fitted width was ~ 2Å or 0.8 pixels, resulting in an observed frame velocity difference of 170 km/s, or rest frame 97 km/s at $z \sim 0.75$ (see Figure 3.6).

These two tests concluded that an acceptable emission line significance threshold of $S/N \geq 5\sigma$ imposed upon the ROLES75 3σ linelist would remove most of the spurious detections in the catalog while ensuring that most real lines were being kept. This cut was applied at a later stage after the emission line fluxes of the 3σ catalog had been determined.

3.3 Emission Line Flux Determination

Before the flux for each emission line in the 3σ catalog was determined, a spectrophotometric standard star was selected for the flux calibration. Three standard stars, chosen because of their relative flatness and constancy in the wavelength region of concern (6040-7025Å), were observed throughout the project: FEIGE 110 (Oke, 1990), HD 49798 (Bohlin & Lindler, 1992), and LTT 1788 (Hamuy, 1994). The three sensitivity functions or flux calibration curves corresponding to these standard stars are shown in Figure 3.7. Atmospheric

[3]ROLES75 was unable to resolve the [OII] doublet so this pair was observed as a single emission line.

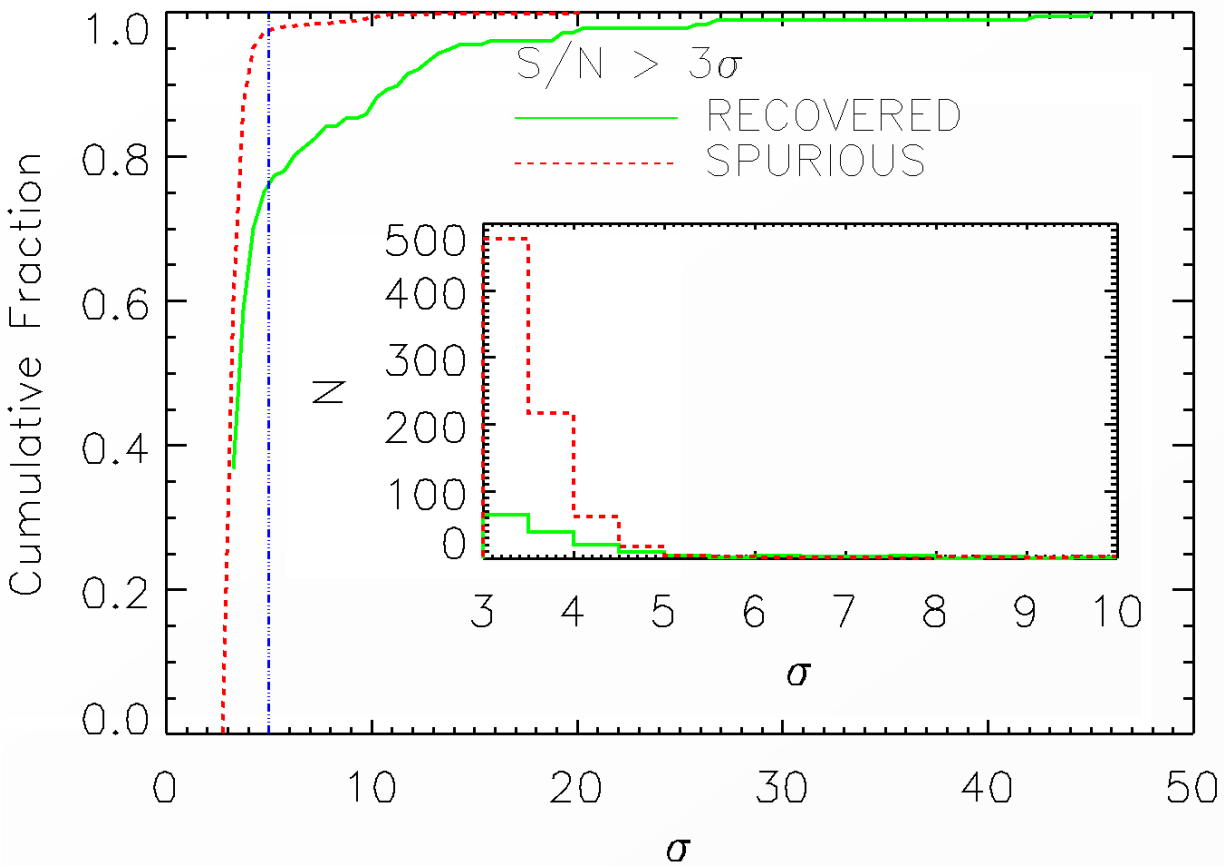

Figure 3.5: (Main Panel) The cumulative fraction of the number of recovered (solid green curve) vs. spurious (dashed red curve) emission lines for galaxies which contain at least two emission lines and lead to self-consistent redshifts, as a function of significance. (Inset) Histogram of the number of recovered and spurious emission lines providing self-consistent redshifts for the galaxies containing them. It is clear from the cumulative fractions that $\sim$ 97% of spurious detections occur below 5σ (highlighted as the vertical blue '$-\cdots-$' line).

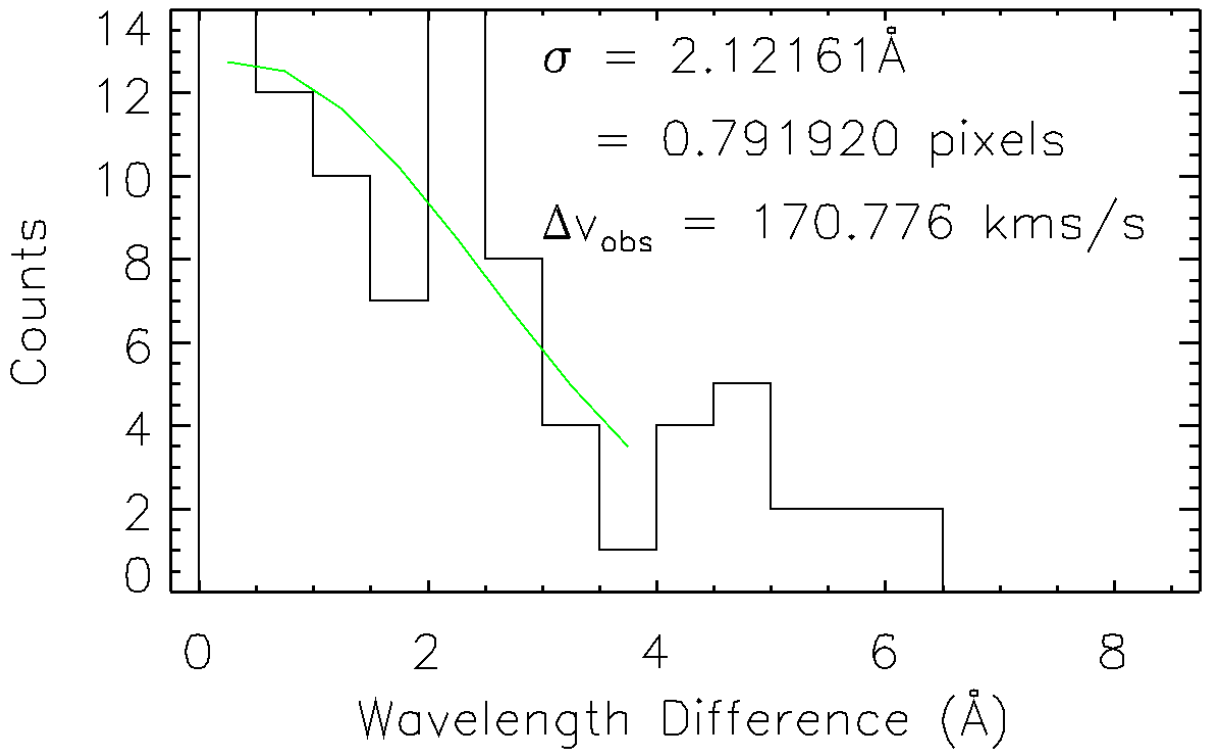

Figure 3.6: Histogram of wavelength differences between identified lines ($H_\beta - [OIII]$-*complex*,[NeIII],[OII]) which were successfully recovered from multiply-imaged galaxies. Overplotted is a fitted Gaussian with width $\sigma \sim 2$Å, corresponding to the accuracy of the ROLES75 wavelength calibration.

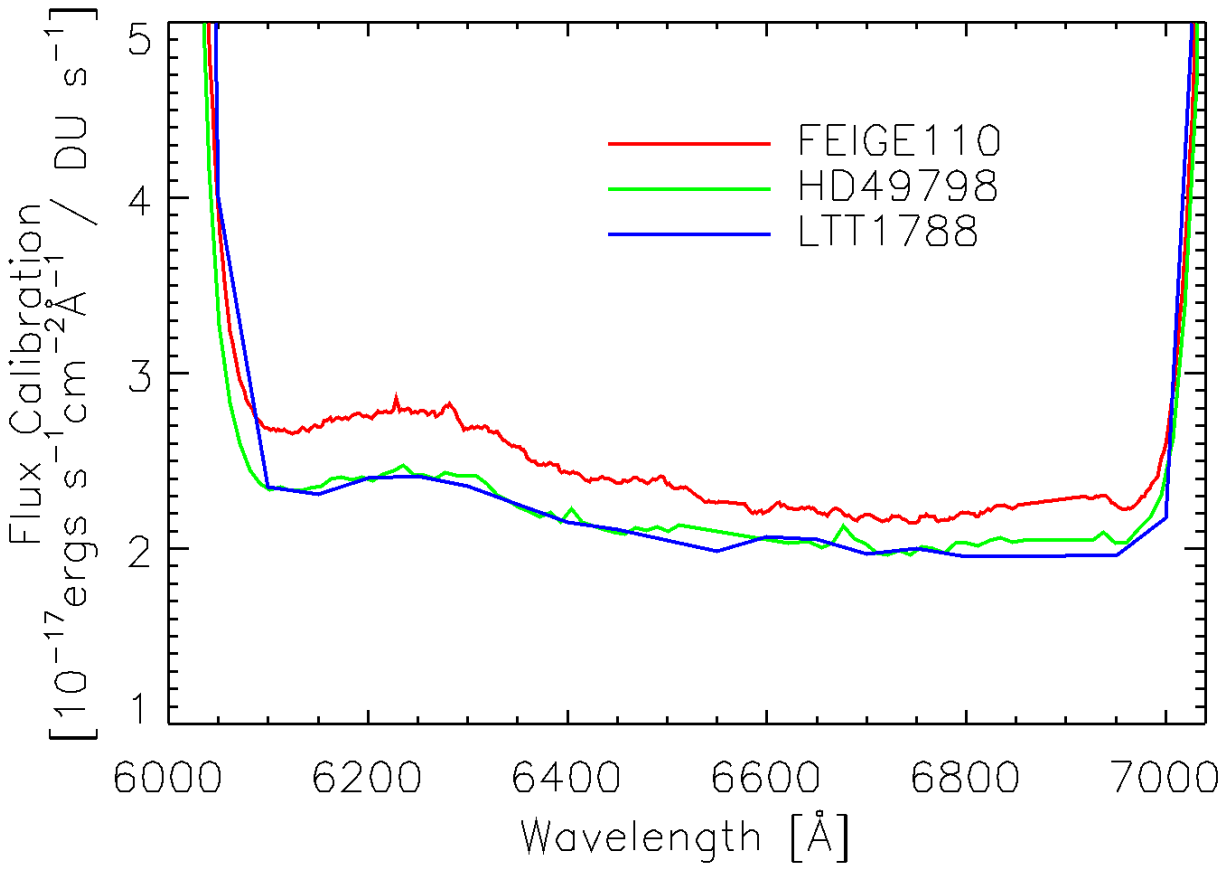

Figure 3.7: Flux calibration curves derived from the three standard stars observed. LTT 1788 and HD 49798 were in excellent agreement while FEIGE 110 showed that this standard star observation may have been done during a time of heavy cloud obscuration.

absorption effects were interpolated over in all three flux calibration curves.

Two of the standard star flux calibration curves, HD 49798 and LTT 1788, were in excellent agreement (see the green and blue curves of Figure 3.7) while the calibration curve derived from FEIGE 110 showed that this standard star may have been acquired at a time of poor seeing or heavy cloud obscuration. The standard star wavelength binning was 2Å, 10-11Å, and 50Å for FEIGE 110, HD 49798, and LTT 1788 respectively. Considering the agreement between the flux calibration curves derived from HD 49798 and LTT 1788, and the relatively small wavelength binning size of the HD 49798 standard, it was ultimately

selected as the standard star used for flux calibration[4].

3.3.1 Detection Flux Measurement

The emission line fluxes and their errors were measured from the stacked raw science frames with the continuum estimation removed, and the stacked raw noise frames. The bad pixel masks from §2.3.2 were applied to ensure the line fluxes were not affected by charge traps, cosmic rays, etc. For each detection, the centroid position of the flux was found within a 15 x 17 pixel box, initially centered on the location of the highest significance pixel in the emission line. Then the flux within a 7 x 5 pixel region (typical size of an emission line) was recorded and summed over the spatial dimension, resulting in a 7 x 1 pixel array. This array was wavelength calibrated, converted from pixel space ($DU/second$) to flux space ($ergs\ s^{-1}cm^{-2}\text{Å}^{-1}$) using the standard star calibration, and integrated to determine the total flux in the emission line. The line flux error was calculated in a similar manner except where summations and integrations occurred over the spatial and spectral directions respectively, quadrature sums were implemented in their place.

An "aperture correction" was also necessary during the conversion from pixel space to flux space since the standard star PSF was larger than the mask slit (recall that the slits were 0.8" x 3", or 4 x 16 pixels in size) through which it was observed. The image of the observed standard star, HD 49798, was examined in IRAF and its radial profile fitted with a Gaussian of width $\sigma \sim 2.2$ and $FWHM \sim 5.2$ pixels. The flux contained within a 2-D Gaussian defined by these parameters was integrated over infinity and compared to the flux contained within the same 2-D Gaussian bounded by the 4 x 16 pixel slit size. The ratio of these values, found to be ~ 1.5, provided the aperture correction factor needed to adjust all point-source fluxes measured through slits to "unobstructed" fluxes. Of course this is a seeing dependent correction and ideally would only be applied if the seeing for a particular target was larger than the slit size. This is impractical however, and given the average seeing values listed in Table 2.2, it was reasonable to apply this small aperture correction to all line fluxes.

[4]It is worth mention that the LTT 1788 standard star could have been used as well. While the 50Å wavelength binning size was large, the relative flatness and smoothness of the sensitivity function would still have allowed an accurate flux calibration over the wavelength range of concern.

3.3.2 Mask-to-Mask Flux Correction

The ROLES75 masks were acquired on different observing runs with differing photometric conditions. As such, emission lines detected in galaxies targeted on more than one mask were often found to have varied measured fluxes. To account for this, correction factors were determined from R-band flux measurements for the six FIRES and 12 CDFS masks.

The R-band filter used by Wuyts et al. (2008, eg. FIREWORKS) almost exactly overlapped the wavelength range used in our ROLES75 survey. Therefore a measurement of the continuum flux in a ROLES75 slit was close to a measure of the R-band flux of the galaxy through the slit. Every ROLES75 CDFS target had its continuum measured in the same way emission line fluxes had been determined, except the full spectral range of the slit was used rather than just the range defined by an emission line. The aperture correction of ~ 1.5 from the previous section §3.3.1 was applied to the measured flux of each slit, ensuring that the total magnitude derived from a slit corresponded to that of a point source observed under similar seeing conditions as those of the standard star. We note that this correction factor does not apply to larger galaxies and thus their measured fluxes are expected to be fainter than their corresponding photometry as their flux extends outside of their respective slits. The flux measurement of each slit in every mask was then converted to an R_{AB} magnitude. The ROLES75 CDFS R-band magnitudes were compared to the public values from the FIREWORKS dataset and plotted as a function of galaxy half-light radius (HLR), in Figure 3.8, on a per mask basis. To determine the flux correction between masks targeting the same field (eg. CDFS), the half-light radius was divided into small bins and the mean R-band magnitude difference was determined for each bin. Then a line ($y = mx + b$) was fitted to all of the R-band difference measurements within 3σ of the mean R-band difference calculated for each bin. Next, lines were similarly fit to each of the individual mask R-band measurement sets, using the same 3σ selection, with the slope constrained to be equal to the slope of the line fit through all of the measurements (no mask segragation; fixed to m = -1.5215). Thus only the R-band magnitude difference between ROLES75 and FIREWORKS (y-intercept) was fit. Finally, the y-intercept represented the flux correction needed for galaxies with $HLR = 1''$ found in that mask to match the ROLES75 photometry to the FIREWORKS dataset. More importantly, for unresolved galaxies wih $HLR \sim 0.3''$, their flux corrections were derived from these mask-dependent fits and typically ranged from 0.4-1.2 magnitudes for ROLES75 CDFS targets. Table 3.1 lists the y-intercepts, or magnitude shifts needed to adjust the ROLES75 ($HLR \sim$ 0.3 and $1''$) magnitudes to FIREWORKS magnitudes. Ideally if a CDFS and a FIRES mask had both been imaged completely in the same night, we would have a method of comparing and calibrating all ROLES75 CDFS and FIRES fluxes to public photometry.

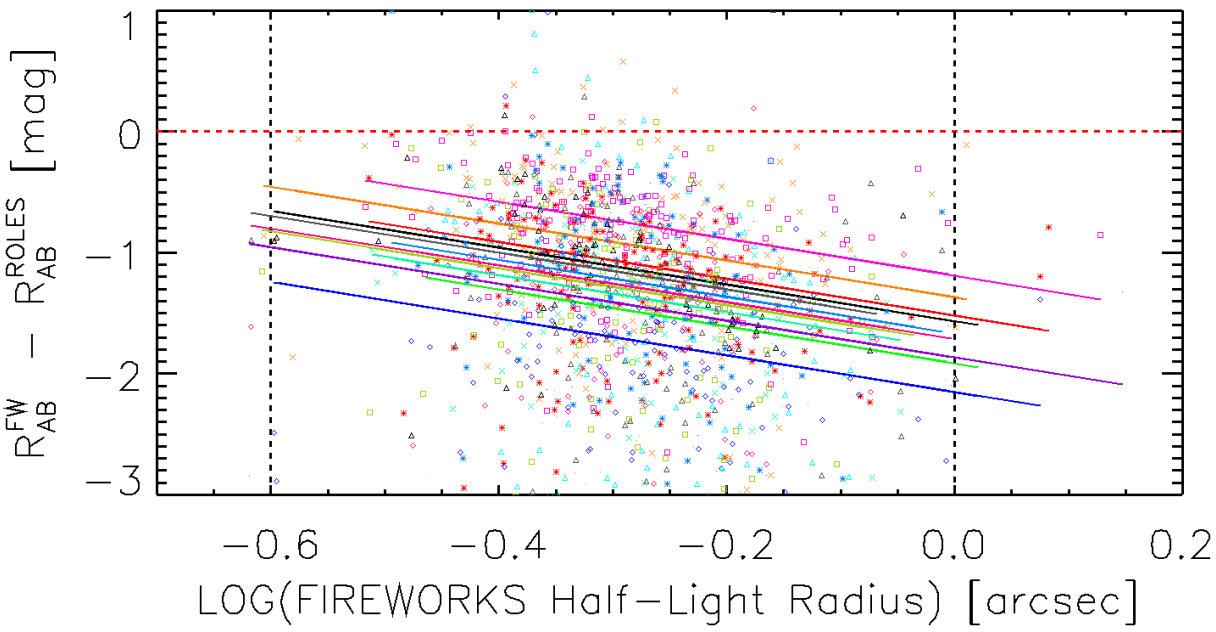

Figure 3.8: Difference between FIREWORKS and ROLES CDFS target R_{AB} measurements as a function of FIREWORKS galaxy half-light radius. The ROLES CDFS measurements were divided into their respective masks where the slope had been fixed and a magnitude shift had been determined to adjust the flux of the faintest CDFS mask to the most photometric. The fitted y-intercepts are shown in Table 3.1.

Unfortunately this situation never arose and as a result we decided to only correct for varied photometric conditions in our survey on a mask-by-mask basis within each of the CDFS and FIRES fields separately. Hence all ROLES75 CDFS emission line fluxes and their errors were corrected according to

$$\begin{aligned} F_{corr} &= F_{orig.} \times 10^{\frac{\left(y_{int.,brightest} \; - \; y_{int.,m}\right)}{2.5}} \\ &= F_{orig.} \times 10^{\frac{\left(\Delta R^{brightest}_{unresolved} \; - \; \Delta R^{m}_{unresolved}\right)}{2.5}} \end{aligned} \tag{3.9}$$

where F is the line flux, $y_{int.,brightest}$ and $\Delta R^{brightest}_{unresolved}$ corresponded to the mask with the y-intercept and unresolved target magnitude difference closest to zero (also the most photometric mask), and $y_{int.,m}$ and $\Delta R^{m}_{unresolved}$ were the y-intercept and unresolved target magnitude difference for a fainter mask m targeting the same field (eg. CDFS).

The analysis was identical for the ROLES75 FIRES masks with two important ex-

Table 3.1: Mask colors and symbols associated with Figure 3.8. Also listed are the fitted R-band magnitude differences (y-intercept) between targets with HLR=1" in ROLES75 CDFS masks and their matching FIREWORKS targets. This y-intercept has been translated to unresolved targets with $HLR \sim 0.3''$ and tabulated under the heading ΔR_{AB} *unresolved*.

Mask	Y-Intercept (ΔR_{AB})	ΔR_{AB} *unresolved*	Symbol	Color
30	-1.1883	-0.4276	$\square$	pink
31	-1.3672	-0.6064	$\times$	orange
32	-1.5192	-0.7584	$*$	red
33	-1.9132	-1.1524	$\bullet$	green
34	-2.1518	-1.3910	$\diamond$	blue
35	-1.5665	-0.8058	$\triangle$	turquoise
36	-1.7373	-0.9766	$\square$	green
37	-1.7937	-1.0330	$\times$	coral
38	-1.6682	-0.9074	$*$	blue
39	-1.8653	-1.1046	$\bullet$	purple
40	-1.7121	-0.9514	$\diamond$	pink
41	-1.6071	-0.8464	$\triangle$	charcoal

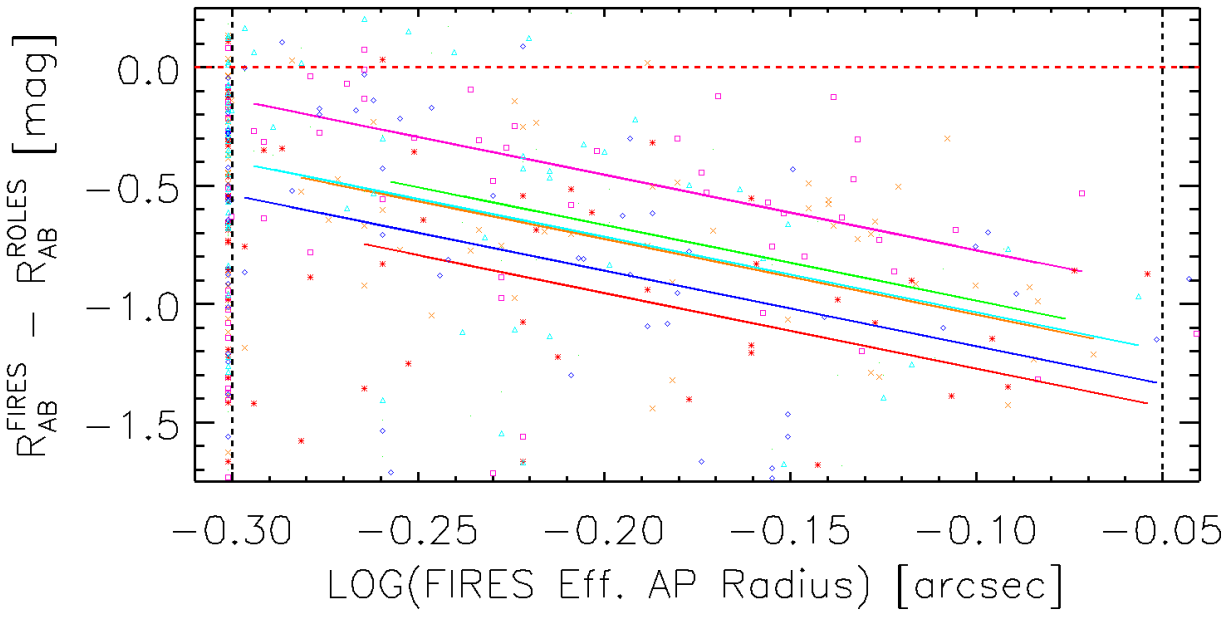

Figure 3.9: Difference between Förster Schreiber and ROLES FIRES target R_{AB} measurements as a function of Förster Schreiber galaxy effective aperture radius. The ROLES FIRES measurements were divided into their respective masks where the slope had been fixed and a magnitude shift had been determined to adjust the flux of the faintest FIRES mask to the most photometric. Table 3.2 lists the unresolved target magnitude differences (fitted y-intercepts).

ceptions. First, the Förster Schreiber FIRES photometry did not contain measured R-band magnitudes. However there was photometry for two bracketing bands from the HST WFPC2 F606W (λ_{eff} = 6030Å,$\delta\lambda$ = 1500Å) and F814W (λ_{eff} = 8040Å,$\delta\lambda$ = 1540Å) filters. These filters, V_{606} and I_{814}, were similar in spectral width to the ROLES75 KG650 filter ($\delta\lambda \approx 1000$Å) and were used to determine an interpolated R-band magnitude (with the same central wavelength and width as the KG650 filter). Second, the lowest effective aperture radius (which is different than the half light radius used in the CDFS analysis) was 0.5". Figure 3.9 and Table 3.2 convey the FIRES results of the same analysis as used for CDFS. Again, all ROLES75 fluxes from FIRES masks were corrected using Equation 3.9 with the corresponding unresolved target ($Eff.Ap.Radius \sim 0.5''$) magnitude differences (fitted y-intercepts) for the FIRES masks. The fitted slope in this case was fixed to $m = -3.1925$.

Figures 3.8 and 3.9 show that the ROLES75 measured R-band fluxes for targets with

Table 3.2: Mask colors and symbols associated with Figure 3.9. Also listed are the fitted R-band magnitude differences between targets (with $Eff.Ap.Radius \sim 0.5$ and $1''$) in ROLES75 FIRES masks and the corresponding Förster Schreiber targets.

Mask	Y-Intercept (ΔR_{AB})	ΔR_{AB} *unresolved*	Symbol	Color
24	-1.0926	-0.1382	$\square$	pink
25	-1.3640	-0.4062	$\times$	orange
26	-1.5921	-0.6344	$*$	red
27	-1.3047	-0.3470	$\bullet$	green
28	-1.4976	-0.5398	$\diamond$	blue
29	-1.3546	-0.3968	$\triangle$	turquoise

HLR / Eff. Ap. Radius $= 1''$ were typically fainter than the public photometry by $\Delta R_{AB} \sim 1.0-2.0$ (a factor of $\sim 2.5-6.3$). For unresolved galaxies (HLR $\sim 0.3'', $Eff. Ap. Radius $= 0.5''$), the differences range by a factor of $\sim 1.2-3.6$. Later in §4.4 we discuss the extension of the ROLES75 dataset to higher stellar masses by using an emission line (EL) galaxy sample from the GOODS Team (see Vanzella et al., 2008). The overlap of only three EL galaxies between the ROLES75 sample and this higher mass dataset unfortunately meant that we were unable to resolve the discrepancy in measured ROLES75 R-band fluxes with the public photometry. The differences in measured line flux resulted in a large scatter, and not in a manner suggesting that ROLES75 was consistently fainter than the comparison sample. One conclusion that might be drawn from the difference in measured R-band flux is that all ROLES75 masks were imaged in non-photometric conditions, suggesting heavy cloud cover and/or poor seeing. However, it seems highly unlikely that *all* of the ROLES75 masks would be non-photometric. Considering the average seeing listed previously in Table 2.2, 10 of the 18 ROLES75 masks had an average seeing of $\lesssim 0.8''$. These are considered to be good quality observing conditions as the seeing disk would be fully contained within the ROLES75 slit. As a result it remains unclear as to why the measured ROLES75 R-band fluxes are typically fainter by a factor of $\sim 1.5-3$ than their matched public photometry.

3.3.3 5σ Detection Catalog and Emission Line Flux Noise Check

At this stage the 3σ emission line catalog (3737 detections, approximately one detection per slit) was cut to a $\geq 5\sigma$ list (400 detections, approximately one detection per 10 slits) based upon the test results of §3.2.3.

From this 5σ linelist, an emission line flux noise check was performed to ensure that an accurate estimate of the noise had been used and that it had been propagated through the analysis correctly. Identical emission lines found within multiply-imaged galaxies were used for this test (a 5σ version of the linelist used in the first test of §3.2.3). The differences in the matching emission line fluxes were determined and plotted against the line flux, as shown in the main panel of Figure 3.10. As expected, the matching line flux differences were scattered about zero. The matching line flux errors were then added in quadrature, taken in ratio with the line flux difference, and histogrammed as shown in the inset of the same figure. It was expected that the line flux quadrature error would have described the typical flux difference between matching lines, and thus the histogram should have been standard normal (shown as the overplotted dashed green curve in the inset of Figure 3.10). A Gaussian was fitted to the sample (red curve of the inset plot) which resulted in a standard deviation of $\sigma \sim 1.28$. A Kolmogorov-Smirnov test found a high probability (P=0.883) of the sample actually arising from a normal distribution, suggesting it is unlikely that we have missed any additional sources of noise.

3.4 Line Identification

The emission lines of the $\geq 5\sigma$ catalog were identified using three methods. The first method was used by the second test in §3.2.3 where self-consistent target redshifts were provided by the presence of multiple emission lines having been detected in a galaxy. Redshifts were established if the detections had line wavelength ratios corresponding to the line combination ratios commonly expected to occur within the ROLES75 spectral window. Only 41 (15 identified as [OII]) of the ROLES75 $\geq 5\sigma$ emission lines were found to provide self-consistent redshifts for their host galaxies. The remainder of the catalog consisted of single emission lines which led to ambiguous identification.

The second identification technique used the photometric redshift probability distribution functions (PDFs) associated with each ROLES75 target galaxy. The most probable emission lines in our redshift window were $[\mathrm{CIV}]_{\lambda 1550\text{Å}}$, $[\mathrm{NeIII}]_{\lambda 3869\text{Å}}$ / $[\mathrm{OII}]_{\lambda 3727\text{Å}}$, and $[\mathrm{H}_\beta]_{\lambda 4861\text{Å}}$ / $[\mathrm{OIII}]_{\lambda 4959,5007\text{Å}}$. The [NeIII] and [OII] lines were grouped together since their redshift ranges overlapped and hence their combined redshift range ($0.56 < z < 0.885$) was bounded by the minimum allowed redshift of [NeIII] and the maximum allowed redshift of [OII]. The H_β / $[\mathrm{OIII}]_{\lambda 4959,5007\text{Å}}$ *complex* was grouped together for the same reason, giving an applicable redshift range of $0.2 < z < 0.45$. The [CIV] line was restricted to $2.9 < z < 3.53$ and of course $[\mathrm{OII}]_{\lambda 3727\text{Å}}$, the line we were searching for, had an applicable redshift range of $0.62 < z < 0.885$. The [CIV] line was rare in our final catalog,

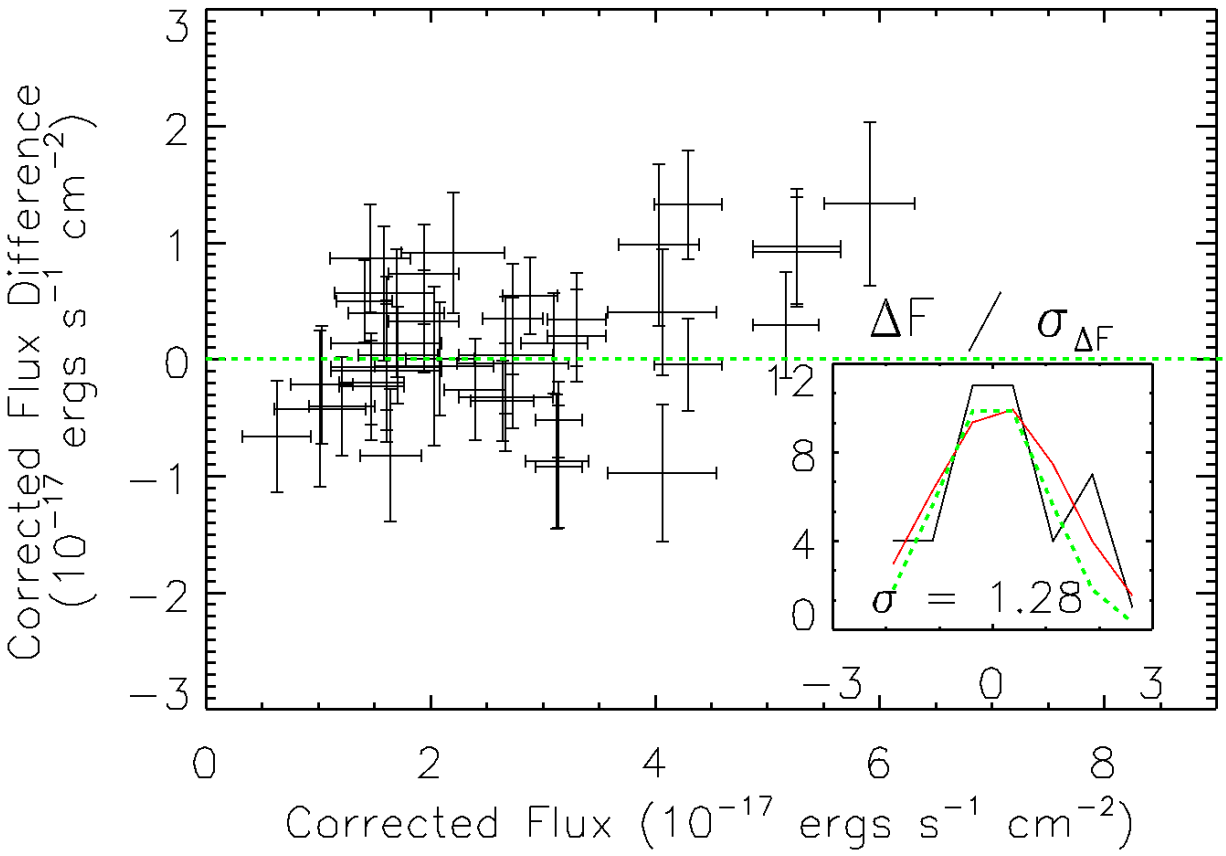

Figure 3.10: (Main Panel) The difference in $\geq 5\sigma$ emission line fluxes for matching detections found in multiply-imaged galaxies as a function of line flux. The zero difference line is shown as the horizontal green dashed line. (Inset) Histogram of the flux differences divided by the quadrature sum of the emission line flux errors. Ideally if a large sample size had been available, the histogram would have been normal with $\mu = 0.0$ and $\sigma = 1.0$ (shown as the dashed green curve) under equal photometric conditions for all masks. The red curve is the Gaussian fit to the sample, from which $\sigma \sim 1.28$.

but was nonetheless considered in the analysis. These ranges are highlighted (sequence of shaded regions) in Figure 3.11 which shows three examples of photometric redshift PDFs suggesting a high likelihood that the galaxy should contain a line from the (Upper Panel) $[H_\beta]_{\lambda 4861\text{Å}}$ / $[OIII]_{\lambda 4959,5007\text{Å}}$ set, (Middle Panel) $[NeIII]_{\lambda 3869\text{Å}}$ / $[OII]_{\lambda 3727\text{Å}}$ set, or (Lower Panel) the $[CIV]_{\lambda 1550\text{Å}}$ line. Note that in the top panel of this figure the PDF shows a small but non-zero probability that the galaxy may contain the [CIV] line rather than one of the $H_\beta - [OIII]$-*complex* lines.

A likelihood of being [OII] was assigned to each detection in our 5σ catalog by determining the ratio of the probability of the emission line being [OII] to the total probability of being any one of the lines mentioned above. The probabilities were calculated by integrating the photometric redshift PDFs over the redshift ranges corresponding to the lines of interest in our spectral window. Thus the likelihood of a detection being [OII] was

$$\mathcal{L}[OII] = \frac{\int_{z_{OIImin}}^{z_{OIImax}} P(z)dz}{\sum_k \left(\int_{z_{k,min}}^{z_{k,max}} P(z)dz \right)} \tag{3.10}$$

where $\mathcal{L}[OII]$ is the likelihood, P(z) is the photometric redshift PDF for the galaxy, and k is an index describing the line(group) to use (eg. $[CIV]_{\lambda 1550\text{Å}}$, $[NeIII]_{\lambda 3869\text{Å}}$ / $[OII]_{\lambda 3727\text{Å}}$, or $[H_\beta]_{\lambda 4861\text{Å}}$ / $[OIII]_{\lambda 4959,5007\text{Å}}$). For the purpose of simplification, where $\mathcal{L}[OII] < 0.1$, then $\mathcal{L}[OII] = 0$. Similarly, where $\mathcal{L}[OII] > 0.9$, then $\mathcal{L}[OII] = 1$. It should be noted that this was the same prescription used in ROLES1.

The third line identification method involved matching ROLES75 detections to public spectroscopy for the FIRES and CDFS fields[5]. Spectroscopy for the FIRES and CDFS fields were matched to the public catalogs published by Crawford et al. (2011, eg. MS1054-03) and Wuyts et al. (2008, eg. FIREWORKS). Of the ROLES75 catalog, only nine detections in the FIRES field had a matching spectroscopic redshift in the Crawford et al. (2011) catalog, while 73 detections in CDFS had a FIREWORKS spectroscopic redshift of the highest quality (z_{sp} quality flag = 1). The matched spectroscopy was verified in Figure 3.12 which shows the redshifts which correspond to the observed ROLES75 detection wavelengths for seven considered emission line identifications. In this identification process we temporarily assumed that *all* ROLES detections were [OII]. In the figure, the angled lines represent the redshift an assumed [OII] detection would have had if it were actually

[5]Due to the ROLES75 survey targeting low mass galaxies, there was not extensive overlap of ROLES75 targets with public catalogs.

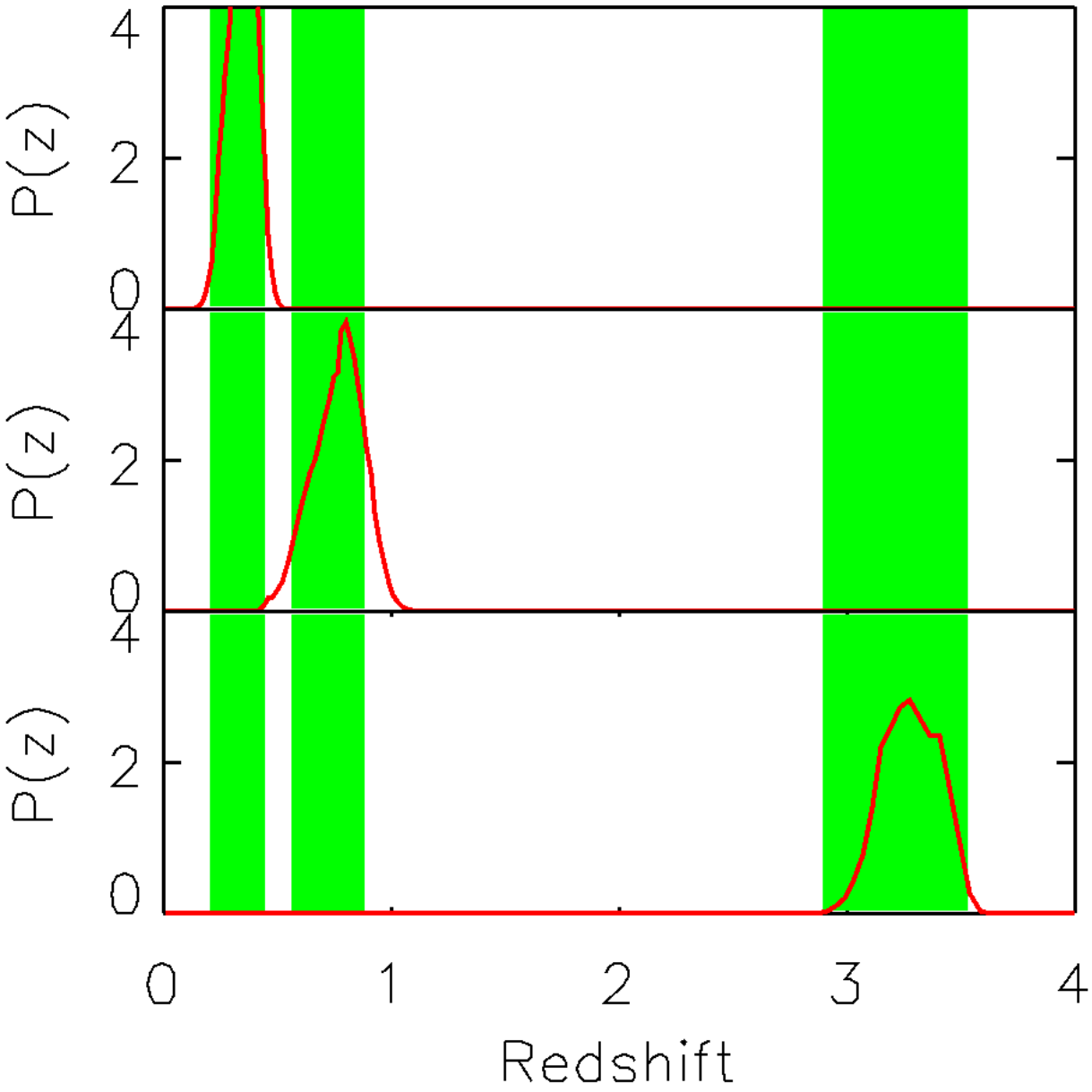

Figure 3.11: Three examples of photometric redshift PDFs indicating a high likelihood of a galaxy containing: (Upper Panel) $[H_\beta]_{\lambda 4861\text{Å}}$ / $[OIII]_{\lambda 4959,5007\text{Å}}$, (Middle Panel) $[NeIII]_{\lambda 3869\text{Å}}$ / $[OII]_{\lambda 3727\text{Å}}$, (Lower Panel) $[CIV]_{\lambda 1550\text{Å}}$. The probability density function, P(z) (in arbitrary units), is plotted vs redshift.

Table 3.3: ROLES75 emission line identifications.

Line ID	Description	Line ID	Description
-1	UNKNOWN	4	$[\mathrm{OII}]_{\lambda 3727\text{Å}}$
1	$[\mathrm{H}_\beta]_{\lambda 4861\text{Å}}$	5	$[\mathrm{NeIII}]_{\lambda 3868\text{Å}}$
2	$[\mathrm{OIII}]_{\lambda 4959\text{Å}}$	6	$[\mathrm{CIV}]_{\lambda 1550\text{Å}}$
3	$[\mathrm{OIII}]_{\lambda 5007\text{Å}}$		

another emission line type (eg. [NeIII], [OIII], etc.). The angled black dashed line shows the ROLES75 [OII] confirmation redshift line. The detections denoted by asterisks were those which had an integrated photometric redshift probability of being [OII]. Detections bounded by squares highlighted those which did not have an obvious line identification (did not fall on when of the angled redshift lines) and were highly likely to be spurious.

Many of the detections in this set contained the $[\mathrm{H}_\beta]_{\lambda 4861\text{Å}}$ / $[\mathrm{OIII}]_{\lambda 4959,5007\text{Å}}$ and $[\mathrm{NeIII}]_{\lambda 3869\text{Å}}$ / $[\mathrm{OII}]_{\lambda 3727\text{Å}}$ combinations of emission lines, which meant that they provided a self-consistent redshift for the target galaxy. These detections appeared on the lower five angled lines in the figure. If any of these (self-consistent) emission line identifications differed from the public redshift, then the ROLES identification was kept. In cases where the (already assumed [OII]) ROLES75 identification of a line differed than the public identification, and the lines could not be identified by a multiple-line ratio, then the public redshift was used.

Most of the emission lines which had a high probability of being [OII] ($\mathcal{L}[OII] > 0.9$) fell on the ROLES75 [OII] confirmation redshift line, validating the photometric redshift PDFs of the target galaxies. Of the 82 matched detections shown in the figure only three had a redshift which did not match the public catalog and also could not be matched using a multi-line ratio.

3.5 Final 5σ Catalog

The $S/N \geq 5$ cut was applied to the emission line catalog with each detection having a line identification (and redshift) described in Table 3.3.

The detections were also given a *line quality* described by the following:

1. 0 = Line does not have a photometric or spectroscopic match in FIRES or FIREWORKS, nor does it meet integrated photo-z expectations of being [OII];

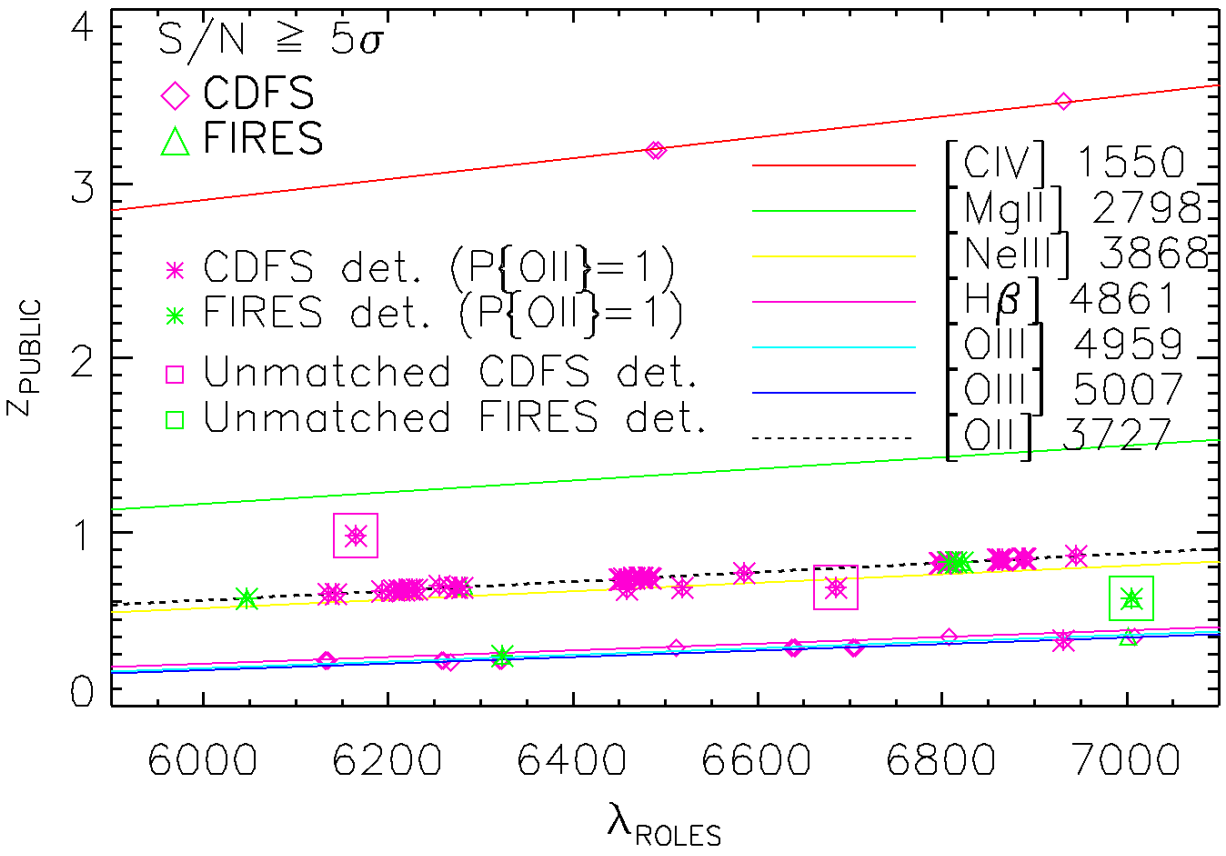

Figure 3.12: ROLES75 emission line identification. Angled lines show the redshift that would be associated with a given observed wavelength, for seven different emission lines as indicated. The seven emission lines considered are identified in the legend and correspond to [CIV] at the highest redshift, and $[\mathrm{OIII}]_{\lambda 5007\mathrm{A}}$ at the lowest redshift. The [OII] confirmation redshift line has been highlighted as the angled dashed line. Asterisks correspond to ROLES75 detections with $\mathcal{L}[OII] > 0.9$, while detections bounded by large boxes represent those which remained unidentified and were likely spurious.

2. 1 = Line has a photometric match in FIRES or FIREWORKS, and meets the integrated photo-z expectations of being [OII];

3. 2 = Line has a photometric match in FIRES or FIREWORKS, meets the integrated photo-z expectations of being [OII], and is verified by multiple lines in the same galaxy;

4. 3 = Line has a spectroscopic match in FIRES (Crawford et al., 2011, eg. MS1054-03) or FIREWORKS, has a photometric match in FIRES or FIREWORKS and meets the integrated photo-z expectations of being [OII].

The highest quality emission line in our catalog had *line quality = 3*.

Chapter 4

Analysis

Spectroscopic redshifts determined for the galaxies in our 5σ linelist, as well as photometry in the CDFS field from the FIREWORKS catalog (Wuyts et al., 2008, U_{38}, B_{435}, B, V, V_{606}, R, i_{775}, I, z_{850}, J, H, K_s, $[3.6]\mu m$, $[4.5]\mu m$, $[8.0]\mu m$), and in the FIRES field (Förster Schreiber et al., 2006, U, B, V, V_{606}, I_{814}, J_s, H, and K_s), served as inputs to the stellar population models implemented in (PEGASE.2, Fioc & Rocca-Volmerange, 1997, and described in detail in Glazebrook et al. 2004). The input photometry was aperture-based and thus any luminosity-dependent SED-fit derived quantities such as stellar mass[1] had to be converted to total light related values. Hence ROLES75 corrected the stellar masses obtained from PEGASE.2 according to

$$M_{*,corr} = M_* \left[10^{-0.4(K_{total}-K_{aperture})}\right] \tag{4.1}$$

where $M_{*,corr}$ and M_* were the corrected and original SED modelled stellar masses, while K_{total} and $K_{aperture}$ were the CDFS or FIRES K_s band total and aperture magnitudes respectively.

The ROLES75 emission line luminosities were initially converted to star formation rates (SFR) using the same [OII] luminosity to SFR conversion as that used in ROLES1 (see Equation 9 of that paper),

$$SFR(M_\odot yr^{-1}) = \frac{10^{0.4A_{H\alpha}}}{0.5} \times \frac{7.9 \times 10^{-42}}{1.82} \times L([OII])(ergs^{-1}) \tag{4.2}$$

[1]PEGASE.2 only accounts for luminous stars in its determination of stellar mass. Thus stellar remnants such as white dwarfs, neutron stars, and black holes were not included.

This conversion was identical to that used by Juneau et al. (2005) which was based upon the Kennicutt (1998) conversion of $L[H_\alpha]$ to SFR. As in Juneau et al., here it was assumed that $L[H_\alpha]/L[OII] = 0.5$ and the luminosity was corrected for dust attenuation by assuming $A_{H_\alpha} = 1$. The factor of 1.82 accounted for the conversion from a Salpeter IMF (Salpeter, 1955) to the BG03 IMF (Baldry & Glazebrook, 2003) used in our SED-fitting.

In Gilbank et al. (2010a, Eq.8) it was determined that the L[OII]-based SFR was dependent upon stellar mass. The simple scale factor in Eqn. 4.2 was found to overestimate the SFR at low stellar masses, and underestimate the SFR at higher masses. The stellar mass-dependent empirical correction (found in Gilbank et al. (2010a)) was applied to all ROLES75 SFR's as follows

$$SFR_{corr}(M_\odot yr^{-1}) = \frac{SFR}{\{(a) \cdot tanh[(X+b)/c] + d\}} \tag{4.3}$$

where $X = log(M_*/M_\odot)$, $a = -1.424$, $b = -9.827$, $c = 0.572$, and $d = 1.700$.

4.1 Completeness

The method used in ROLES1 to calculate the spectroscopic completeness of the ROLES survey was adopted for the ROLES75 analysis. The method combined targeting completeness with a redshift success rate (or probability of being [OII] mentioned in §3.4) and was applied to the CDFS and FIRES fields separately. For each field, all photometric redshift probability distribution functions corresponding to galaxies within the LDSS-3 FOV (centered on the ROLES75 fields) were first binned by K-magnitude, then summed within each bin, giving the total redshift distribution for all galaxies in each bin, $P_K(z)$. The summed redshift distribution in each bin was then integrated across the redshift range targeted by ROLES75 ($0.62 < z < 0.885$). Mathematically, this was

$$N_K^{all} = \int_{0.62}^{0.885} \sum_{i=0}^{n} P_{K,i}(z) dz \tag{4.4}$$

where the set of galaxies in a K-magnitude bin were indexed from $i = 0..n$, $P_{K,i}(z)$ was a single photometric redshift PDF for a galaxy in a given K-magnitude bin, and N_K^{all} was the number of galaxies in a given K-magnitude bin within the ROLES75 redshift range. The process was then repeated for only those galaxies which ROLES75 actually targeted, giving

a similar result, $N_K^{targeted}$ (see Figure 4.1). Finally, the completeness for each K-magnitude bin was determined by taking the ratio of these arrays,

$$w_K = \frac{N_K^{targeted}}{N_K^{all}} \tag{4.5}$$

The K-magnitude dependent ROLES75 completeness is shown in Figure 4.2 with the CDFS field represented by the solid red line and the FIRES field denoted by the green dashed line.

4.2 Survey Volume

The ROLES75 survey volume was limited by the field-of-view of LDSS-3 (with the exception of the FIRES field), the imposed K-band magnitude limits ($22.5 < K < 24$), and a lower flux limit defined by the average noise of the survey masks. Therefore, the maximum volume from which a galaxy could be found within our survey was determined uniquely for each galaxy for which an emission line was found.

4.2.1 K-Band Magnitude Limits

Using a "k-correction", the K-magnitude of each galaxy was projected to each limit ($22.5 < K < 24$) and the corresponding redshift where the galaxy would have these K-magnitudes was determined. The method adopted here was the same as that used by ROLES1,

$$K_z = K_{z_{obs}} + 5 \cdot Log(d_{z_{obs}}/d_z) + (k_{corr,z} - k_{corr,z_{obs}}) \tag{4.6}$$

$$k_{corr}(z) = \frac{-2.58z + 6.67z^2 - 5.73z^3 - 0.42z^4}{1 - 2.36z + 3.82z^2 - 3.53z^3 + 3.35z^4} \tag{4.7}$$

where $d_{z_{obs}}$ and d_z were the luminosity distances corresponding to the observed and projected redshifts, $k_{corr,z_{obs}}$ and $k_{corr,z}$ were the k-corrections at the observed and projected redshifts (using Eqn. 4.7), and $K_{z_{obs}}$ and K_z were the observed and projected K-magnitudes. The observed values were fixed, while a set of test (projected) redshifts was iterated through the above equations until the projected K-magnitudes were equal to the limits of the ROLES75 survey.

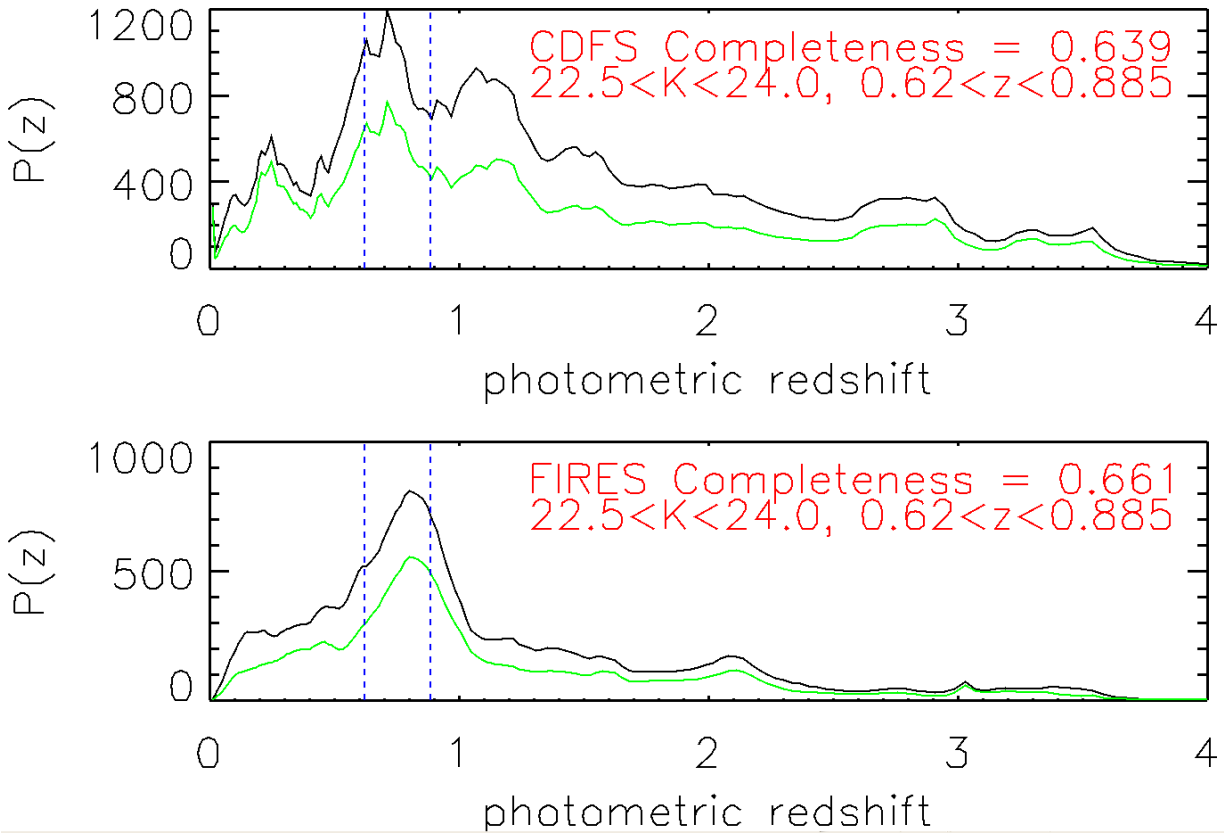

Figure 4.1: (Upper Panel) Summation of all photometric redshift PDF's within the LDSS-3 FOV and with $22.5 < K < 24$ (black curve) compared with the summation of those photometric redshift PDF's corresponding to galaxies targeted in this survey (lower green curve), for the CDFS field. (Lower Panel) Same as the upper panel, corresponding to the FIRES field.

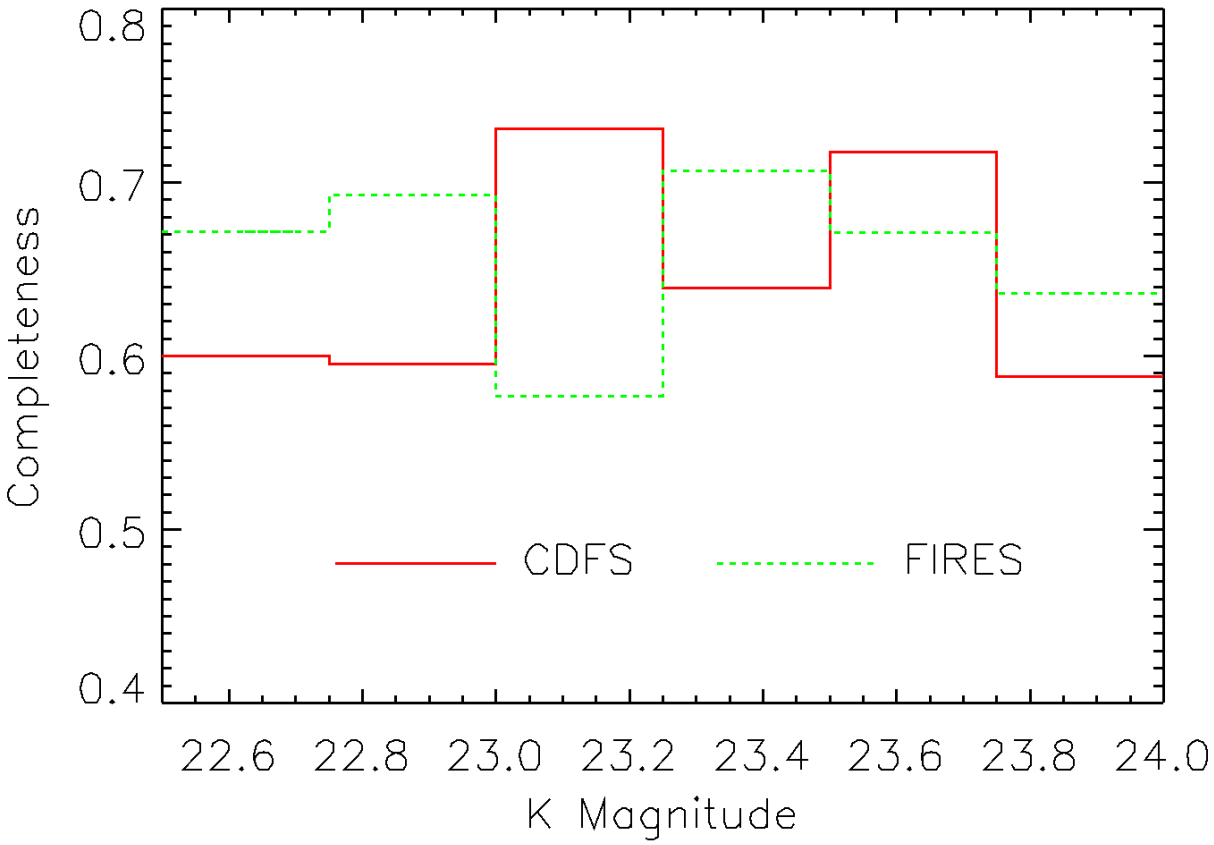

Figure 4.2: ROLES75 spectroscopic completeness for the CDFS (solid red line) and FIRES (dashed green line) fields.

4.2.2 L[OII] Flux Limit

The L[OII] flux limit was determined for each survey mask from the associated noise propagated through the analysis pipeline. Rather than using a constant flux limit, we used a flux limit defined by the dominant bright skylines found in each galaxy spectrum. For each mask the average noise spectrum was determined from all of the dispersed spectra in the mask. This average was then scaled by five which corresponded to the significance threshold selected for our 5σ catalog. The scaled average noise flux limit became the average noise flux limit for the mask and was interpreted as the flux limit below which a detection could not be considered real (see Figure 4.3). This was repeated for each mask, and finally the average of the mask noise flux limits was determined. This final average was used as the flux limit for our 5σ linelist, and any detection which had a flux below this limit was culled from the linelist, as shown in Figure 4.4.

Similar to the calculation of the projected K-magnitude redshift limits discussed in §4.2.1, a flux limit dependent distant projected redshift was determined for each galaxy with a detected emission line. The flux of each detection in our 5σ catalog was projected from its observed redshift to the distant redshift, using a similar algorithm as that in §4.2.1. The projection was accomplished using a redshift scale factor set to the ratio of the square of luminosity distances, $D_L(z_{obs})^2/D_L(z_{proj.})^2$, implying that the line flux decreased with increased projected redshift. For each iteration of the algorithm the projected flux was compared with the average $5 \cdot N_{ij}$ noise flux limit, and the redshift limit taken to be the location where they crossed.

4.3 Determination of Vmax

The volume, V_{max}, from which a galaxy with a detected emission line could have been found was defined by the survey area of each field pointing (limited by the FOV of LDSS-3) and the redshift space bounded by the imposed K-magnitude and noise flux limits. The survey areas for the ROLES75 CDFS and FIRES fields were 105.62 and 29.15 square arcminutes respectively. The redshift limits for each emission line in our 5σ catalog were taken to be

$$z_{min} = max\left\{0.62, \quad z_{local}^{K-mag}\right\}$$
$$z_{max} = min\left\{0.885, \quad z_{distant}^{K-mag}, \quad z_{distant}^{noise-flux}\right\}$$

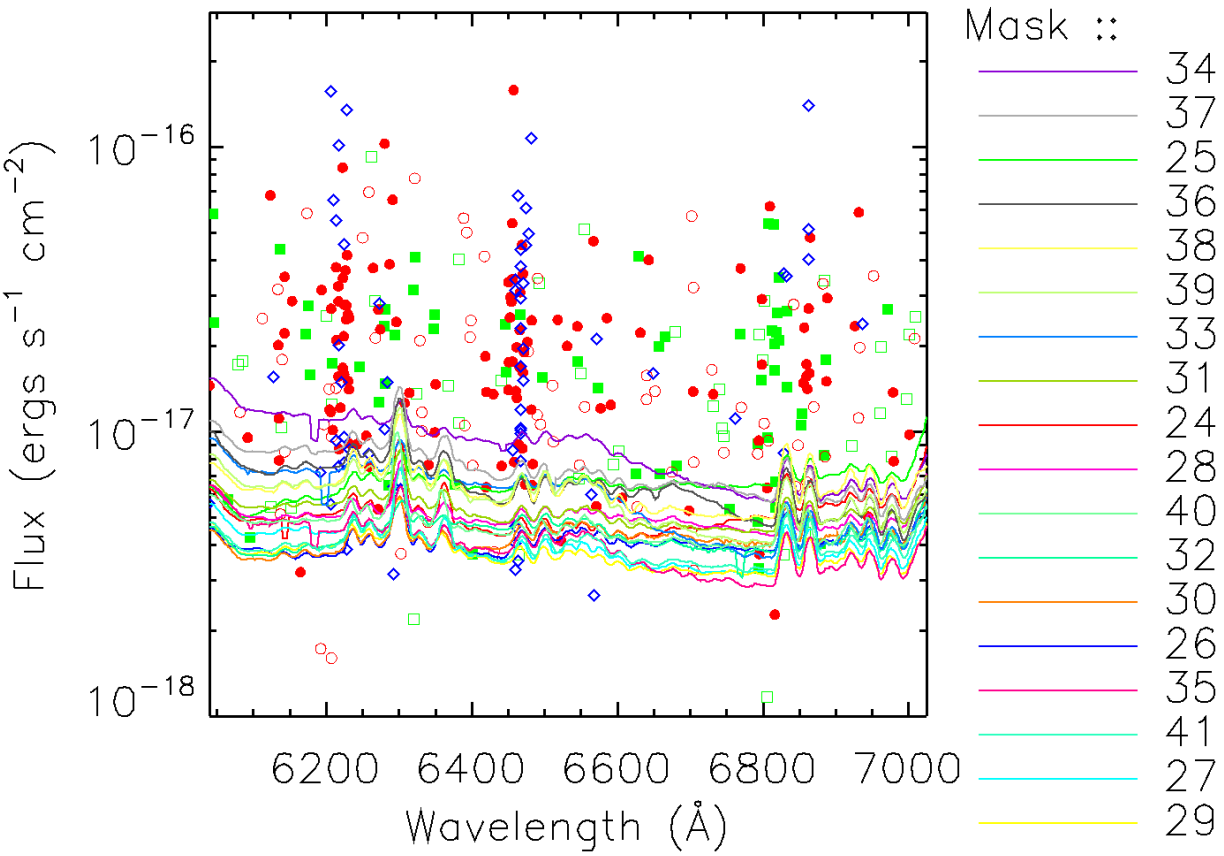

Figure 4.3: All 5σ detections plotted as line flux vs. wavelength. Detections are divided into the CDFS ROLES (red), FORS2 (blue diamonds), and FIRES (green) fields. The $5 \cdot N_{ij}$ noise flux limit determined for each mask is overplotted as a solid line. The difference between the $5 \cdot N_{ij}$ noise flux limit for the brightest mask and faintest mask is approximately a factor of four at the low wavelength end, and roughly a factor of two at the high wavelength end.

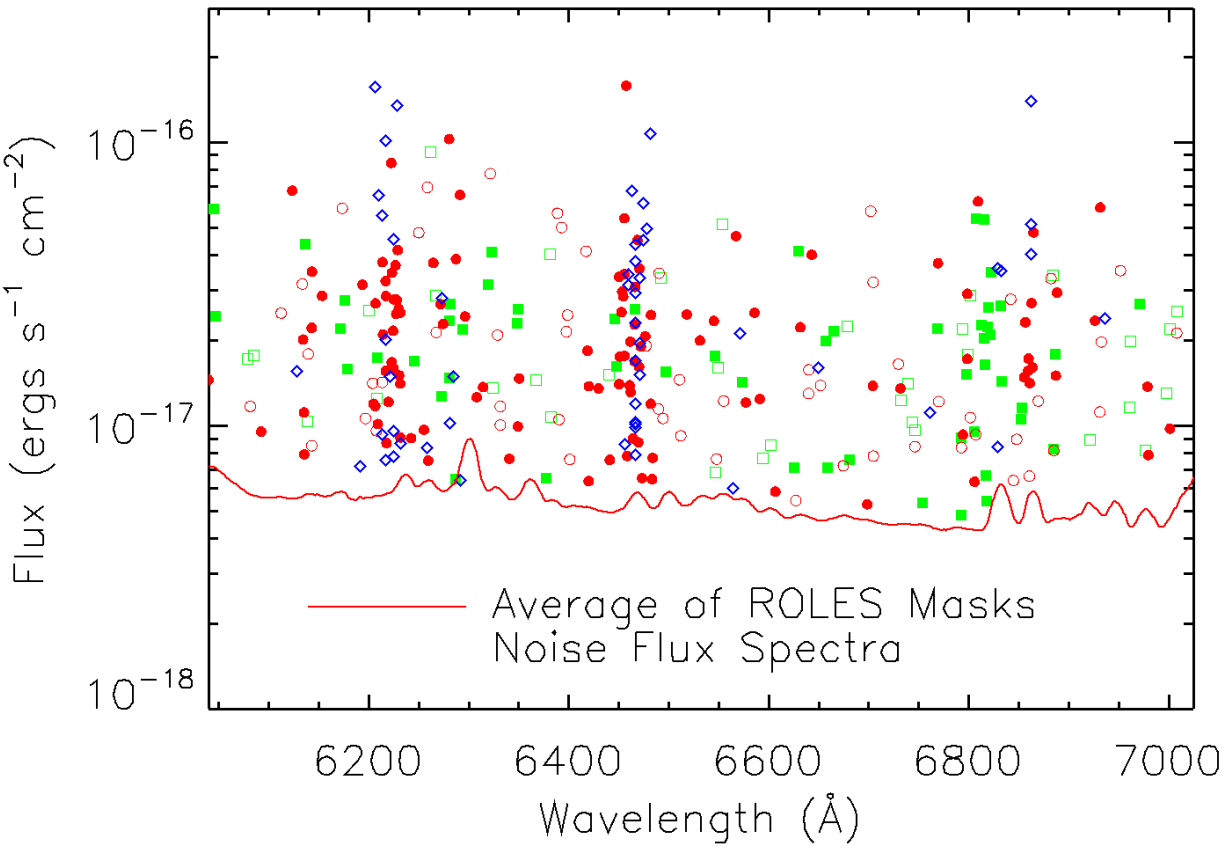

Figure 4.4: Culled 5σ detections plotted as line flux vs. wavelength. Detections are divided into the CDFS ROLES (red), FORS2 (blue diamonds), and FIRES (green) fields. The average $5 \cdot N_{ij}$ noise flux limit of all masks is overplotted as a solid line. The bright skylines are clearly evident in the flux limit curve, with the [OI] line dominating at 6300Å.

where the redshifts denoted by "K-mag" and "noise-flux" superscripts corresponded to the projected redshift limits calculated in §4.2.1 and §4.2.2. The volume, V_{max}, was determined for each galaxy using

$$V_{max} = \Omega_{field} \int_{z_{min}}^{z_{max}} \frac{dV_c}{dz} dz \tag{4.8}$$

where dV_c/dz was the differential co-moving volume (see Hogg (1999)), and Ω was the survey field area in sterradians. The typical ($0.62 < z < 0.885$) V_{max} for a ROLES75 CDFS galaxy was $4.7 \times 10^4\ Mpc^3$, and $1.3 \times 10^4\ Mpc^3$ for a FIRES galaxy.

Segregating the dataset into high density structure and low density field populations changes the maximum volume from which a galaxy can be drawn. Figure 5.1 shows the distribution of galaxy redshifts for each of ROLES75 CDFS, FIRES, and FORS2, where it is clear that a galaxy found within the CDFS structure is confined to two redshift sub-ranges, $z = 0.668 \pm 0.016$ and $z = 0.735 \pm 0.009$. Thus a ROLES75 CDFS structure galaxy could be drawn from a maximum volume of $\sim 8 \times 10^3 Mpc^3$, and a CDFS field galaxy could be found within a volume of $\sim 3.9 \times 10^4 Mpc^3$. Similarly, a FIRES cluster galaxy ($z = 0.83 \pm 0.02$) would have a maximum volume of $\sim 2.2 \times 10^3 Mpc^3$, while its field counterparts would reside in a volume of $\sim 1.1 \times 10^4 Mpc^3$.

4.4 Extension of Survey with Higher Mass Sample

As in ROLES1, this survey was extended beyond the targeted high mass limit of $Log(M_*/M_\odot) < 9.5$ by repeating the analysis using data for a subset of emission line galaxies targeted by *The GOODS Team* (Vanzella et al., 2008). This public data is VLT/FORS2 spectroscopy in the GOODS-S field (which overlaps with the ROLES75 CDFS field). Their sample was a color and photometric redshift selected catalog with targets found between the redshift ranges of $0.5 \lesssim z \lesssim 2$ and $3.5 \lesssim z \lesssim 6.3$. We selected only those targets which were found within the LDSS-3 field-of-view centered on our CDFS field pointings, and which fell within our redshift range of $0.62 < z < 0.885$. Their observation masks used 1" slits (compared to 0.8" for ROLES) and exposure times for each mask were typically ≥ 4 hours. Herein this higher mass sample is referred to as *FORS2*.

We extracted spectroscopic redshifts, line identifications and quality flags, and 1D spectra for the subset of their catalog mentioned above. Emission line fluxes, identified as being [OII], were measured from the 1D spectra in the same way as for ROLES1. A constant 4σ noise flux limit of $6 \times 10^{-18} ergs^{-1} cm^{-2}$ was used in ROLES1 and it was adopted

for the same sample here since it was approximately the same as the average noise flux limit for ROLES75 (see Figure 4.4). For each FORS2 emission line we calculated V_{max} as before (with a typical value of $4.7 \times 10^4\ Mpc^3$). Since the FORS2 sample is in the CDFS field, its high and low density galaxies use the volumes described for the ROLES75 CDFS population. The K-magnitude binned FORS2 completeness was determined in the same way as for the ROLES CDFS and FIRES completeness (recall Equations 4.4 and 4.5 in §4.1), with the FORS2 targets limited to the LDSS-3 FOV. The completeness for the ROLES75 CDFS field was then extended with the FORS2 data set as shown in Figure 4.5. Where the two sets overlapped in K-magnitude, the FORS2 success rate of measuring redshifts was taken to be 72% as was done in ROLES1.

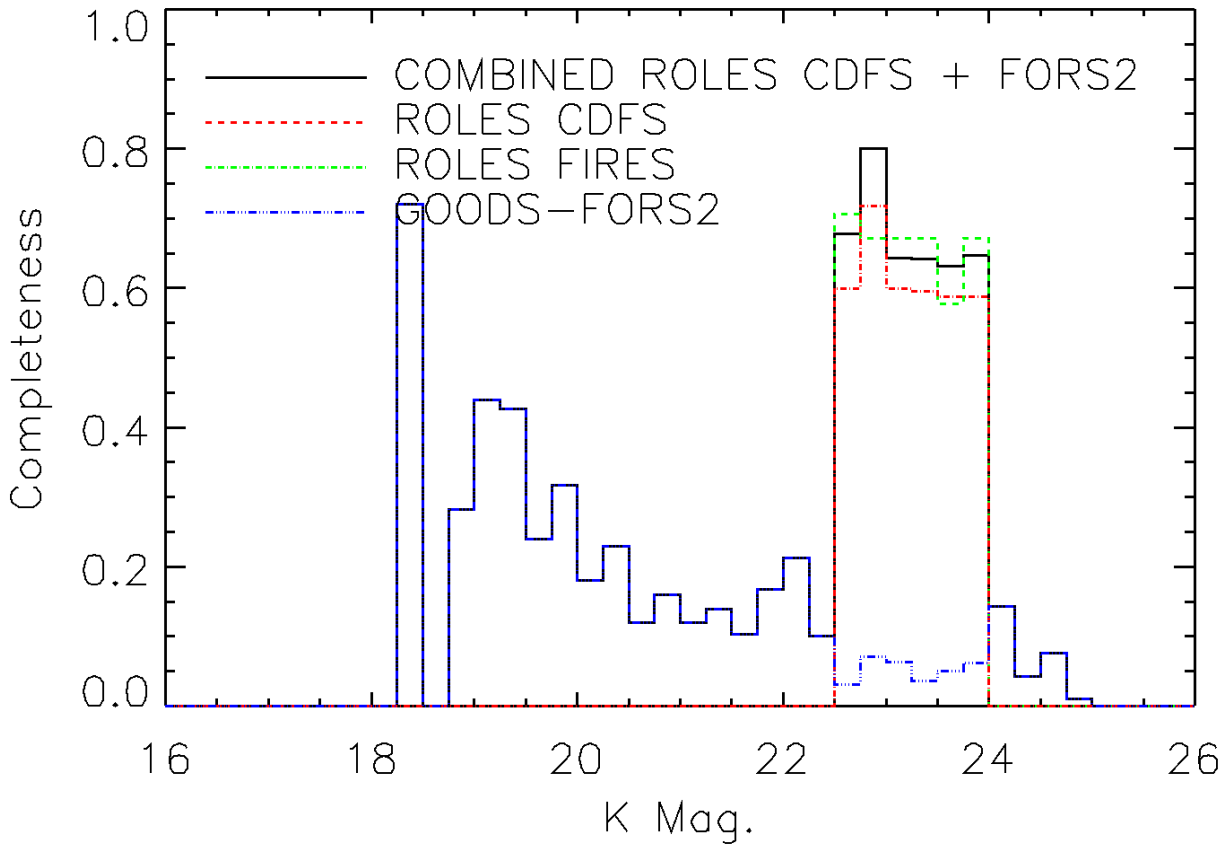

Figure 4.5: Completeness histograms for ROLES75 CDFS, FIRES, FORS2, and the combined CDFS + FORS2 data sets. The ROLES75 CDFS and FIRES completeness was limited to $22.5 < K < 24$, reflecting the survey selection used. The FORS2 data reached larger stellar masses, thus extending the completeness out to brighter K-magnitudes.

Chapter 5

Results & Discussion

The primary objective of this work was to examine how environment drove star formation in the low stellar mass regime during the $z \sim 0.75$ epoch. Many studies have examined the impact of environment on the stellar mass function (GSMF), star formation rate density (SFRD) and specific star formation rate (sSFR) at low redshift (Bolzonella et al., 2010; Peng et al., 2010; Popesso et al., 2011, to name a few). However, observations are sparse in the low mass regime at the redshift surveyed by ROLES. Following are the results of the ROLES75 survey analysis divided into cluster/structure vs. field, which demonstrate the effect of environment on star formation for low mass star-forming galaxies. Other higher mass surveys were compared with the ROLES75 results, offering a semi-complete picture of star formation across a large range of stellar mass.

For the structure/field analysis, targeted ROLES75 galaxies with detected [OII] emission lines were separated into one of three different categories: structure found in CDFS, the MS1054-03 cluster in the FIRES field, or membership of the field population. Closer examination of Figures 4.3 and 4.4 in §4.2.2 confirms a high density of CDFS galaxies with detected emission lines found at two observed wavelengths of $\lambda_{[OII]_{CDFS,S1}} \sim 6217$Å and $\lambda_{[OII]_{CDFS,S2}} \sim 6466$Å ($z_{CDFS,S1} = 0.668 \pm 0.016$ and $z_{CDFS,S2} = 0.735 \pm 0.009$, (Ravikumar et al., 2006)). The redshift ranges of these high density structures were verified by histogramming the emission line galaxy redshifts, shown in Figure 5.1. Ravikumar et al. describe these structures as 'wall-like,' or certainly not a cluster, and which have been discussed in greater detail in other literature (see Gilli et al. (2003); Le Fèvre et al. (2004); Vanzella et al. (2005)). Figures 4.3, 4.4, and 5.1 also show the MS1054-03 cluster in the FIRES field at an observed wavelength of $\lambda_{FIRES,Cluster} \sim 6820$Å ($z_{Cluster} = 0.83 \pm 0.02$, (Förster Schreiber et al., 2006)). Emission line galaxies which did not fall within any of

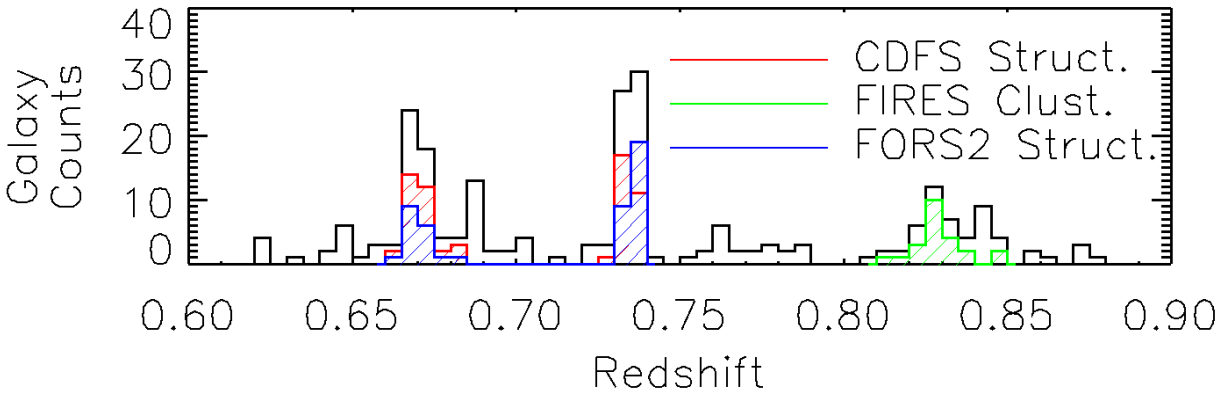

Figure 5.1: Redshift distribution of ROLES75 emission line galaxies.

the structure/cluster redshift ranges were finally classified as (low density environment) field galaxies (see the non-hatched regions of the redshift distributions in Figure 5.1).

5.1 [OII] Luminosity, Mass and SFR Limits

The four primary science results presented in the forthcoming sections rely critically upon knowing what the limits of the ROLES75 survey are, and the impact they have on the interpretation of these results. Special care must be taken to ensure that observed trends and features which may be present in the results are not based upon 'incomplete' data. Therefore, before presenting the results of the ROLES75 survey, we first provide the [OII] luminosity, mass, and star-formation rate limits of the survey.

The [OII] flux limit is shown in Figure 4.4. Its mean value is $\sim 6 \times 10^{-18} ergs\ s^{-1} cm^{-2}$, and its maximum is $\sim 8 \times 10^{-18} ergs\ s^{-1} cm^{-2}$. In an effort to be conservative, we take the maximum as the [OII] flux limit, for the purposes of interpreting later results. This is higher than the [OII] flux limit used to cull the emission line detections in §4.3, where we used the actual wavelength dependent average noise flux limit shown in Figure 4.4. To re-iterate, we are only using this higher flux limit when interpreting the results and we have chosen to be conservative with this estimate. Based upon this flux limit and the lower ROLES75 redshift of $z \sim 0.62$, the **[OII] luminosity limit is determined to be** $LogL_{[OII]} \sim 40.1$.

The mass limit is determined from the scatter of the K-magnitude vs. stellar mass plot shown in Figure 5.2. The horizontal dashed green line shows the K-magnitude limit of

$K = 24$. Based upon the typical scatter of this plot and where it crosses the K-magnitude limit, the ROLES75 mass limit is $Log(M^*/M_\odot) \sim 8.85$. The best-fit line crosses the K-magnitude limit at $Log(M^*/M_\odot) \sim 8.5$, verifying the lower mass limit originally targeted by ROLES. Clearly the ROLES75 CDFS sample is the most influenced by this mass limit, which will affect the interpretation of the primary science results. As suggested earlier, we are being conservative with these limits. As such, it is evident in Figure 5.2 that we are 100% complete for $LogM^* > 8.85$ *and* $K < 22.8$, the latter defined by where the typical bright-side scatter crosses the mass limit. Fainter than $K \sim 22.8$ and toward lower stellar mass, the survey begins to be incomplete in K-magnitude. Probing to even fainter K-magnitude and lower stellar mass, the survey is incomplete in both mass and K-magnitude when $K > 24.0$ and $Log(M^*/M_\odot) < 8.85$

Finally, using the [OII] luminosity limit, we can derive the ROLES75 star formation rate limit using Equations 4.2 and 4.3. Figure 5.3 is a plot of the empirically corrected star formation rates versus stellar mass. The mass and SFR limits are highlighted as green dashed lines. The SFR limit is curved due to the hyperbolic tangent function present in the mass dependent SFR empirical correction of Equation 4.3. The ROLES75 sample is limited to $\sim 0.1 M_\odot yr^{-1}$ while the FORS2 sample sees an increasing SFR limit with increasing stellar mass. Near the largest stellar mass of $10^{11} M_\odot$, the FOR2 sample is limited to $\sim 1 M_\odot yr^{-1}$.

The four primary science results are the [OII] luminosity function, galaxy stellar mass function, star formation rate density, and specific star formation rate. For each of these results we also show the ROLES1 and local SDSS data for comparison purposes, and highlight the incompleteness limits.

5.2 [OII] Luminosity Function

The ROLES75 number density of galaxies, Φ, was determined for bins of log [OII] luminosity ($LogL_{[OII]}$), using the $1/V_{max}$ method. For each $LogL_{[OII]}$ bin,

$$\Phi_{(LogL_{[OII]})_\ell} = \sum_{\substack{i=0 \\ \ell \ const.}}^{n} \frac{P_{OII,i}}{w_i \cdot V_{max,i}} \tag{5.1}$$

where the summation ran over the set of all detections ($i = 0..n$) found within the bin of $(Log\ L)_\ell$, $P_{OII,i}$ was the probability of the i^{th} detection being [OII], w_i was the K-magnitude dependent completeness for the detection, and $V_{max,i}$ was the corresponding

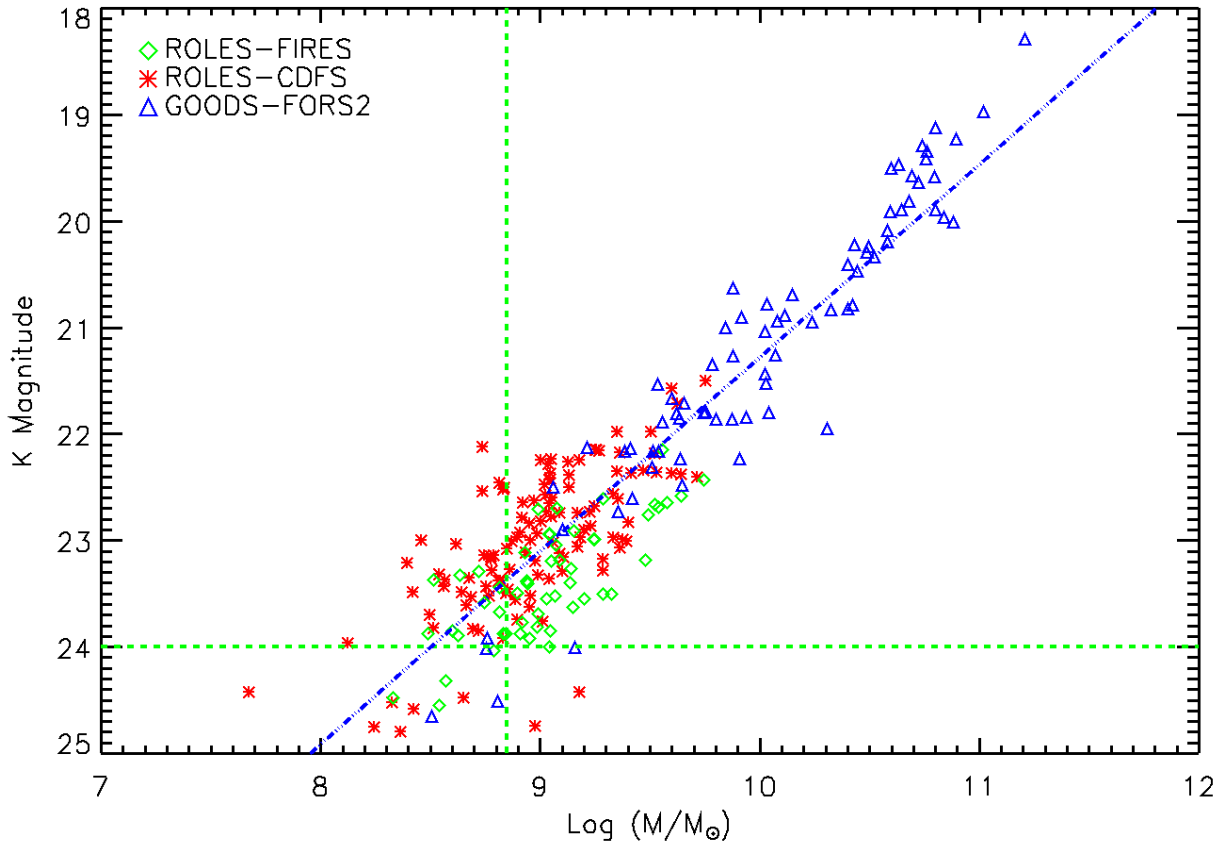

Figure 5.2: K-magnitude vs. stellar mass for the three ROLES75 populations. The ROLES75 CDFS galaxies are shown as red asterisks, FIRES as open green diamonds, and the extended higher mass sample of GOODS-FORS2 is represented by open blue triangles. Dashed green lines show the K-magnitude and stellar mass limits, while the blue '– · · · –' curve is the line of best fit to the three populations combined.

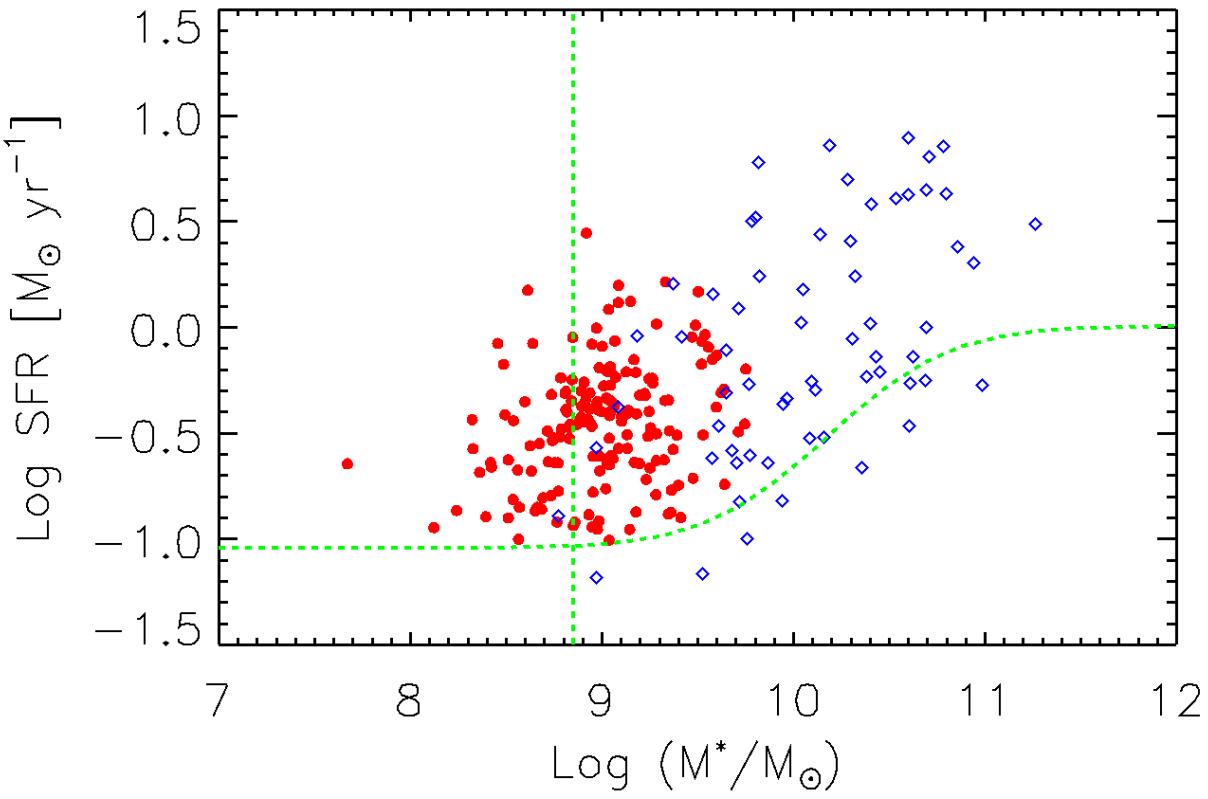

Figure 5.3: SFR of the ROLES75 and FORS2 datasets. The axes are $SFR[M_{\odot}yr^{-1}]$ vs. $Log(M_*/M_{\odot})$. ROLES75 is shown as solid red circles while FORS2 is represented by open blue squares. The ROLES75 mass and SFR limits are shown as green dashed lines.

volume from which it could have been drawn. The upper and lower limit error bars for each ($Log\ L_{[OII]}$) bin were based on Poisson counting statistics, and required a scale factor and effective number of binned objects, as described by Zhu, Moustakas & Blanton (2009). The effective weight, W_{eff}, scaled the effective number of binned objects, N_{eff}, where

$$\begin{aligned} W_{eff,\ell} &= \sum_{\substack{i=0 \\ \ell\ const.}}^{n} \left[\frac{1}{(V_{max})_i^2} \Big/ \frac{1}{V_{max,i}} \right] \\ N_{eff,\ell} &= \sum_{\substack{i=0 \\ \ell\ const.}}^{n} \left[\frac{1}{V_{max,i}} \Big/ W_{eff,\ell} \right] \end{aligned} \tag{5.2}$$

Then, each N_{eff} for a given bin was used to determine the Poisson upper and lower counting limits for the bin. This method is described in detail in Gehrels (1986), however the specific equations used have been repeated below for clarity, where

$$\begin{aligned} \Phi^{UpperLimit}_{(LogL_{[OII]})_\ell} &= W_{eff,\ell} \cdot \left[(N_{eff,\ell}+1) \cdot \left(1 - \frac{1}{9 \cdot (N_{eff,\ell}+1)} \right.\right. \\ &\quad \left.\left. + \frac{1}{3 \cdot \sqrt{N_{eff,\ell}+1}} \right)^3 \right] \\ \Phi^{LowerLimit}_{(LogL_{[OII]})_\ell} &= W_{eff,\ell} \cdot \left[N_{eff,\ell} \cdot \left(1 - \frac{1}{9 \cdot N_{eff,\ell}} \right.\right. \\ &\quad \left.\left. - \frac{1}{3 \cdot \sqrt{N_{eff,\ell}}} \right)^3 \right] \end{aligned} \tag{5.3}$$

The [OII] luminosity function for ROLES75 is shown in Figures 5.4 and 5.5. Figure 5.5 shows the data set divided into high density (combined CDFS ROLES + FORS2 structures) and low density (CDFS ROLES + FORS2 field) environments. In Figure 5.4 the combined CDFS ROLES75 [1] and FORS2 subsample, and the combined CDFS ROLES1 and FORS2 datasets are shown. Note that we intentionally omit the FIRES sample since

[1]Herein, *combined* refers to the use of the K-magnitude dependent completeness function shown in Figure 4.5 when joining the ROLES75 CDFS sample with the higher mass GOODS-FORS2 dataset. This is done in each of the major science result sections ([OII] LF, SF-GSMF, SFRD, and sSFR).

it has not been extended with a higher mass galaxy dataset as we were able to do with the CDFS subset. Data from Zhu, Moustakas & Blanton (2009) in the redshift range of $0.75 < z < 0.93$ has been overplotted in Figure 5.4 for comparison purposes.

Zhu, Moustakas & Blanton used [OII] measurements from the DEEP2 (Deep Extragalactic Evolutionary Probe, DEIMOS instrument) Data Release 3, which was an R-band and color selected survey (Davis, 2003). Masks used 1" wide slits with exposure times between one and three hours, which was comparable to 0.8" and $\sim$ 2 hours for ROLES. It should be noted that the DEEP2 survey spectra were not flux calibrated and thus the method used to determine [OII] line luminosities was different than that used by ROLES. Zhu, Moustakas & Blanton multiplied rest-frame equivalent widths of [OII] emission lines by the continuum luminosity in the region of 3727Å, determined from SED-fitted BRI photometry.

A local ($z \sim 0.1$) SDSS $L_{[OII]}$ comparison sample is also shown in Figure 5.4. This data was extracted from Gilbank et al. (2010b) and corresponds to the mass selected ($8.5 < Log(M^*/M_\odot) < 9.5$) population in the right panel of Figure 14 of that work.

It is clear that ROLES has probed the faint luminosity side of the [OII] luminosity function for this epoch, where there is a noticeable offset of $LogL_{[OII]} \sim 0.7$ between the bright-end of the ROLES data and the bright-end fit[2] of the Zhu, Moustakas & Blanton data. This offset is most likely due to lower than expected measured [OII] line fluxes for the higher stellar mass population of the extended FORS2 sample. Figure 5.3 shows nine FORS2 targets falling below our conservative SFR limit, or $\sim$ 14% of the FORS2 population. A unform shift of 0.2 dex toward higher SFRs for the FORS2 population would ensure that all FORS2 targets would be above the conservative SFR limit. This shift would also correspond to a shift of 0.2 dex toward higher [OII] luminosity for the FORS2 sample, reducing but not completely eliminating the offset of 0.7 dex between the ROLES75 bright-end and that of Zhu, Moustakas & Blanton. The completeness or V_{max} corrections of the FORS2 sample may have been overestimated in the bright [OII] luminosity end, which would shift the number density of FORS2 galaxies downward, thus increasing the offset between the ROLES75 and Zhu, Moustakas & Blanton samples. All of the higher redshift populations have bright-end slopes which are shifted to larger [OII] luminosities by a factor of approximately ten, in comparison to the location of the local SDSS [OII] LF bright-end slope. This suggests that the [OII] luminosity of galaxies was higher in the past than it is at present day.

In the faint-end, all of the populations exhibit a 'turnover' with the exception of the

[2]The functional form of the Zhu, Moustakas & Blanton power law fit is: $\Phi(LogL)\ d(LogL) = 10^{(\alpha+1)(LogL-42.5)+\beta}\ d(LogL)$.

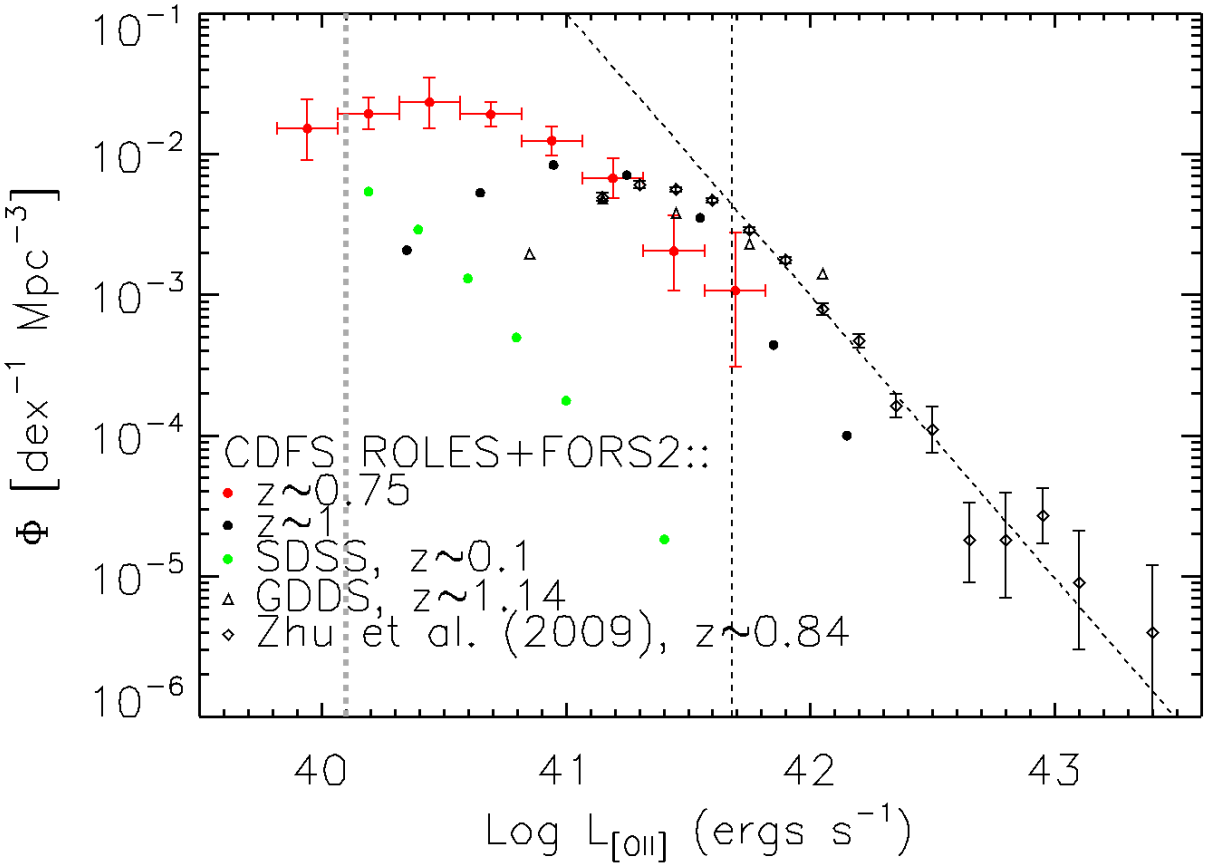

Figure 5.4: [OII] Luminosity function of the ROLES75 data set. The axes are Φ[dex^{-1}Mpc^{-3}] vs. Log $L_{[OII]}$[erg s^{-1}]. ROLES1 data consisting of combined CDFS ROLES1 and FORS2, and GDDS is shown as black solid circles and open triangles respectively, without error bars (for clarity). ROLES75 data consisting of combined CDFS and FORS2 (solid red circles) is shown with error bars. Local SDSS LF data extracted from Gilbank et al. (2010b) is represented by solid green circles. The ($0.75 < z < 0.93$) data from Zhu, Moustakas & Blanton (2009) is shown as black diamonds with error bars for comparison purposes. Also shown is their bright-end LF fit (angled thick black dashed line) and highlighted LF "turnover" point (thin black dashed vertical line). The thick grey vertical dashed line highlights the faint [OII] luminosity limit of this survey.

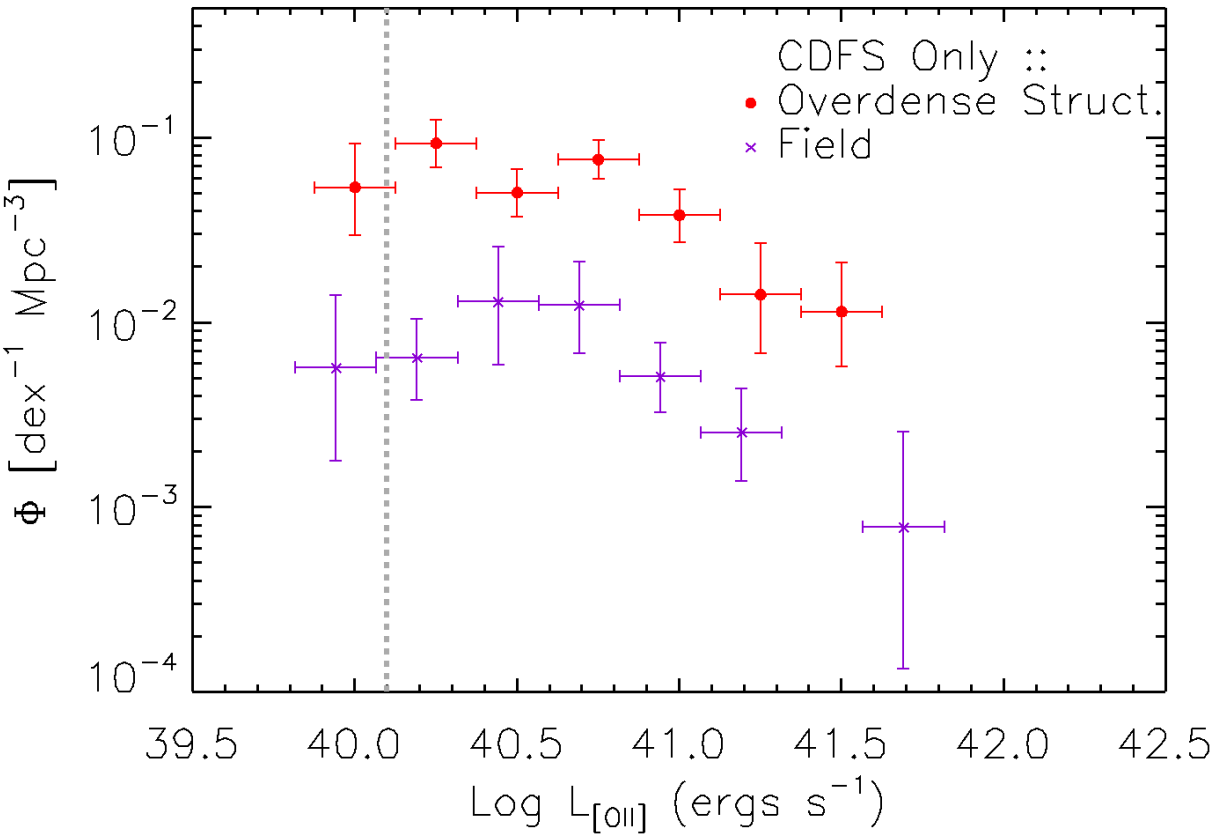

Figure 5.5: [OII] Luminosity function of the ROLES75 data set. The axes are Φ[dex^{-1}Mpc^{-3}] vs. Log $L_{[OII]}$[erg s^{-1}]. The data set has been divided into high density [ROLES75 + FORS2 CDFS Structure (solid red circles)], and low density [ROLES75 + FORS2 CDFS field (purple X)] environments. The thick grey vertical dashed line highlights the faint [OII] luminosity limit of this survey.

local SDSS [OII] LF which does not extend to faint enough [OII] luminosites where we might see a turnover. The ROLES75 [OII] LF turnover is located 0.5 dex brighter in luminosity than our [OII] luminosity limit at $LogL_{[OII]} = 40.1$, suggesting that this effect is not a result of incompleteness. The ROLES1 turnover *due to incompleteness* occurs at $LogL_{[OII]} = 40.5$ (Gilbank et al., 2010b), which is ~ 0.8 *dex* fainter than the turnover effect due to the nature of the [OII] LF at $z \sim 1$. Hence both ROLES [OII] LF results suggest the presence of a turnover in their respective faint-ends for $z \gtrsim 0.6$. The GDDS sample at $z \sim 1.14$ is a higher mass sample which also appears to show a turnover in its [OII] LF. Interestingly, the GDDS sample traces the Zhu, Moustakas & Blanton [OII] LF remarkably well suggesting there may be a mass selection effect between the ROLES and Zhu, Moustakas & Blanton samples.

As expected, the normalizations of each population shown in Figure 5.5 are different, with there being a larger number density of galaxies in the high density environment as compared to the low density field subset. Also, comparing between Figures 5.4 and 5.5, the [OII] *structure* LF lies *above* the *combined* CDFS LF, while the *field* [OII] LF lies below it. Note that it is not the normalization which may suggest a difference in the formation of galaxies in different density environments, but rather the *shape* of the respective [OII] luminosity functions. The CDFS structure and field [OII] luminosity functions have comparable bright end slopes. However, considering the location of our conservative [OII] luminosity limit, the low density field population exhibits the turnover discussed earlier while the high density structure population does not (we are ignoring the impact of the faintest [OII] luminosity bin in each population since it falls behind the [OII] luminosity limit). This suggests that the faint-end slope of the high density environment [OII] LF remains shallow at low luminosities while the field population turns over. The difference in the faint-end between the high and low density environments is likely due to the presence of large scale structure in the CDFS field, increasing the number density of faint (low mass) galaxies which are gravitationally bound to this structure. Thus the comparable shapes of the [OII] LF for each population suggests that at $z \sim 0.75$, the [OII] luminosity of star forming galaxies does not critically depend on the local density of the environment in which the galaxies are forming.

The bright end slope of the ROLES75 [OII] LF appears to extend the bright end slope of the ROLES1 population to fainter [OII] luminosities. Extrapolating to fainter luminosities, the peak of the ROLES75 [OII] LF is approximately three times larger in normalization than the ROLES1 sample. Considering that large scale structure was not present in the ROLES1 sample, it is reasonable to compare the field population of ROLES75 to the ROLES1 data, which is shown in Figure 5.6. The ROLES75 field sample reaches a peak number density of $Log\ \Phi \sim -1.82$ while that of the ROLES1 is $Log\ \Phi \sim -2.07$.

Since ROLES75 and ROLES1 both targeted the same stellar mass range, this difference in normalization of 0.25 dex is not likely a mass effect, nor is it related to the structure in CDFS as it has been removed. Thus ROLES75 suggests that the [OII] luminosity field population may be underdense. The bright-end slope of the field population appears to be more shallow than that of the ROLES1 population, suggesting the possibility of evolution in the shape of the [OII] luminosity function between these two epochs. However the error on the brightest ROLES75 [OII] LF field bin is large enough that the bright-end slopes may actually be consistent between the two epochs. Thus, this comparison suggests that the ROLES75 and ROLES1 samples are consistent at this epoch.

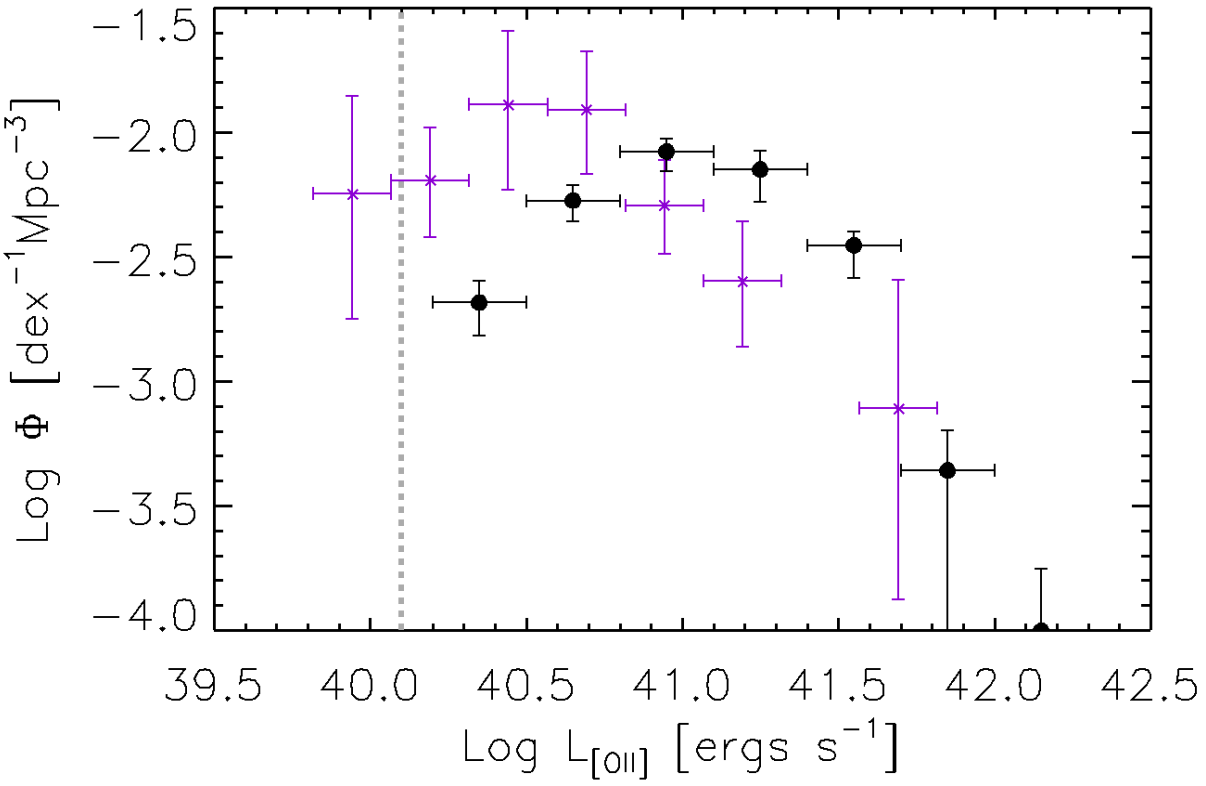

Figure 5.6: The [OII] Luminosity function of the ROLES75 field dataset (purple X's) compared with the ROLES1 LF (solid black circles). The axes are Φ[dex^{-1}Mpc^{-3}] vs. Log L$_{[OII]}$[erg s^{-1}].

5.2.1 [OII] Luminosity Function: Summary of Section

The key results of the [OII] luminosity function section are:

1. The [OII] luminosity of galaxies was higher in the past than at present day.
2. The high redshift populations exhibit turnovers in their [OII] luminosity functions which is not present in the local SDSS [OII] LF.
3. The faint-end slope of the [OII] luminosity function increases in steepness with increasing redshift.
4. Environment does not influence the [OII] luminosity function at $z \sim 0.75$.

5.3 Mass Function

The stellar mass function (SF-GSMF) was computed in a similar manner as the luminosity function (see Equation 5.1) except that the binning was according to $LogM_*$ (equal mass bins of width $\Delta LogM_* = 0.25$) rather than $LogL_{[OII]}$. The ROLES75 mass function is shown in Figures 5.7 and 5.7 where the sample has been separated in the same manner as was done for the luminosity function, with the exception that the FIRES sample has also been combined with the CDFS and FORS2 datasets. Comparison data (see Table 5.1 for the symbol legend) from ROLES $z \sim 1$ (Gilbank et al., 2011), Pozzetti et al. (2009), Sánchez et al. (2011), Drory et al. (2009), and Peng et al. (2010) are shown (without error bars for the reason that we wish to clearly highlight the evolution of the SF-GSMF with redshift) in Figure 5.7, and it is clear that the ROLES75 SF-GSMF fills in the low mass end where the comparison datasets are incomplete.

The mass function datasets from Pozzetti et al. (2009) and Sánchez et al. (2011) provided excellent comparisons with the mass function results of ROLES75 across a range of redshifts and galaxy stellar masses in Figure 5.7. Pozzetti et al. used a subset of the zCOSMOS spectroscopic survey (Lilly et al., 2007) which acquired redshifts for more than 10,000 galaxies of the *bright* ($15 < I < 22.5$) sample of the COSMOS field (also known as the zCOSMOS-bright 10k sample). Further selection cuts were made based upon emission line redshift quality flags, availability of multi-band photometry, and agreement between spectroscopic and photometric redshifts. Stellar masses were computed using the *Hyperzmass* code (Pozzetti et al., 2007) which is a modified version of the *Hyperz* code by Bolzonella, Miralles & Pelló (2000). This code used a standard photometric SED-fitting algorithm

Table 5.1: Symbol legend for the SF-GSMF comparison data of Figure 5.7.

Source	Redshift Range	Symbol
Gilbank et al. (2011)	$0.88 < z < 1.15$	blue asterisks
Pozzetti et al. (2009)	$0.55 < z < 0.75$	black X's
Pozzetti et al. (2009)	$0.75 < z < 1.0$	red X's
Sánchez et al. (2011)	$1.4 < z < 1.6$	black triangles
Sánchez et al. (2011)	$1.6 < z < 2.0$	red triangles
Sánchez et al. (2011)	$2.0 < z < 2.5$	green triangles
Sánchez et al. (2011)	$2.5 < z < 3.0$	blue triangles
Drory et al. (2009)	$0.6 < z < 0.8$	black diamonds
Drory et al. (2009)	$0.8 < z < 1.0$	red diamonds
Peng et al. (2010)	$0.02 < z < 0.085$	black squares

with solar metallicity, a Calzetti extinction law (Calzetti et al., 2000), Bruzual & Charlot population synthesis models (Bruzual & Charlot, 2003), and a Chabrier IMF (Chabrier, 2003, $0.1 - 100 M_{\odot}$). While other redshift ranges were available from Pozzetti et al., only those matching closely with ROLES were included.

Sánchez et al. also derived their multi-wavelength sample from the COSMOS field, using an IRAC $3.6 \mu m$ selection and $z \geq 1.4$ for their specific investigation into the high-redshift evolution of the galaxy stellar mass function (SF-GSMF). Their group used the *Le Phare* code (Arnouts et al., 1999; Ilbert et al., 2006) to obtain photometric redshifts and galaxy stellar masses. This photometric SED-fitting code used population synthesis models from Maraston (2005), a solar metallicity, Chabrier IMF, and Calzetti dust extinction. In addition to matching Sánchez et al. SF-GSMF redshift ranges to the ROLES75 redshift range, we have also included their SF-GSMF data extended out to $z = 3$ in an effort to demonstrate the redshift evolution of the SF-GSMF.

Both of the comparison datasets from Pozzetti et al. and Sánchez et al. used a Chabrier IMF which had to be converted to the Baldry & Glazebrook (2003) (BG03) IMF used in the ROLES analysis. This was done through the intermediary Salpeter IMF (Salpeter, 1955) where

$$\begin{aligned} M_{*,Salpeter} &= (1.65) \cdot M_{*,Chabrier} \\ Log\ (M_{*,BG03}) &= Log\ (M_{*,Salpeter}) + 0.11 \\ M_{*,BG03} &= (2.12) \cdot M_{*,Chabrier} \end{aligned} \tag{5.4}$$

$$\begin{aligned} SFR_{Salpeter} &= 1.65 \times SFR_{Chabrier} \\ LogSFR_{BG03} &= LogSFR_{Salpeter} - 0.26 \\ SFR_{BG03} &= 0.91 \times SFR_{Chabrier} \end{aligned} \tag{5.5}$$

The explanation behind the conversion factor from a Chabrier to Salpeter IMF is discussed in detail in the thesis of Marcel Haas (2010, Ch.2, pgs.25-26), and the conversion from a Salpeter to BG03 IMF is listed in Gilbank et al. (2011, Table A1).

The SF-GSMF for active galaxies from Drory et al. (2009) for the redshift ranges of $0.6 < z < 0.8$ and $0.8 < z < 1.0$ were derived from a magnitude selected subsample of the COSMOS catalog (Ilbert et al., 2009) with $i^+_{AB} < 25$ and $K_s < 24$, similar to this work. SED fitting employing a Chabrier IMF (0.1-100$M_\odot$), combined with the 2007 updated version of the stellar population synthesis models of Coelho et al. (2007), and a Calzetti et al. (2000) extinction law were all used with photometric redshifts to derive stellar masses.

The local ($z < 0.085$) SF-GSMF data was taken from Peng et al. (2010) which was their local SDSS DR7 $10 < r < 18$ selected sample. This catalog consisted of roughly 239,000 objects with reliable spectroscopy in the range of $0.02 < z < 0.085$. Their stellar masses were computed using the *k-correction* code of Blanton & Roweis (2007) which used BC03 (Bruzual & Charlot, 2003) stellar population synthesis models and a Chabrier IMF. For comparison with ROLES75, only their star-forming sample (Peng et al., 2010, eg. *Blue-All*, Figure 12) was used. The Peng et al. single Schechter function fit[3] ($\alpha_s = -1.40$, $Log(M^*/M_\odot) = 10.92$, $\Phi^* = 2.612 \times 10^{-3} dex^{-1} Mpc^{-3}$), is overplotted as the curved [$-\cdots-$] line in Figures 5.7 and 5.8.

Like the Pozzetti et al. (2009) and Sánchez et al. (2011) comparison samples, the Drory et al. (2009) and Peng et al. (2010) datasets also had to be converted from Chabrier IMF's to BG03 using Equation 5.4.

In Figure 5.7 the *mass complete* Pozzetti et al., Sánchez et al., Drory et al., and ROLES75 galaxy stellar mass functions indicate that the number density of high mass galaxies ($11 < Log(M^*/M_\odot) < 12$) has evolved very little since $z \sim 2.75$. Remarkably both the ROLES75 and ROLES1 SF-GSMF results are consistent with the observation that there is little evolution of the SF-GSMF with redshift across a stellar mass range of

[3]Note that since the Peng et al. dataset was modified to account for a BG03 IMF rather than a Chabrier IMF, their single Schechter function fit parameters for the star-forming galaxy population were modified to match the new dataset. In this case, $LogM^*$ and Φ^* were changed from the original published values of 10.67 and $1.014 \times 10^{-3} Mpc^{-3}$ respectively.

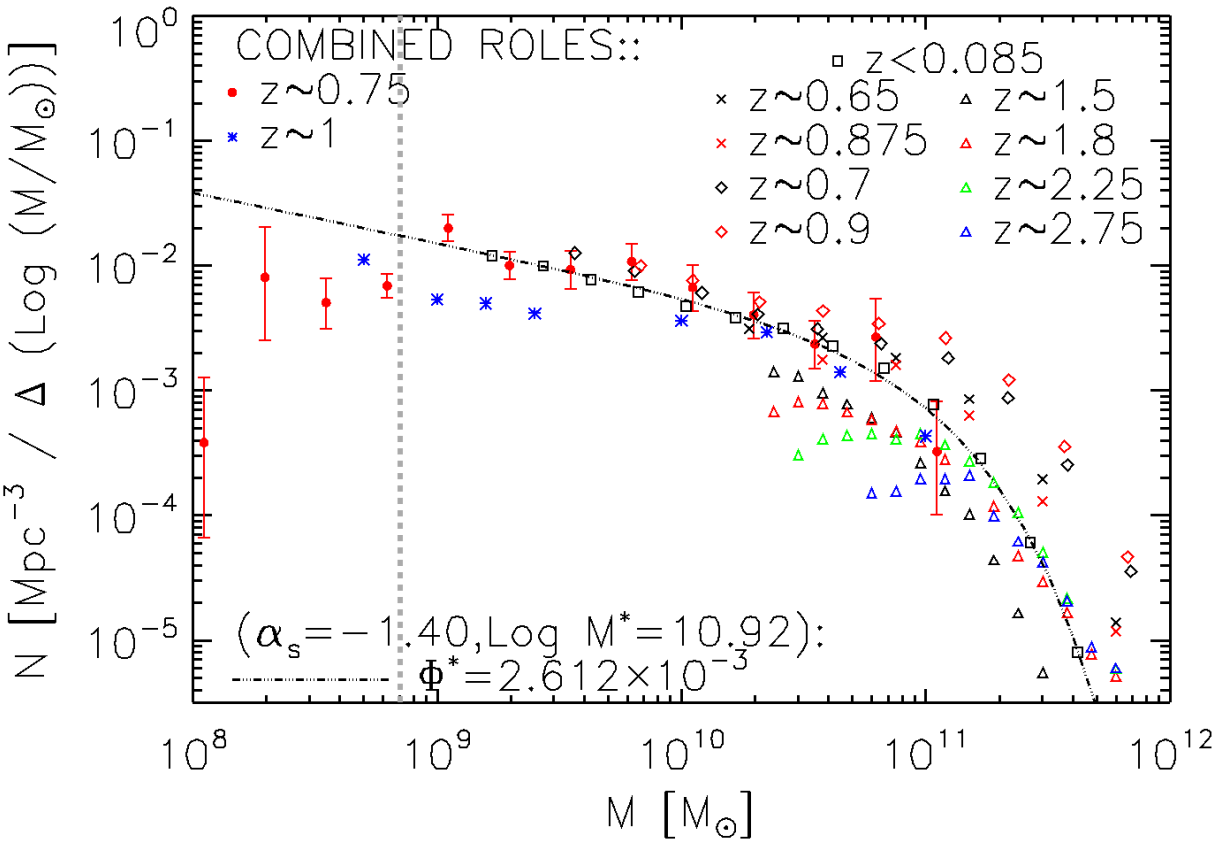

Figure 5.7: Mass function of the ROLES75 data set. The axes are $N[\mathrm{Mpc}^{-3}/\Delta(Log(M_*/M_\odot))]$ vs. $M_*[M_\odot]$. ROLES75 data consisting of combined CDFS, FIRES, and FORS2 (solid red circles) is shown with error bars. Data consisting of combined CDFS ROLES1 and FORS2 (shown as blue asterisks) is shown without error bars. The ($0.55 < z < 0.75$, $0.75 < z < 1.0$) data from Pozzetti et al. (2009) (shown as black and red X's respectively), ($0.6 < z < 0.8$, $0.8 < z < 1.0$) data from Drory et al. (2009) (shown as black and red diamonds respectively), and ($1.4 < z < 1.6$, $1.6 < z < 2.0$, $2.0 < z < 2.5$, $2.5 < z < 3.0$) data from Sánchez et al. (2011) (shown as black, red, green, and blue triangles respectively) is shown without error bars for comparison purposes. The local SF-GSMF sample from Peng et al. (2010) is shown (open black squares) with their single Schechter function fit overplotted (black dashed curve,Φ^* re-normalized to match the SF-GSMF in units of $dex^{-1}Mpc^{-3}$). The thick grey vertical dashed line highlights the mass limit of this survey.

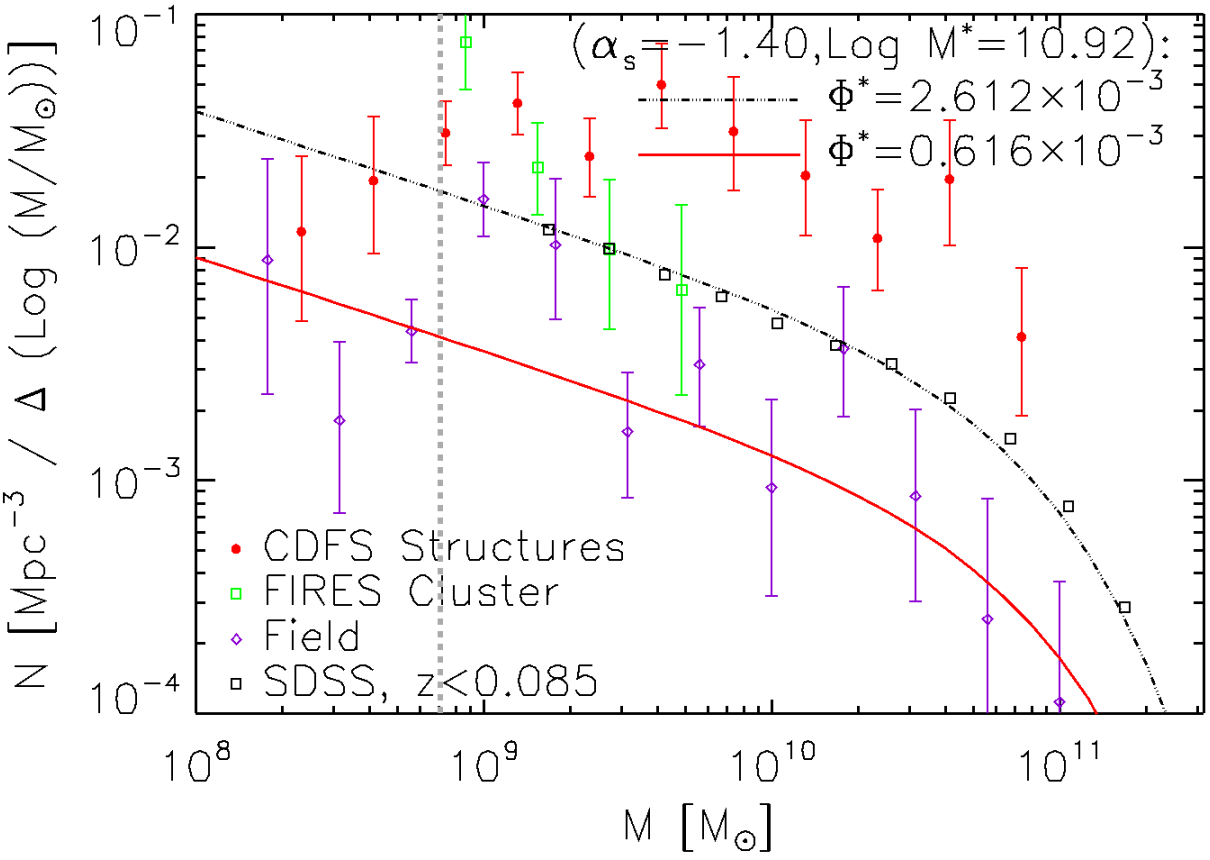

Figure 5.8: Mass function of the ROLES75 data set. The axes are $N[\mathrm{Mpc}^{-3}/\Delta(Log(M_*/M_\odot))]$ vs. $M_*[M_\odot]$. The data set has been divided into high density [ROLES75 + FORS2 CDFS Structure (solid red circles), FIRES Cluster (open green squares)], and low density [ROLES75 + FORS2 field (purple X)] environments. The local SF-GSMF sample from Peng et al. (2010) is shown (open black squares) with their single Schechter function fit overplotted (black dashed curve,Φ^* re-normalized to match the SF-GSMF in units of $dex^{-1}Mpc^{-3}$). Also a Schechter function has been fit to the ROLES75 field population using the Peng et al. (2010) α_s and M^* values, with Φ^* being the fitted free parameter (solid red curve). The thick grey vertical dashed line highlights the mass limit of this survey.

$10^{8.7} < M^* < 10^{12} M_\odot$ for star forming galaxies. This is highlighted by the fact that the ROLES75 SF-GSMF traces the local SDSS mass function within the limits of the ROLES75 errors, with the exception of the 'bump' in the high mass end. However by comparing the ROLES75 combined mass function with the dataset divided into high and low density environments in Figure 5.8, it is clear that in the high mass end, the mass function is dominated by the structure in CDFS. This is sensible as we should expect higher stellar mass galaxies to group, thus increasing their number density in a given volume. The ROLES75 field population does not exhibit this 'bump' and the shape of the field SF-GSMF is the same as the local SDSS SF-GSMF for $M^* > 10^{9.5} M_\odot$. Evidence of this is also shown by the single Schechter function fit of Peng et al., which has been renormalized to fit the ROLES75 field population (α_s and M^* held constant with Φ^* the fitted parameter; red curve). In Figure 5.8 we do not consider the difference in *normalization* between the ROLES75 field and structure populations, and the local SDSS SF-GSMF as evidence for evolution in the star forming GSMF.

The SF-GSMF for the field population is the same shape as the structure population in Figure 5.8, with the exception of the 'bump', in the high mass end at $M^* \sim 10^{10.78} M_\odot$. If the 'bump', attributed to the large number of galaxies in the 'wall' structure in CDFS, was removed, the two samples would have similar curves, with each population falling off at equal rates in the high mass end. This is sensible as higher mass galaxies are typically found in high density environments.

Interestingly, there is a distinct 'upturn' in the ROLES75 star forming GSMF in the range of $8.85 < Log(M/M_\odot) < 9.3$. This upturn is also present in the ROLES75 *field* population. In comparison, the SF-GSMF of Peng et al. (2010) does not show evidence for such an upturn. Also, the ROLES75 CDFS structure population does not exhibit this feature if we exclude the two lowest mass bins where ROLES75 is incomplete ($Log(M/M_\odot) < 8.85$). The later work of Peng et al. (2011) confirmed this upturn was present only in the passive red galaxy population of satellite galaxies, and not attributable to the passive red central galaxies, nor the star-forming galaxies. In contrast, Drory et al. (2009, i.e. Fig.5) suggested the presence of this upturn for stellar masses below a dip in the star-forming GSMF at $LogM^* \sim 10$ for redshifts $z < 1$ [4]. They suggested that a single Schechter function is not adequate to fit the star-forming GSMF and a two component, bright & faint double Schechter function should be used. This may be the case for the ROLES75 sample as well since the field population (and consequently the combined star forming GSMF) exhibits the upturn at lower stellar masses, but the high density sample does not. Drory et al. concluded that since this 'bimodal' characteristic is present in the blue star-forming pop-

[4]The dip is actually shifted to $LogM^* \sim 10.3$ because of the conversion from a Chabrier to BG03 IMF.

ulation as early as $z \sim 1$, then it is not entirely attributable to the passive red galaxy population.

While Peng et al. (2011) claim that at local redshifts the bimodal GSMF is due to the passive red satellite galaxy population, Drory et al. (2009) claim that at $z \lesssim 1$ this can not be the full picture as the blue star-forming population also shows the bimodal nature of the GSMF. To add to this, the results of this work confirm the results of Drory et al. (2009) down to a redshift of $z \gtrsim 0.62$. Drory et al. suggest that the star formation efficiency may decline at galaxy stellar masses near the dip in the GSMF, perhaps due to an increase in gas fraction, thus shifting the number density of galaxies forming near the GSMF dip to lower stellar masses. This would create the dip in the GSMF as well as the upturn. There may be a suggestion of a slight dip or plateau in the ROLES1 SF-GSMF in the range of $10^{9.3} < M^* < 10^{10} M_\odot$, while there is also a faint dip in the ROLES75 SF-GSMF in the range of $10^{9.3} < M^* < 10^{9.78} M_\odot$, each occurring before an upturn for $M^* < 10^9 M_\odot$ and $M^* < 10^{9.3} M_\odot$ for ROLES1 and ROLES75 respectively. Drory et al. (2009) also suggested another picture which coincides with the later conclusions of Peng et al. (2011) for the local SDSS SF-GSMF sample. Each component of the bimodal Schechter GSMF could consist of a bright central galaxy population dominant for stellar masses of $10^{10-11} M_\odot$ ($\alpha_{cen.}$,$M^*_{cen.}$,$\Phi^*_{cen.}$), and a faint satellite population at lower stellar masses of $M < 10^{10} M_\odot$ ($\alpha_{sat.}$,$M^*_{sat.}$,$\Phi^*_{sat.}$). The two components would minimally overlap at the observed GSMF 'dip.' The bimodal nature of the GSMF would be the result of an increase in the galaxy assembly rate for $M \lesssim 10^{11} M_\odot$. This may explain what we are seeing in the ROLES75 environment segregation of Figure 5.8.

In summary of this section, the ROLES75 and ROLES1 data suggests that there is no evidence of evolution of the GSMF for star forming galaxies since $z \sim 1$ (Figure 5.7). The presence of an increased number density at $M^* \sim 10^{10.78} M_\odot$ in the ROLES75 SF-GSMF is due to the large scale structure in the CDFS field rather than an indication of evolution which has not been seen by any other survey. The observed upturn in the low stellar mass end is consistent with the idea of a bimodal Schechter GSMF constructed from a bright central galaxy component at high stellar masses and a faint satellite population at low stellar masses.

5.3.1 Galaxy Stellar Mass Function: Summary of Section

The key results of the SF-GSMF section are:

1. The galaxy stellar mass function of [OII] luminous galaxies shows little, if any evolution since z=2.75 for stellar masses of $M^* > 10^{9.3} M_\odot$.

2. There is a tantalizingly weak suggestion of an environmental dependent upturn in the field population near $M^* \sim 10^9 M_\odot$ which is not strongly apparent in the structure population. This may be weak evidence of a bi-modal SF-GSMF in the CDFS sample.

3. The FIRES cluster SF-GSMF also shows an upturn which would argue against SF-GSMF bi-modality.

5.4 SFRD

The binned star formation rate density (SFRD) as a function of stellar mass was computed in a similar manner as the luminosity function. However, rather than binning by luminosity, bins of stellar mass were used, and the star formation rate was included in the binning process. The SFRD was computed as follows:

$$\rho_{SFR_\ell} = \sum_{\substack{i=0 \\ \ell \ const.}}^{n} \frac{P_{OII,i} \cdot SFR_i}{w_i \cdot V_{max,i}} \tag{5.6}$$

where the SFR was calculated according to Equations 4.2 and 4.3, and ℓ corresponded to a bin of stellar mass, $LogM_*$.

Figure 5.9 shows the SFRD for the combined ROLES75 CDFS, FIRES, and GOODS-FORS2 populations at a redshift of $z \sim 0.75$. Also shown are the SFRD results from ROLES1 (Gilbank et al., 2010b) split into CDFS, FIRES, GOODS-FORS2, and GDDS at a redshift of $z \sim 1$. For further redshift evolution comparisons, the SFRD results of Juneau et al. (2005) are shown for three redshift ranges: $z \sim 0.05$ (SDSS), $z \sim 0.975$ (GDDS), and $z \sim 1.35$ (GDDS). These three datasets from Juneau et al. (who used a BG03 IMF, same as this work) correspond to:

- an SFRD based upon modelling of measured emission line fluxes detected in galaxies in the local universe (Brinchmann et al., 2004, derived from targets in SDSS) and converted to a BG03 IMF, with $14.5 < r < 17.77$ and $0.005 < z < 0.22$;

- an SFRD derived from [OII] emission line luminosity measurements of selected galaxies in the Gemini Deep Deep Survey (GDDS) with $K < 20.6$ and $z < 1.6$;

- an SFRD derived from rest-frame UV continuum luminosity ($L_{2000\text{Å}}$) measurements of selected galaxies in GDDS with $K_{Vega} < 20.6$ and $1.2 < z < 2$. The $L_{2000\text{Å}}$ luminosity

was defined as the absolute rest-frame AB magnitude measured from the continuum flux within a 200Å window centered at 2000Å.

The empirical correction described by Equation 4.3 was applied to the [OII] luminosty derived results of Juneau et al. for the purposes of comparison with the ROLES SFRD.

The ROLES75 SFRD shown in Figure 5.9 is consistent with the ROLES1 SFRD in the mass range of $10^{8.85} < M^* < 10^{9.8} M_\odot$. However above this mass range the ROLES75 SFRD becomes increasingly lower than the ROLES1 SFRD by a factor of 2-4 in the range of $10^{10} < M^* < 10^{10.7} M_\odot$. This behaviour is unusual given that the Juneau et al. SFRD at $z \sim 0.975$ matches and extends the ROLES1 result as expected for stellar masses above $M^* \sim 10^{9.6} M_\odot$. Gilbank et al. (2010b) found that there was only a change in overall SFRD normalization (and not shape) between the different SFR indicators used to probe the SFRD at various epochs accross this mass range. Thus we should expect the shape of the ROLES75 SFRD to be the same as that of ROLES1, however the normalization should be lower given our earlier result suggesting that the [OII] luminosity function shifts to lower luminosities with decreasing redshift (recall Equation 4.2).

The four binned SFRD values at stellar masses of $Log(M^*/M_\odot) = \{10.04,\ 10.3,\ 10.54,\ 10.78\}$ indicate that the ROLES75 SFRD does not follow a simple scaling, reducing it to lower star formation rate densities equally for all stellar masses. In the low mass end there is one unusually high SFRD value at $M^* \sim 10^{9.05} M_\odot$ which lies above the ROLES1 results at this stellar mass. Considering the error on these ROLES75 SFRD measurements does not make it consistent with the idea of a constant SFRD scaling, as proposed by Gilbank et al.. The ROLES75 SFRD shows a gradually increasing SFRD towards higher stellar masses, with sharp drop-offs at the ends where the combined ROLES75 and FORS2 dataset becomes incomplete. The slope of this increasing SFRD with stellar mass is expected to be smooth, running parallel with the slope of the ROLES1 results across the mass range of $10^{8.85} < M^* < 10^{10.5} M_\odot$.

In Figure 5.10 the effects of environment are shown for ROLES75. Across the entire mass range of $8.85 < Log(M_*/M_\odot) < 11$ it is clear that the presence of structure is driving up the SFRD in this stellar mass range with the slope of the field population being very shallow but showing a gradual decrease in SFRD with increasing stellar mass. The opposite is apparent in the structure population where the SFRD increases with increasing stellar mass. The difference in structure and field SFRDs in the high stellar mass end indicates that there is a higher fraction of active galaxies in high density environments than those in the low density environment. The 'bump' in the structure population SFRD between $10^{10.5} < M^* < 10^{11} M_\odot$ was also found in the SF-GSMF (see Figures 5.7 and 5.8) and is attributed to the large scale structure in the CDFS field (recall Figure 4.3) as most of the

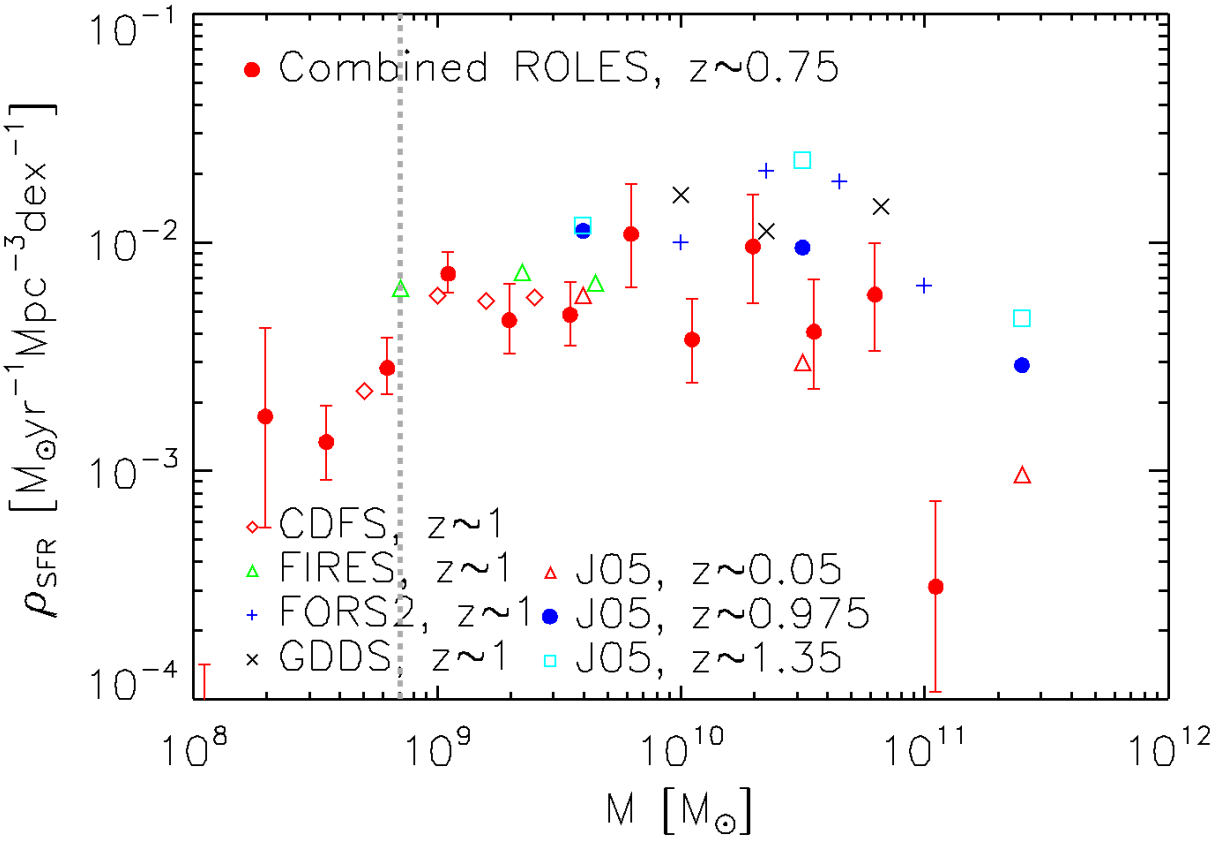

Figure 5.9: SFRD of the ROLES75 data set. The axes are $\rho_{SFR}[M_\odot yr^{-1}\mathrm{Mpc}^{-3}dex^{-1}]$ vs. $M_*[M_\odot]$. ROLES75 data, consisting of combined CDFS, FIRES, and FORS2 (solid red circles), is shown with error bars. Higher redshift ROLES1 data [CDFS (open red diamonds), FIRES (open green triangles), FORS2 (blue plus signs), and GDDS (purple X's)], are shown without error bars for comparison purposes. Similarly, data from Juneau et al. (2005) [$0 < z < 0.1$ (SDSS, open red triangles), $0.8 < z < 1.15$ ($L_{[OII]}$ derived, solid blue circles), $1.15 < z < 1.55$ ($L_{[OII]}$ derived, open turquoise squares)] are also shown without error bars, for the purpose of clarity. The thick grey vertical dashed line highlights the mass limit of this survey.

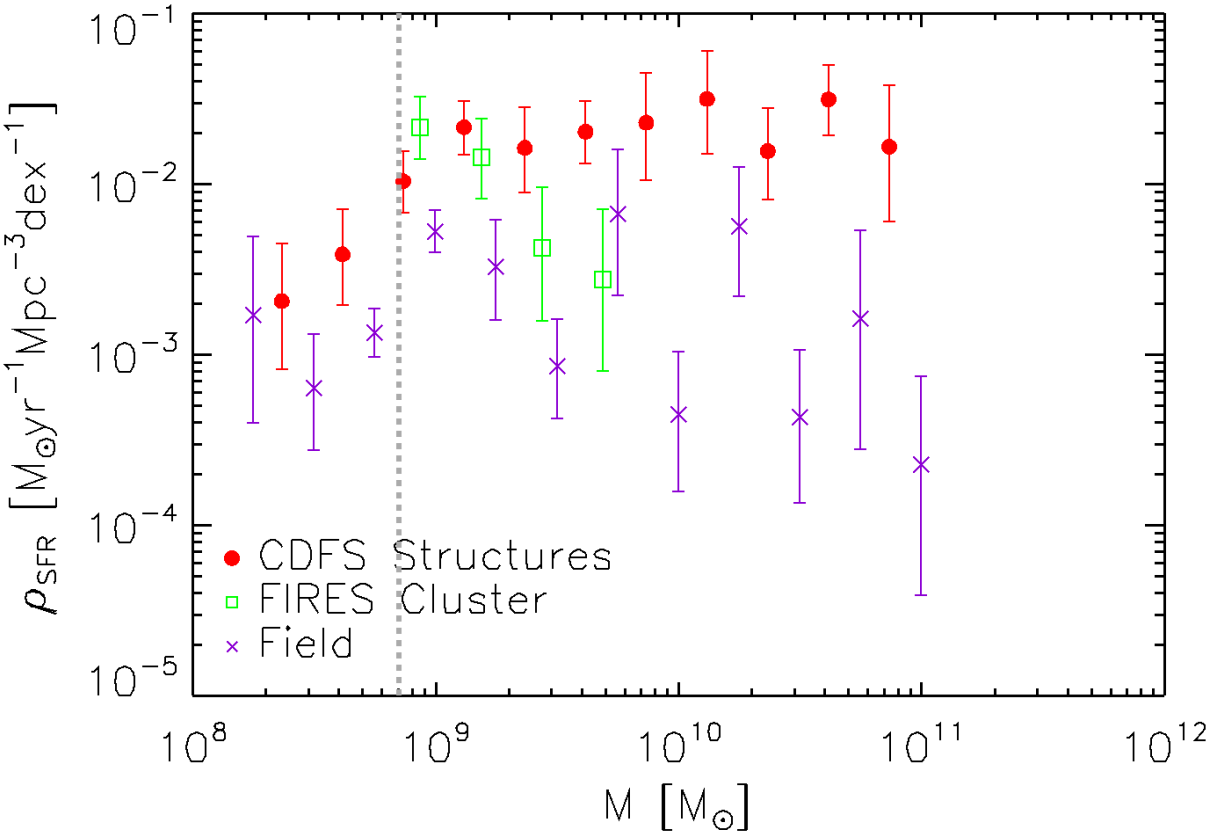

Figure 5.10: SFRD of the ROLES75 data set. The axes are $\rho_{SFR}[M_\odot yr^{-1}\mathrm{Mpc}^{-3}dex^{-1}]$ vs. $M_*[M_\odot]$. The data set has been divided into high density [ROLES75 + FORS2 CDFS Structure (solid red circles), FIRES Cluster (open green squares)], and low density [ROLES75 + FORS2 field (purple X)] environments. The thick grey vertical dashed line highlights the mass limit of this survey.

FORS2 galaxies fall within one of the two structure redshift ranges. The SFRD value in the low mass end which is higher than the interpolated slope of the $SFRD - M^*$ relation at that location coincides with an increase in SFRD away from the smooth slope in the ROLES1 SFRD at the same stellar mass, albeit on a smaller scale. This feature is present in the combined ROLES75 $SFRD - M^*$ relation of Figure 5.9 and in the CDFS structure population of Figure 5.10. The error bars of the field population in Figure 5.10 are too large to be able to confidently suggest the existence of this feature. The ROLES75 mass completeness limit is immediately adjacent to this feature on the low stellar mass side, thus we are unable to confirm whether the SFRD continues to increase with yet lower stellar masses, or drop off again.

In §5.3 we suggested that this 'bump' or 'upturn' could be evidence of a bimodal galaxy population, as discussed by Drory et al. (2009). If the assembly rate of galaxies with $M^* < 10^{11} M_\odot$ increased at this epoch then the star forming GSMF and SFRD would see an increased contribution from the lower mass satellites. The population of central galaxies with lower stellar masses would have a lower SFRD than their higher mass counterparts. The $SFRD - M^*$ curve of the central galaxies would combine with the $SFRD - M^*$ curve of the satellite galaxies, causing the SFRD to peak where the two populations maximally overlap in stellar mass which would correspond to the location of the upturn.

The idea that a high density environment might increase the SFR for the galaxies evolving within them should be more apparent in Figure 5.13 which shows specific star formation rate as a function of stellar mass. If the SFR was enhanced for high mass galaxies which formed and evolved in high density environments then the sSFR for a given high mass bin in Figure 5.13 should be higher for the cluster/structure samples than for the field population. Given the error bars shown in Figure 5.13 it is not clear if this trend is present even though it is in the SFRD environment plot of Figure 5.10. Two of the high mass bins for the sSFR of the field population (at $M^* \sim 10^{10.28}, 10^{10.74} M_\odot$) lie at similar levels as the sSFR of the sample which evolved in a high density environment, while three others (at $M^* \sim 10^{10}, 10^{10.48}, 10^{11} M_\odot$) lie below the structure sSFR. Thus we are unable to conclude that environment has influenced the specific star formation rate of galaxies forming in high density environments in the mass range of $M^* \gtrsim 10^{10} M_\odot$ at $z \sim 0.75$. Therefore this conclusion neither confirms nor denies the observation of an increased fraction of active (increased SFR) high stellar mass galaxies residing in high density environments as opposed to those residing in low density regions.

In Figure 5.11 we re-create a portion of the SFRD-redshift plot of Juneau et al. (2005, i.e. Figure 2). We have added the SFRD results from this work, as well as from ROLES1, and we exclude the results from Hopkins (2004). The [OII] luminosity derived Juneau et al. results were empirically corrected using Equation 4.3 so they could be compared with the

ROLES SFRD-redshift results. Clearly the SFRD for a given mass range decreases with decreasing redshift for all three stellar mass ranges examined by Juneau et al.. However, due to the empirical correction of the [OII] luminosity based results, there are large 'jumps' where the $L_{[OII]}$ based SFRD joins with the SFRD derived from the UV continuum luminosity (within a narrow filter centered at 2000Å). These discontinuities are not present in the original plot of Juneau et al. (2005, i.e. Figure 2). A similar trend shows that the SFRD for a given redshift bin gets progressively higher as the stellar mass range considered decreases, up until $z \gtrsim 1$. At higher redshifts the empirical correction is likely over-correcting for the extinction of the higher stellar mass galaxies since the most distant [OII] luminosity derived binned SFRD values are higher than those of the low stellar mass bins. The ROLES75 and ROLES1 SFRD data points lie above the $10.2 < Log(M^*/M_\odot) < 10.8$ stellar mass series as expected, however the $z \sim 1.5$ data points corresponding to the stellar mass range of $9 < Log(M^*/M_\odot) < 10.2$ fall below the mid-stellar mass range data. Juneau et al. admit that their sample is incomplete below $M^* \sim 10^{10.2} M_\odot$ across the entire redshift range explored in Figure 5.11 and that their lowest mass data points are shown as lower limits.

5.4.1 Star Formation Rate Density: Summary of Section

The key results of the SFRD section are:

1. The key result of ROLES1 of the existence of a constant scale factor applicable to the local SDSS SFRD to attain the ROLES1 SFRD is not confirmed for ROLES75. There is a weak suggestion that in the low mass end of the SFRD, such a scale factor may be applicable. However in the high stellar mass end, the ROLES75 SFRD is lower than would be expected based upon the application of such a scale factor.

2. The environment is highly influential in the high stellar mass end with the structure SFRD being much larger than the field. This is attributed to the difference in the shapes of their respective mass functions rather than enhanced star formation rates in a high density environment.

5.5 sSFR

In this section we discuss our results regarding the effect of environment on the specific star formation rate of ROLES75 [OII] emission line galaxies. As in the previous sections

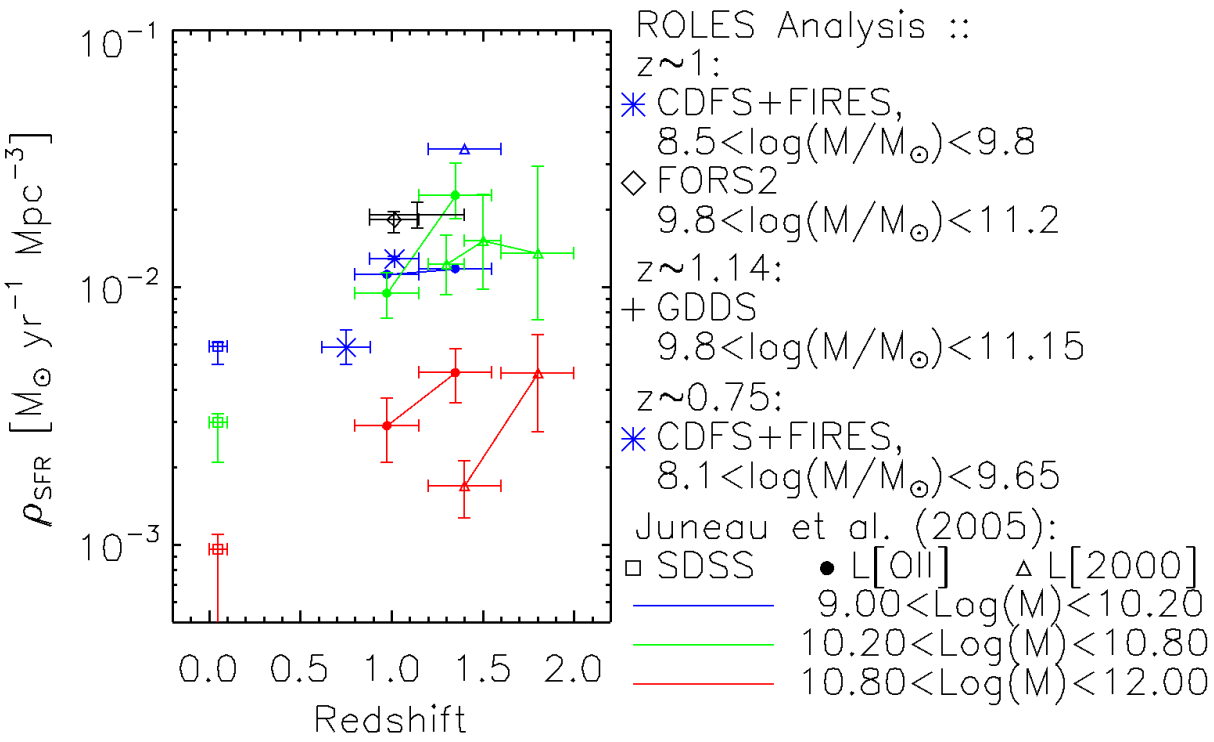

Figure 5.11: SFRD of the ROLES75 and ROLES1 data sets, added to Juneau et al. (2005, eg. Figure 2). The axes are $\rho_{SFR}[M_\odot yr^{-1}\mathrm{Mpc}^{-3}]$ vs. Redshift. SFRD determined by ROLES1 for the combined CDFS + FIRES (blue asterisk), FORS2 (black diamond), and GDDS (black plus sign) are shown for $z \gtrsim 1$. SFRD determined by this work is plotted as the combined CDFS + FIRES (blue asterisk) for $z \sim 0.75$. The higher mass Juneau et al. (2005) data is shown for local SDSS galaxies (open squares), distant $L_{[OII]}$ derived SFRD (solid circles), and distant $L_{[2000]}$ derived SFRD (open triangles).

we present the main ROLES75 sSFR results in Figures 5.12 and 5.13. Common to each, we highlight lines of constant SFR (dashed black lines), the approximate ROLES75 sSFR limit (dashed blue line), and a cloud of small filled circles corresponding to the individual ROLES75 emission line galaxies (colored by type).

Figure 5.12 shows the *binned mean* sSFR of the ROLES75 combined CDFS + FIRES + FORS2 sample (solid red circles), ROLES1 (solid black circles), and local SDSS (open black diamonds) datasets. In this case, *binned mean* refers to the mean of the sSFRs of all emission line galaxies found in a given bin of stellar mass. This binning method is different than what was done for the [OII] LF, SF-GSMF, and SFRD, however the motivation was to be able to compare the result with Gilbank et al. (2011, i.e. Figure 3). A quadratic function was fit to the *mass complete* fraction of the ROLES75 sSFR population, with the resulting fit defined as:

$$LogsSFR[yr^{-1}] = (0.128) \cdot [Log(M_*/M_\odot)]^2 - (3.09) \cdot [Log(M_*/M_\odot)] + 8.06 \qquad (5.7)$$

None of the ROLES75, ROLES1, nor local SDSS $sSFR - M^*$ curves are linear over the range of stellar masses each explored. For the ROLES75 sample across a mass range of $10^{8.85} < M_* \lesssim 10^{11} M_\odot$, this non-linearity is indicated by the locations of the points representing the full ROLES75 sSFR sample and those of the binned mean sSFR values which do not deviate significantly from the quadratic curve of best-fit. This indicates that while the specific star formation rate generally decreases with increasing stellar mass, the rate of decrease also slows with increasing mass. The binned mean ROLES1 sSFRs, which lie above the best-fit curve, exhibit the same trend but with a slightly more shallow curve for all binned stellar masses in the sample. With increasing stellar mass, the ROLES1 sSFR values appear to asymptotically approach a constant sSFR of $\sim 10^{-10} yr^{-1}$. The local SDSS sSFR runs below the best-fit curve for all stellar masses explored, and in contrast to the ROLES samples, the rate of decrease of sSFR with increasing stellar mass gets larger with stellar mass. Below a mass of $M_* \sim 10^{9.7} M_\odot$, the SDSS population also seems to asymptotically approach a constant sSFR of $\sim 10^{-10} yr^{-1}$, towards lower stellar mass.

Above our conservative mass limit, the low stellar mass end upturn, in comparison to the low mass end slope of the local SDSS sample, is present for the ROLES75 $sSFR - M^*$ sample shown in Figure 5.12. For stellar masses in the range of $10^{9.3} < M* < 10^{9.78} M_\odot$, the ROLES75 $sSFR - M^*$ sample exhibits a downward shift away from the ROLES1 population, before increasing in sSFR again to return to tracing the ROLES1 sample for stellar masses above $M^* \sim 10^{9.78} M_\odot$. Considering the error bars, this shift is likely insignficant but nonetheless, may be influenced by the use of an un-weighted mean to calculate the binned sSFR values. There is a pronounced 'dip' in the ROLES75 sample

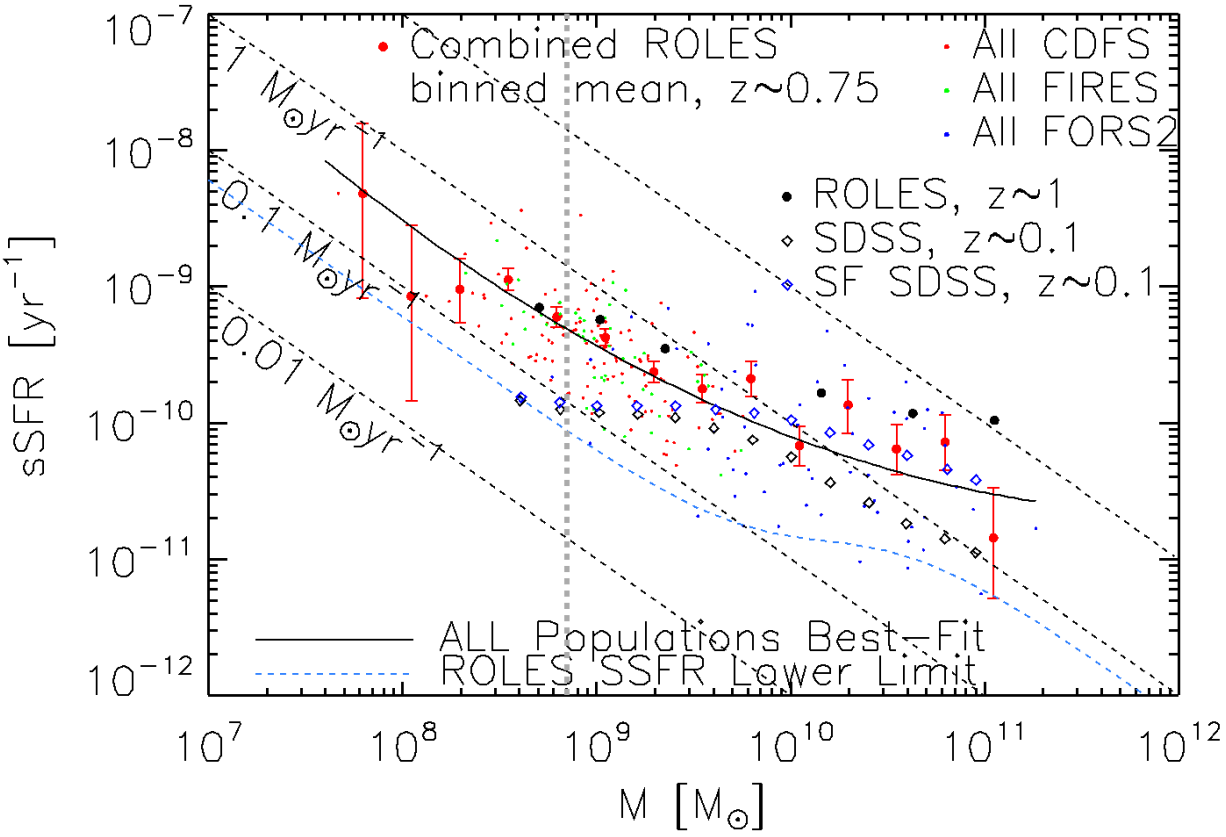

Figure 5.12: *Binned mean* sSFR of the ROLES75 data set. The axes are $sSFR[yr^{-1}]$ vs. $M_*[M_\odot]$. ROLES75 data, consisting of combined CDFS, FIRES, and FORS2 (solid red circles), is shown with error bars. Higher redshift ROLES1 data [CDFS, FIRES, FORS2, GDDS combined (solid black circles)], is shown without error bars for comparison purposes. Similarly, data from Juneau et al. (2005) [$0 < z < 0.1$ (ALL SDSS, open black diamonds; Star Forming SDSS, open blue diamonds)] are also shown without error bars, for the purpose of clarity. A best-fit curve to the entire ROLES75 sample is shown (thick continuous black line), the sSFR limit is identified (thin blue dashed line), and lines of constant SFR (thin black dashed lines) are highlighted. The thick grey vertical dashed line highlights the mass limit of this survey.

at $M^* \sim 10^{10} M_\odot$ which was also present in the ROLES75 combined SFRD shown in Figure 5.9 and the field population shown in Figure 5.10. The ROLES75 field population sSFR exhibits the dip as well however the structure population does not (see Figure 5.13). This feature is attributed to the binning process. The ROLES75 combined sSFR has a bin located at this stellar mass, as does the field sSFR population. However the structure sSFR population does not. Therefore this mass bin in the combined sSFR sample is dominated by the counts in the corresponding field bin.

The SDSS sSFR sample corresponding to *all* galaxies and the sample which represents only those which are star forming were extracted from Figure 3 of Gilbank et al. (2011) and plotted in Figure 5.12 of this work for comparison purposes. The ROLES1 sSFR comparison sample corresponds only to galaxies of *all colors*. The 'blue cloud' SDSS population is a result of the application of a blue color cut, selecting only those galaxies which are star-forming based upon the analysis of a ($V_{606} - i_{775}$) - i_{775} color magnitude diagram. It is clear in Figure 5.12 that the ROLES1 $sSFR - M^*$ results are normalized to higher sSFRs in comparison to the local star forming SDSS sample, however the shapes of each $sSFR - M^*$ curve are consistent for $M^* > 10^{9.5} M_\odot$. Below this mass threshold the ROLES1 $sSFR - M^*$ curve exhibits an upturn with decreasing stellar mass. This color selection should not change the results of the ROLES75 $sSFR - M^*$ relation as ROLES selected blue star forming galaxies through the observation of [OII] emission lines as part of the survey strategy, and these galaxies are sufficiently low in stellar mass as to not be significantly effected by extinction. The FORS2 population is a higher mass sample which would certainly see its galaxies extincted by the increased amount of obscuring dust. Therefore the extended high stellar mass end of the ROLES75 $sSFR - M^*$ could change with the application of this color cut. The color selected local SDSS sSFR sample is heavily influenced by the cut in the high stellar mass end where the red sequence galaxies have been removed from the population, thus increasing the sSFRs in the high mass end to run approximately parallel with the ROLES75 and ROLES1 samples. Of course, the statements on the predicted influence of the color cut on the ROLES75 sample are qualitative and can only be confirmed by applying the color selection, which is planned for future work. Overall the ROLES75 combined $sSFR - M^*$ trend shown in Figure 5.12 confirms observations from other works (Brinchmann et al., 2004; Elbaz et al., 2007; Popesso et al., 2011) suggesting that the observed star formation rate decreases for galaxies consisting of larger stellar masses already in place.

In Figure 5.13 the results have been separated into high density (CDFS structure (solid red circles), FIRES cluster (open green squares)) and low density (field, open purple diamonds) environments. Both high and low density populations show a decreasing specific star formation rate with increasing stellar mass. The low density field population of the

ROLES75 sSFR is consistent with the high density structure population for masses in the range of $M^* < 10^{10} M_\odot$. Their normalizations are equal and the shapes of their respective $sSFR - M^*$ curves are consistent in this mass range. For stellar masses above $M^* \sim 10^{10} M_\odot$ the field population brackets the best-fit line for five mass bins, however with large scatter. Meanwhile, the structure population is consistently above the $sSFR - M^*$ trendline for three of five stellar mass bins, considering the error bars.

In an effort to quantitatively confirm whether the ROLES75 $sSFR - M^*$ high density structure sample is different from the low density field population, a Kolmogorov-Smirnov (K-S) statistical test was performed between four different subsamples. The test was performed as follows:

1. Four residual $sSFR - M^*$ populations were determined for each of the high density (CDFS ROLES75 + FORS2, ROLES75 FIRES, combined ROLES75 + FORS2) and low density (combined ROLES75 + FORS2) $sSFR - M^*$ populations. For a given bin of stellar mass, the residual sSFR was defined as the difference between the population sSFR and the sSFR of the best-fit line for this stellar mass bin center. See Figure 5.14;

2. A two sided K-S test was performed between each of the high density residual populations with the low density residual field population. A fourth test was performed between the CDFS ROLES75 + FORS2 high density residual dataset and the ROLES75 FIRES cluster residual sample;

3. The resulting K-S probability statistic indicated the likelihood that the two populations originated from the same distribution. The higher the probability, the more likely the two test populations were derived from the same distribution.

Figure 5.14 and Table 5.2 show histograms of the residual populations tested and the resulting K-S probability statistics. The K-S test results for the comparisons between the low density field residual population, and the two high density residual populations containing the CDFS structure and extended high stellar mass FORS2 subset, confirm that it is highly likely that the residual sSFR structure populations originated from the same distribution as that of the residual sSFR field population ($Prob._{K-S} \sim 0.95$ for these two tests). The probability that the high density residual sSFR FIRES cluster sample originated from the same distribution as the residual sSFR field population is low, with $Prob._{K-S} = 0.533$. This is reasonable since the FIRES sSFR was not extended to higher stellar masses which are included in the field population. For the same reason there is also a very low probability that the residual sSFR CDFS structure sample and the residual

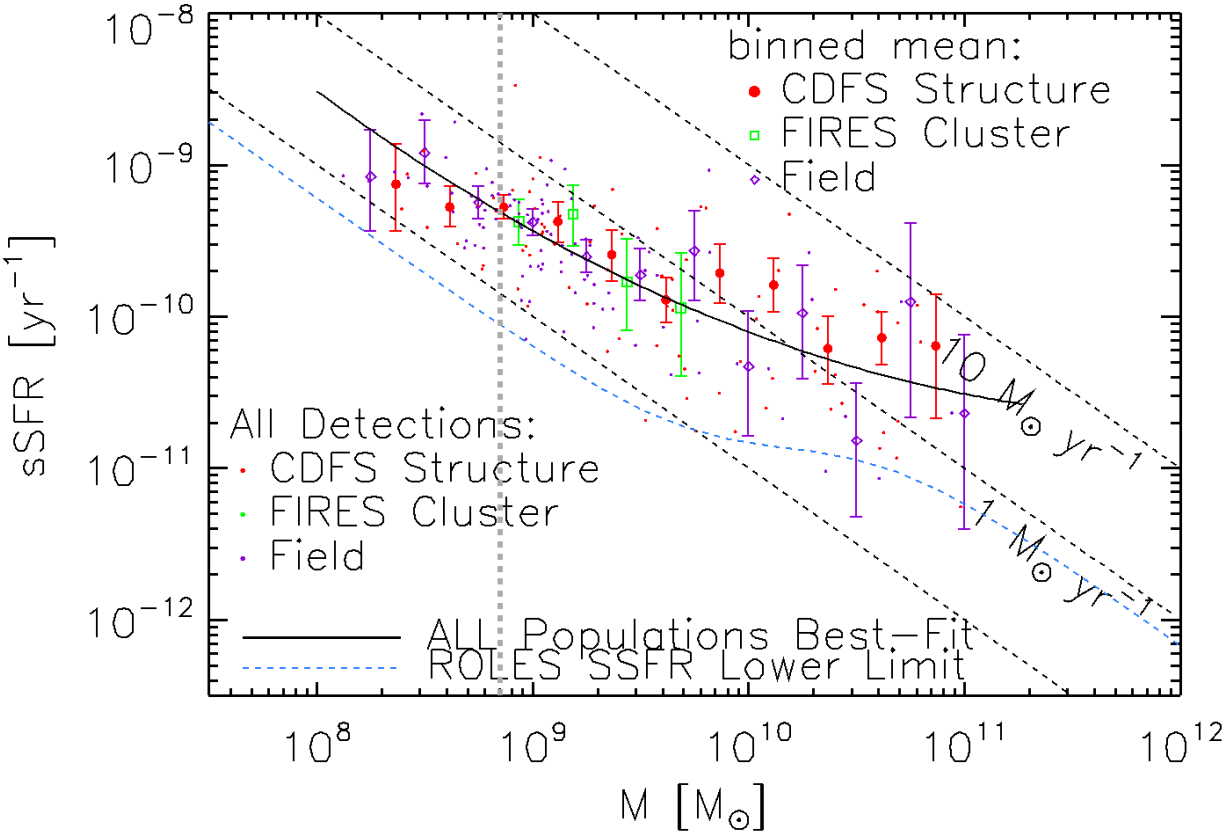

Figure 5.13: *Binned mean* sSFR of the ROLES75 data set. The axes are $sSFR[yr^{-1}]$ vs. $M_*[M_\odot]$. The data set has been divided into high density [ROLES75 + FORS2 CDFS Structure (solid red circles), FIRES Cluster (open green squares)], and low density [ROLES75 + FORS2 field (purple X)] environments. A best-fit line to the entire ROLES75 sample is shown (thick continuous black line), the sSFR limit is identified (thin blue dashed line), and lines of constant SFR (thin black dashed lines) are highlighted. The thick grey vertical dashed line highlights the mass limit of this survey.

Table 5.2: Results of the Kolmogorov-Smirnov statistical tests performed between each of the high density residual sSFR samples with the residual field sSFR sample, and between the CDFS structure and FIRES cluster residual sSFR samples. (see Figure 5.14).

Comparison	K-S Prob.
CDFS Structure-FIRES Cluster	0.232
CDFS Structure-FIELD	0.957
FIRES Cluster-FIELD	0.533
Combined Structure/Cluster-FIELD	0.957

sSFR FIRES cluster population come from the same distribution. These K-S test results confirm that the ROLES75 high density CDFS structure $sSFR - M^*$ population does not statistically differ from the low density field $sSFR - M^*$ sample. As such, the statement earlier regarding that both of the high and low density populations show a decreasing specific star formation rate with increasing stellar mass, can be made stronger. The K-S tests suggest that the rate of decrease of the specific star formation rate with increasing stellar mass, is statistically equal between the high and low density populations.

In Figure 5.15 we re-create the density segregated, $sSFR - M^*$ plot from Li et al. (2011, i.e. Figure 6). In this plot we show the density-dependent $sSFR - M^*$ curves for each of the local SDSS, ROLES75, and ROLES1 epochs. The local SDSS and ROLES1 samples were segragated according to a density parameter, ρ_5, which is defined in detail in Li et al.. Briefly, ρ_5 indicates the redshift-completeness weighted number density of star-forming galaxies limited to $M_{K_{AB}} \leq -21.0$, found within a 'nearest-neighbour' volume defined by the five closest galaxies to the current galaxy being evaluated. The volume is defined by the maximum projected radius of the set of five nearest-neighbour galaxies, and the difference in co-moving distances set by the *closest* and *farthest* nearest-neighbour galaxies *to us*, in redshift space. Li et al. set a threshold of $\rho_5 = 0.31 Mpc^{-3}$ to represent the difference between galaxies forming in high or low density environments. The ROLES75 $sSFR - M^*$ population was not segregated according to the ρ_5 density parameter. Rather, we use the same structure and field $sSFR - M^*$ populations shown in Figure 5.13. We acknowledge that the different methods used to divide the ROLES75 and ROLES1 / SDSS $sSFR - M^*$ populations are likely to influence the results presented in Figure 5.15. However, this plot is

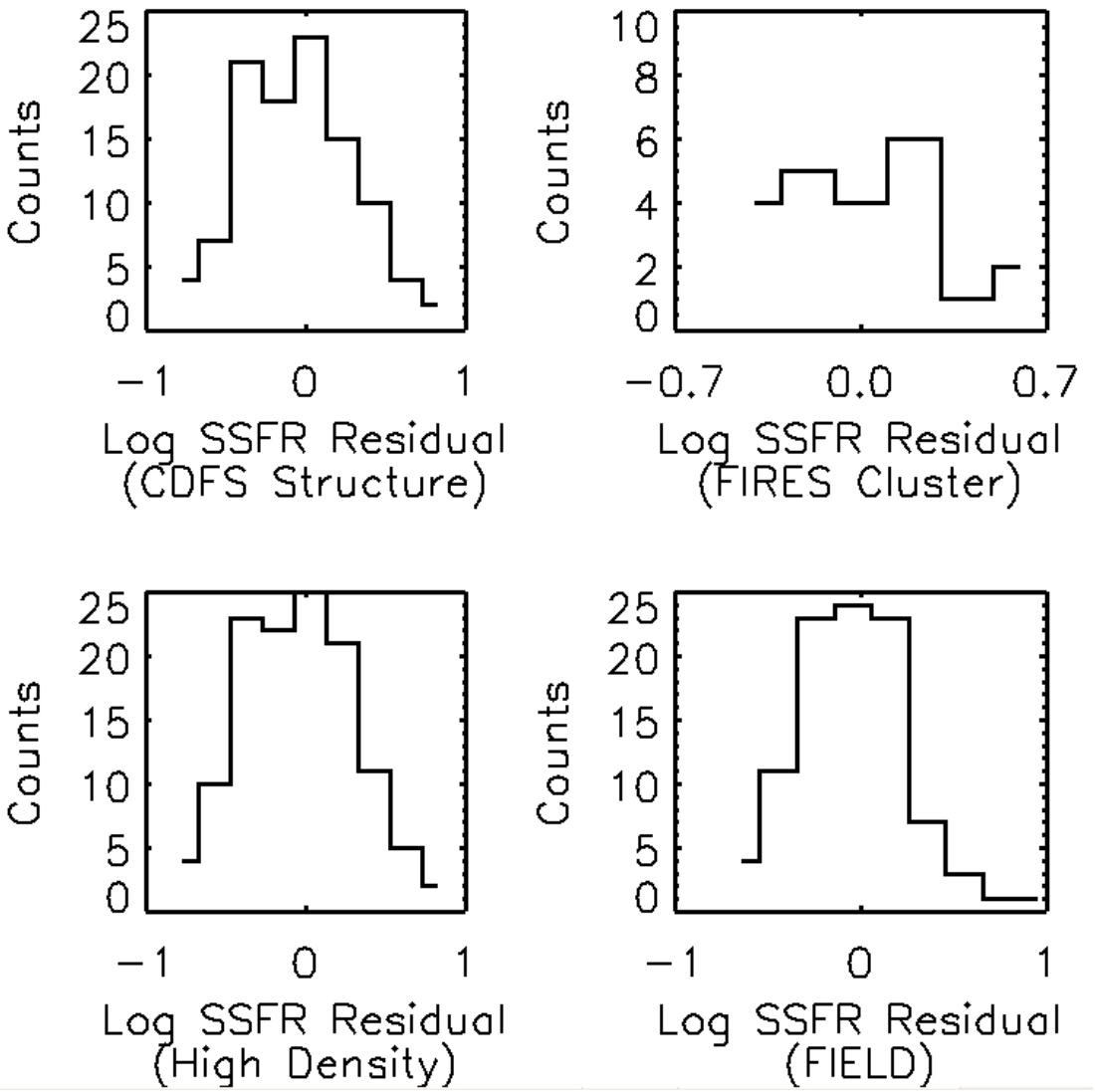

Figure 5.14: The histograms of the residual sSFR, with the full sample best-fit line, of the four populations of Figure 5.13 are shown. A Kolmogorov-Smirnov statistical test was performed between each of the high density residual sSFR samples with the residual field sSFR, and between the CDFS structure and FIRES cluster residual sSFR samples. See Table 5.2 for the results.

meant to be a qualitative plot, allowing us to observe the role of environment as a function of epoch.

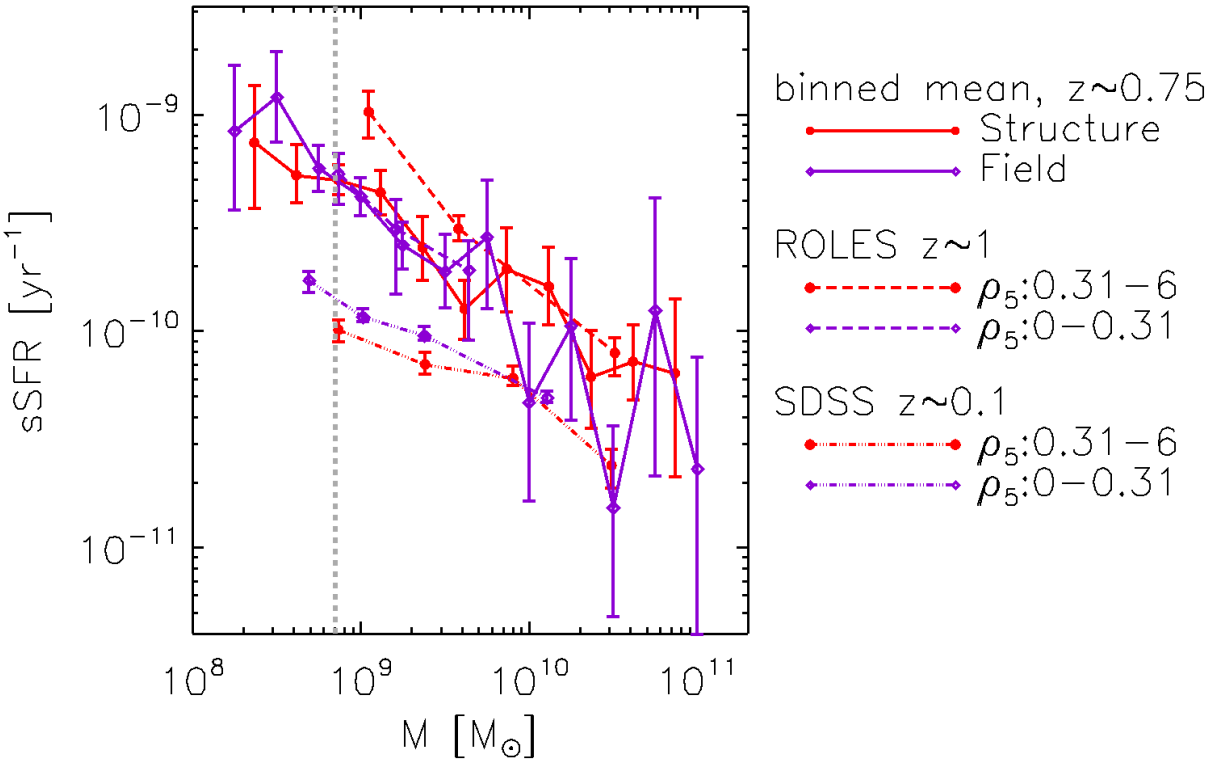

Figure 5.15: sSFR of the ROLES75 data showing $sSFR[yr^{-1}]$ vs. $M_*[M_\odot]$. Here we re-produce a portion of the high-vs.-low density environment plot from Li et al. (2011, eg. Figure 6). ROLES75 sSFR (combined with FORS2) is shown as high density structure/cluster (red solid circles connected by continuous red lines) and low density field (open purple diamonds connected by continuous purple lines). The highest density ROLES1 and local SDSS (ROLES1 analysed) sSFR are shown as red solid circles connected by red long dashed and '$-\cdots-$' lines respectively, while the lowest density counterparts are shown as open purple diamonds connected by purple long dashed and '$-\cdots-$' lines respectively. The thick grey vertical dashed line highlights the mass limit of the survey.

All of the $sSFR-M^*$ populations in Figure 5.15 have slopes which are consistent with one another for stellar masses of $M^* \gtrsim 10^{9.7}M_\odot$. Below this mass we see a gradual upturn of the high density $sSFR-M^*$ curves as we progress from the local universe to $z\sim1$. The evolution of this upturn does not appear to be present in the low density $sSFR-M^*$

populations (excluding the two highest and lowest stellar mass bins of the ROLES75 high and low density $sSFR - M^*$ populations). The low density $sSFR - M^*$ populations are parallel to one another with the normalization of each increasing with increasing redshift. In contrast the evolution of the sSFR high density environment normalization is larger in the low stellar mass end compared with the high stellar mass region, suggesting a stellar mass dependent evolution.

Most interesting is the observation that the normalization of each of the high and low density environment $sSFR - M^*$ populations appears to 'flip' or 'rollover' sometime between the present day and $z \sim 1$. The local SDSS sample shows that the low density environment $sSFR - M^*$ curve is consistently higher in sSFR than its high density counterpart for the full stellar mass covered by the SDSS sample. Conversely, the ROLES1 dataset shows that the low density environment $sSFR - M^*$ curve is consistently lower in sSFR than its high density counterpart across comparable stellar mass ranges for the ROLES1 sample. At each epoch, the low density $sSFR - M^*$ curve does not extend to the high stellar mass range which is reached by the high density $sSFR - M^*$ curves, therefore this comparison between epochs is only applicable for common stellar mass ranges of $10^{8.8} < M^* < 10^{9.7} M_\odot$. It is tantalizing to suggest that this 'rollover' in density-dependent $sSFR - M^*$ occurs at $z \sim 0.75$ since the ROLES75 high and low density $sSFR - M^*$ curves are not separated in sSFR. However, recall that the ROLES75 $sSFR - M^*$ results shown here are not segregated into different density formation environments using the ρ_5 method. Plans to convert the ROLES75 specific star formation rate dataset into high and low density galaxy formation environments, based upon the ρ_5 method of Li et al. (2011), are reserved for future work. However, qualitatively, for the specific stellar mass range of $10^{8.8} < M^* < 10^{9.7} M_\odot$, the influence of a high density environment on the sSFR evolved significantly since $z \sim 1$, with it being the dominant environmental factor at this redshift, and changing to not be the dominant environmental factor at present time. The opposite is the case for the dominance of the low density environment on the specific star formation rate of star forming galaxies.

5.5.1 Specific Star Formation Rate: Summary of Section

The key results of the sSFR section are:

1. The presence of an 'upturn' at low stellar mass confirming the same observation in ROLES1. This upturn is not present in the local SDSS sample.

2. The $sSFR - M^*$ normalizations between the ROLES1, ROLES75, and the color-cut local SDSS samples are different but their shapes are approximately equal.

3. There is no indication that environment influences the sSFR at $z \sim 0.75$.

4. There is an increase in the sSFR toward higher redshifts with decreasing stellar mass.

5. There is a turnover effect of the sSFR dominant density regime as a function of redshift.

Chapter 6

Future Work

The success of the ROLES surveys ($z \sim 0.75, 1$) to date have prompted the plan to continue the survey up to a redshift of $z \sim 1.7$. At the epoch of $z \sim 2$ both the cosmic star fomation rate and the accretion rate of supermassive blackholes had peaked (See Hopkins & Beacom, 2006; Boyle & Terlevich, 1998, i.e Figure 1 of each), suggesting that this was the most active era of galaxy formation (herein referred to as the *critical epoch of galaxy formation*). Also important at this redshift is that it has been suggested that the primary mechanism for galaxy formation changes from a rapid rate of cold gas accretion to a slow accretion rate of warm gas. The cause of this change may be a result of the presence of newly formed hot stars, forcing the cooling efficiency of accreting gas to be reduced, resulting in a mode of warm gas accretion (Bouché et al., 2010).

The galaxy stellar mass functions shown in Figure 5.7 indicate that there is surprisingly very little change since $z \sim 3$ in the abundance of star forming galaxies with stellar masses of $M > 10^{11} M_{\odot}$. This suggests that the large galaxies that we see today have been in place since this distant redshift. In contrast, the lower mass galaxies appear to evolve more rapidly since this redshift, as can be seen by comparing the ROLES results to the local SDSS population in Figure 5.7. Beyond $z \sim 1$, the GSMF picture is unknown as to whether the number density of low mass galaxies continues to decrease with increasing redshift, out to the critical epoch of galaxy formation.

The SFRD results shown in Figure 5.9 of this work and in Figure 15 of Gilbank et al. (2010b, i.e. lower left panel) indicate that the peak of the SFRD is not shifting to lower stellar masses as is commonly suggested by the cosmic downsizing scenario. Rather the SFRD appears to decrease by equal amounts across all stellar masses as redshift decreases, maintaining the shape of the overall SFRD-stellar mass relation. It is an open question as

to whether this redshift evolving SFRD-stellar mass curve normalization continues to the critical epoch of galaxy formation, or if indeed the SFRD peak does shift to lower masses with decreasing redshift, but ceases by $z \sim 1$.

In the introduction it was mentioned that a problem with many galaxy star formation surveys is that they do not probe down to low galaxy stellar masses, and therefore any trends they observe are based predominantly on the activity of large galaxies. Of course the underlying cause for this is the inherrent difficulty in observing low mass / low SFR galaxies at high redshifts which are too faint to be imaged without using long exposure times. In addition to this problem, at $z \sim 2$ massive galaxies are rare and tend to be clustered, thus requiring large survey volumes to avoid cosmic variance. Due to these issues, disagreement can already be found between studies which attempt to probe down to galaxy stellar masses of $Log(M/M_{\odot}) \lesssim 10.5$ as recent as $z < 1.4$ (Bundy et al., 2006, i.e. Figure 5). High redshift surveys also tend to use photometric redshifts (photo-z's) to simultaneously determine stellar mass and star formation rates. However, stellar masses determined from photometric redshifts can vary significantly from those determined spectroscopically (Bundy, Ellis & Conselice, 2005, i.e. Figure 3), adding further difficulty to the study of galaxy formation at high redshift.

Considering these issues, it is clear that further study probing down to lower stellar masses using spectroscopic redshifts is necessary to reveal the trends of, and dominating contributions to, galaxy formation at this critical epoch.

6.1 Redshift Extension of ROLES

In September 2010 the Association of Universities for Research in Astronomy, Inc. (AURA), who operate the Gemini Observatory, purchased new red-sensitive CCDs from Hamamatsu Photonics for use with the Gemini Multi-Object Spectrographs - North (GMOS-N) instrument. These new CCDs provide improved quantum efficiency out to $1.04\mu m$ (see Figure 6.1), increasing the near-infrared capabilities of GMOS-N.

Considering the improved sensitivity limit of the (as yet to be installed) Hamamatsu CCDs ($\lambda \sim 1\mu m$ in Figure 6.1), the $[OII]_{3727\text{Å}}$ (unresolved) doublet could be observed out to $z \sim 1.7$. As this would provide an exciting opportunity to apply the ROLES survey and analysis techniques to this critical epoch of galaxy formation, an extension survey was planned. The new survey is called the Redshift One-plus GMOS Ultra-deep Emission line Survey, or ROGUES, which will image star forming [OII] emission line galaxies down to $M \sim 10^9 M_{\odot}$ with redshifts in the range of $1.2 < z < 1.7$. An observing proposal

was submitted to AURA and in June 2011 the ROGUES collaboration were awarded 10 hours of GMOS-N Band-1 time for semester 2011B with rollover status, which should be adequate time to test and prove the ROLES techniques for this epoch.

As suggested earlier, deep infrared large field surveys are required to clarify the galaxy formation picture at $z \sim 2$. Since GMOS-N is located at Gemini North in Mauna Kea, Hawaii, a field visible in the Northern sky is required. The United Kingdom InfraRed Telescope Infrared Deep Sky Survey (Lawrence et al., 2007, i.e. UKIDSS) is one such comprehensive study of the Northern sky which has been operational since 2005. Consisting of five smaller surveys, one of those, the UKIDSS-UDS (Ultra Deep Survey) with a limiting magnitude of $K < 23$ and areal coverage of ~ 0.8 square degrees will be specifically targeted by ROGUES.

In a similar manner by which targets were chosen for ROLES, ROGUES will make use of existing UKIDSS-UDS photometry, photometric redshifts, and the BzK technique (Daddi, Cimatti et al., 2004) to pre-select K-faint (low stellar mass) star forming galaxies with photometric redshifts in the range of $1.2 < z < 1.7$, which is limited by the throughput and efficiencies of the Gemini z' filter (Figure 6.2), R150 grism (dispersion=0.174 nm/pixel, 150 lines/mm, Figure 6.3), and the new red-sensitive CCD.

One of the most important aspects of the ROLES survey method was the ability to accurately subtract the flux contribution from the sky. ROGUES will also use the nod & shuffle technique and as such, slits will be 0.8" by 3" with a 3" charge shuffle distance and a 1.5" telescope nod distance. Considering the 6144x4176 pixel size of the new Hamamatsu CCD, ROGUES will be able to place three colums of 50 slits each (platescale=0.0809"/pixel) with a spectral resolution of ~ 17Å. Assuming a target placement efficiency of $\sim 50\%$ ROGUES will be able to image 75-80 high redshift galaxies in one mask. The 10 hours awarded for the survey will be completely used on this one mask which will be optimally populated in density with targets of the highest priority (highest photo-z likelihood of lying within the target redshift range and $K < 24$).

Using the integrated time calculator provided by Gemini for the new Hamamatsu CCDs, it is expected that seven stacked exposures of one hour each with $4\times$ binning[1] in both the spatial and spectral directions will yield a signal-to-noise of ~ 3 for each 17Å resolution element and [OII] emission line flux of $4 \times 10^{-18} ergss^{-1}cm^{-2}$. This is comparable to the ROLES S/N levels reached for $z \sim 0.75, 1$ (although with ROLES75 we chose a detection threshold of $S/N \sim 5$, and ROLES1 used $S/N \sim 4$, each yielding a line flux limit of approximately $6 \times 10^{-18} ergss^{-1}cm^{-2}$).

[1]The galaxies targeted by ROGUES will be seeing limited and as such ROGUES will be able to bin at high levels in the spectral and spatial directions, thus increasing detection S/N.

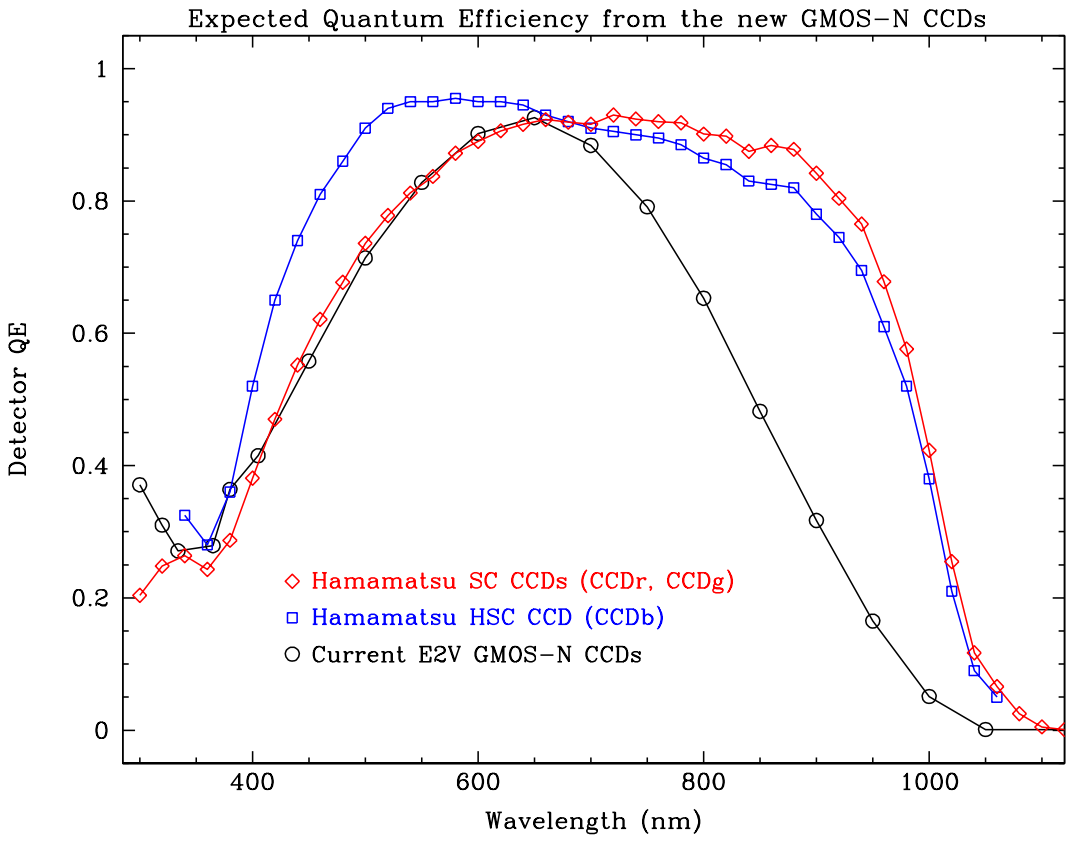

Figure 6.1: Comparisons between the quantum efficiency curves of the current CCD and the planned upgrade to the red sensitive CCDs. (Image courtesy of Gemini Observatory. See `http://www.gemini.edu/?q=node/11395`.)

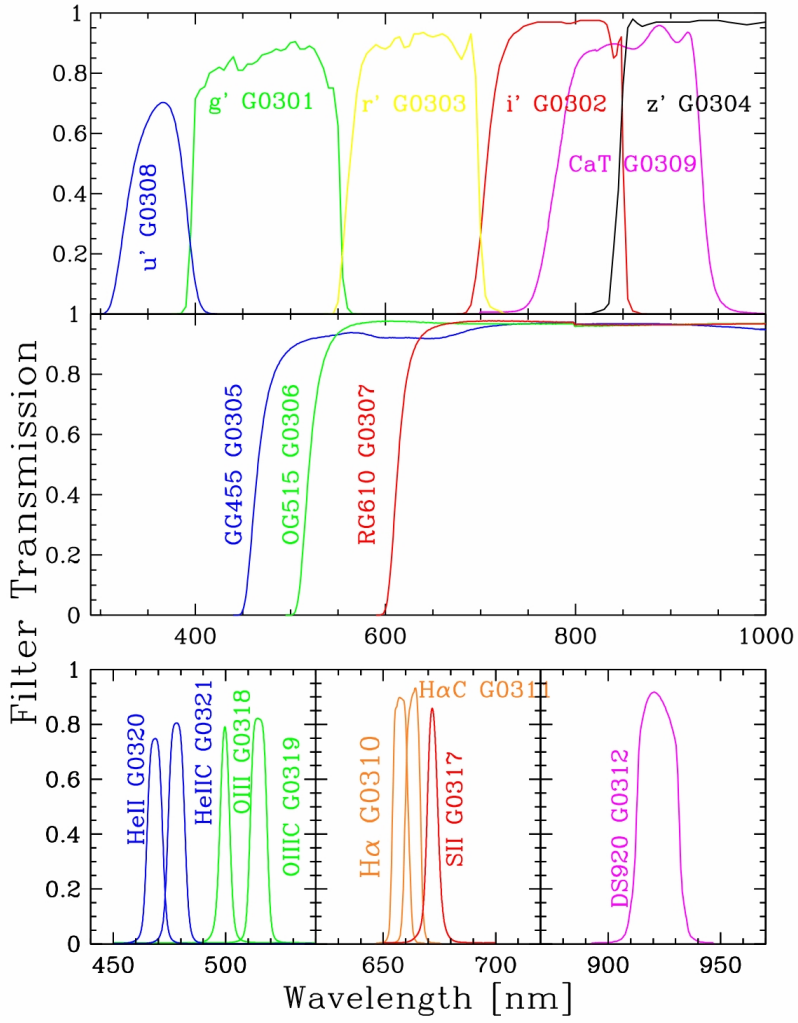

Figure 6.2: GMOS-N filter curves. The z' filter shown to the far right of the top panel is to be used by ROGUES. (Image courtesy of Gemini Observatory. See `http://www.gemini.edu/sciops/instruments/gmos/filters/filters_2009.gif`.)

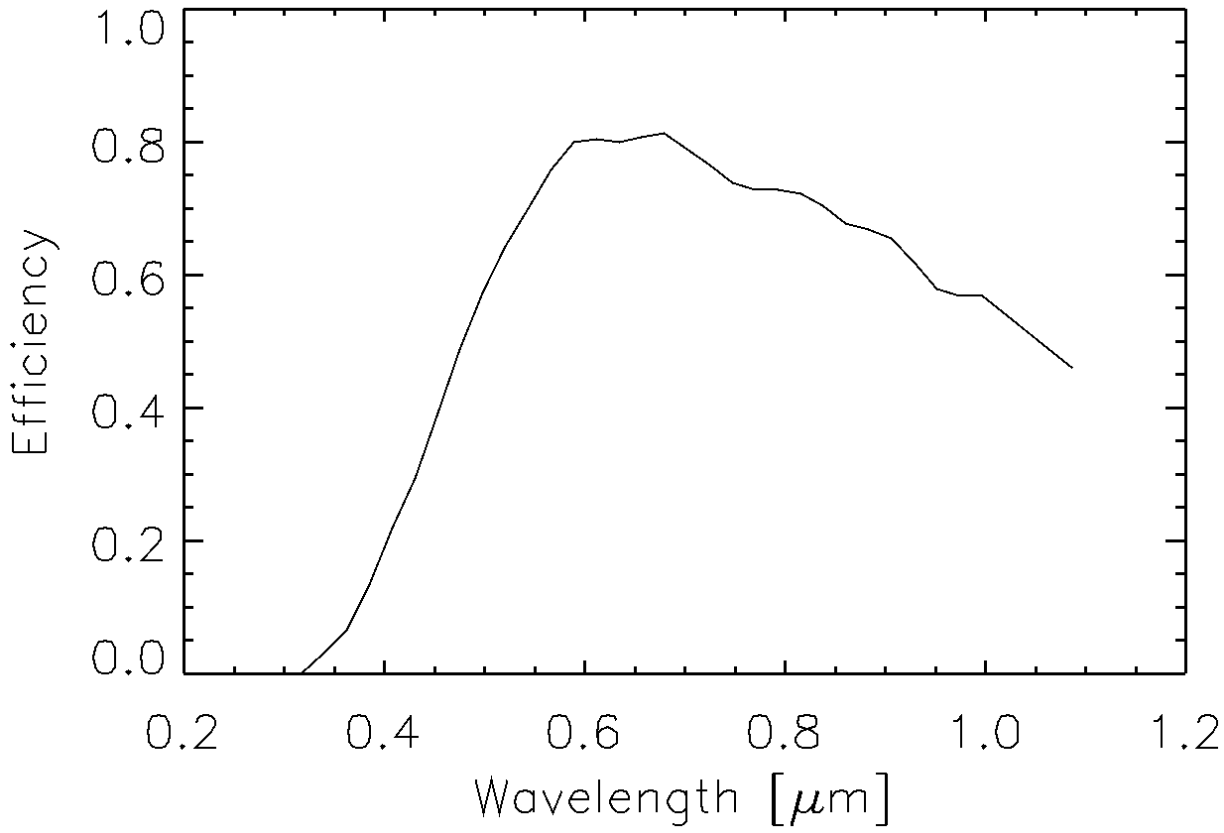

Figure 6.3: GMOS-N R150 grism efficiency curve. (Data courtesy of Gemini Observatory. See `http://www.gemini.edu/sciops/instruments/gmos/gratings/gmos_n_R150_G5306.txt`.)

Following the strategy outlined above, it is expected that the LF, GSMF, SFRD, and sSFR results from this single ROGUES survey mask will verify the applicability of the ROLES technique to the higher redshift domain. Unfortunately, as of the time of this writing, the GMOS-N upgrade to the new Hamamatsu CCDs appears to be significantly delayed. The new Hamamatsu CCD arrays failed during testing due to an ESD (electrostatic discharge) event and they have been deemed "not science worthy". As a result, Gemini plans to purchase replacement Hamamatsu CCDs for installation sometime in 2012. In the meantime, the current GMOS-N EEV CCDs will be replaced by new versions of the same type, produced by the same manufacturer. These new CCDs also have improved red sensitivity out to $0.98\mu m$.

The ROGUES survey will likely use these new EEV CCDs, however the survey will only be able to explore out to a redshift of $z \sim 1.6$. Since the current plan involves the use of only one mask for the purposes of proving the strategy and techniques at $z > 1$, the use of the EEV CCDs is not expected to dramatically change the proposed observing plan. Integrated signal-to-noise levels, flux limits, and spectral resolution will change but not enough to suggest that the ROGUES test survey be delayed. It is also expected that ROGUES will be able to analyse and publish results from the test survey mask during the planned schedule of the GMOS-N transition to the new Hamamatsu CCDs. This will place the ROGUES collaboration in a favorable position to be able to lobby for further observing time based upon a successful, proven extension of the ROLES survey methodology.

Chapter 7

Conclusion

The Redshift One LDSS-3 Emission line Survey (ROLES) was initially designed to tackle the issue of *cosmic downsizing*, first introduced by Cowie et al. (1996), and originally described as the observation where the dominant regime of galaxy formation evolved from massive galaxies at earlier cosmic times to lower mass galaxies at recent times. Since its introduction, the concept of downsizing has been divided into several specific types, two of which are frequently observed: *downsizing in stellar mass* and *downsizing in star formation rate (SFR)* (see Fontanot et al., 2009, for more details on the sub-types of downsizing). Downsizing in stellar mass suggests that the number density of low mass galaxies evolves more rapidly with redshift than the number density of higher mass galaxies. Similarly, downsizing in SFR implies that as redshift decreases, the dominant contribution to global star formation evolves from high to low mass galaxies. With these concepts in mind, the ROLES1 survey (the original survey) was designed in a manner to optimally probe galaxy formation at $z \sim 1$ and determine if downsizing was indeed present at lower mass scales.

The ROLES observation and data reduction strategy is unique in that for the first time the faint $[\mathrm{OII}]_{\lambda 3727\text{Å}}$ emission from low stellar mass galaxies ($8.5 < Log(M^*/M_\odot) < 9.5$) has been spectroscopically measured for redshift $0.62 < z < 1.15$. Using photometric redshifts, targets within the planned survey fields were pre-selected based upon their likelihood of falling within the redshift ranges of $0.62 < z < 0.885$ (ROLES75, a folow-up study corresponding to the work of this thesis) and $0.885 < z < 1.15$ (ROLES1, the previous study of Gilbank et al. (2010a,b, 2011); Li et al. (2011)). From these targets, a subset were selected based upon deep near-infrared imaging such that their K-band magnitude fell within the range of $22.5 < K_{AB} < 24.0$, which is effectively a stellar mass selection (see Figure 5.2). Image reduction of multi-object spectroscopy utilizing the Nod & Shuffle technique (for accurate sky removal) led to galaxy spectra for these targets which were

subsequently searched for [OII] emission lines. Identified lines were cataloged, had their line fluxes measured, and stellar masses were determined by SED fitting which used the spectroscopically confirmed redshifts and publically available multi-band photmetry.

One of the conclusions of the first ROLES survey at $z \sim 1$ suggested that the galaxy stellar mass function of star forming galaxies has not changed significantly since $z \sim 1$ (Gilbank et al., 2011), refuting the idea that the number density of low mass galaxies evolves more rapidly with redshift than the number density of higher mass galaxies. With regard to the star formation rate density, the ROLES1 conclusion was that while the normalization of the SFRD changes with redshift, the overall shape of the $SFRD - M^*$ curve does not change with cosmic time. This implied a constant scale factor relating the $z \sim 1$ SFRD with the local (SDSS) SFRD. Again, this is not evidence of downsizing in star formation as the dominant contribution to the [OII] luminous galaxy star formation does not shift to lower masses with decreasing redshift.

The success of ROLES1 fostered the creation of the follow-up study, ROLES75, which is the focus of this thesis. As mentioned above, ROLES75 utilized the same observational strategy as ROLES1 (identical target fields, K-magnitude range and therefore stellar mass) but targeted a lower redshift range of $0.62 < z < 0.885$. During the analysis phase of the study, it became clear that the significant structure in the CDFS field at redshifts of $z = 0.668 \pm 0.016$ and $z = 0.735 \pm 0.009$, in addition to the targeted FIRES MS1054-03 cluster, might provide valuable insight on the influence of high versus low density environment on the formation of star forming dwarf galaxies, as presented by the ROLES science objectives ([OII] luminosity function, [OII] luminous galaxy stellar mass function, star formation rate density, and specific star formation rate). At this stage the focus quickly shifted to the study of environment since most existing galaxy formation and environment studies have not probed down to the dwarf galaxy mass scale.

This investigation of the influence of environment on galaxy formation at $z \sim 0.75$ has partially lifted the veil on the impact of local density for star forming dwarf galaxes at earlier times. Some of these results help to confirm the picture as presented by ROLES1, while others are tantalizing and in need of future study. The most important results presented in this thesis are briefly mentioned in the following sections.

[OII] Luminosity Function
In Figure 5.4 of §5.2 the total [OII] luminosity function at redshift $z \sim 0.75$ was compared with [OII] luminosity functions at $z \sim 0.84$ and $z \sim 1$, as well as with the local SDSS LF. The conclusions drawn from this figure suggest that the [OII] luminosity of galaxies was higher in the past than at present day. This is evident in the observed shift of the

bright-end [OII] luminosity function slope to lower [OII] luminosities with decreasing redshift over several orders of magnitude in galaxy number density. Also apparent in Figure 5.4 is the presence of 'turnovers' in each of the high redshift [OII] luminosity functions. The local SDSS [OII] luminosity function does not exhibit such a turnover, however it is likely that the sample does not reach [OII] luminosities faint enough to see it. There is also a potentially observed evolution in the faint-end slopes of the high redshift [OII] luminosity functions. The ROLES75 [OII] LF error bars are large and do not constrain the faint-end fit, therefore this is considered a weak observation in need of further study. The faint-end slopes, in increasing order of redshift, are $\alpha(0.75) = -1.25$, $\alpha(0.84) = -1.3$ (Zhu, Moustakas & Blanton, 2009), and $\alpha(1.0) = -1.5$ (Gilbank et al., 2010b). Most importantly ROLES75 has determined that the [OII] luminosity function at $z \sim 0.75$ is not influenced by environment. Figure 5.5 shows that the bright and faint-end slopes of each of the structure and field populations are consistent with each other given the error bars. It is the comparable shapes of the [OII] luminosity functions in these distinct density environments, not the normalization, which implies that the [OII] luminosities of star forming galaxies are not influenced by the local density in which they reside.

[OII] Luminous Galaxy Stellar Mass Function

The [OII] luminous star forming galaxy stellar mass function (combined SF-GSMF) was presented in §5.3 in Figure 5.7, while the ROLES75 SF-GSMF segregated by environment is shown in Figure 5.8. The combined SF-GSMF further verified the results from ROLES1 - there is little, if any evolution in the galaxy stellar mass function of [OII] luminous galaxies since a redshift of $z \sim 2.75$ for stellar masses of $M^* > 10^{9.3} M_\odot$. This is clearly shown in Figure 5.7 where the ROLES75 combined SF-GSMF shape *and* normalization are consistent with the SF-GSMFs of the local SDSS sample, the ROLES1 population, and the high redshift / high mass comparison samples. There is a weak suggestion of an environmentally dependent 'upturn' in the field population near $M^* \sim 10^9 M_\odot$ which is not strongly apparent in the structure population. This may be weak evidence of a bi-modal GSMF in the CDFS sample. In this case, a bi-modal GSMF refers to the combination of two separate mass functions. One would dominate at the high mass end and belong to a population of large central star forming galaxies, while the other would correspond to a population of star forming satellite galaxies which dominate in the low stellar mass domain. The 'upturn' which is present in the field SF-GSMF sample of Figure 5.8 would correspond to the stellar mass threshold where the satellite field galaxies begin to dominate the structure SF-GSMF. However, the upturn also appears in the FIRES cluster SF-GSMF which would then refute the idea of a bi-modal GSMF being evident in the ROLES75 populations. Clearly this observation is in need of further study. In the high

mass end of Figure 5.8 the structure SF-GSMF is distinctly different in shape than the corresponding stellar mass range of the field population. This is attributed to the presence of large sale structure found in the CDFS field within the redshift limits covered by ROLES75.

Star Formation Rate Density
Figure 5.9 of §5.4 presents the ROLES75 star formation rate density at $z \sim 0.75$ compared with the ROLES1 SFRD results which are divided into the CDFS, FIRES, GDDS, and FORS2 fields. Also shown are results from Juneau et al. (2005) for the present day SFRD and for $z \gtrsim 1$. The GDDS and FORS2 SFRD points are meant to extend the ROLES1 SFRD (CDFS,FIRES) to higher stellar masses. ROLES75 shows the higher mass FORS2 sample already combined with the CDFS and FIRES samples. The idea of a constant scale factor applicable to the local SDSS SFRD to attain the ROLES1 SFRD is not confirmed for ROLES75. In the low mass end of the ROLES75 SFRD there is a weak suggestion that such a scale factor may be applicable. However in the high stellar mass end, the ROLES75 SFRD is lower than would be expected based upon the application of such a scale factor. The high mass end of the SFRD is dominated by the FORS2 sample, which has been corrected for incompleteness and volume (using V_{max}), however there may be an additional correction which is unaccounted for, and which causes the SFRD to be lower than expected. One possibility is that the effect of extinction for these higher mass galaxies has been underestimated. A larger extinction correction would increase the SFRD, shift the bright-end of the [OII] luminosity function to higher [OII] luminosities (reducing the offset mentioned earlier), and increase the sSFR in the high mass end. All of these adjustments would improve the consistency of the ROLES75 population with the ROLES1 comparison samples.

The environment is highly influential in the high stellar mass end with the SFRD of the structure population being much larger than its field couterpart (see Figure 5.10). This is attributed to the difference in the shapes of their respective galaxy stellar mass functions rather than a high density environment causing the galaxy star formation rates to be enhanced. At the low mass end the two populations are consistent with one another.

In the total star forming SFRD versus redshift plot of Figure 5.11 the location of the ROLES75 binned SFRD value is consistent with the observed trend where the SFRD increases with decreasing stellar mass for a given redshift. Similarly, the SFRD decreases with decreasing redshift for a given stellar mass range.

Specific Star Formation Rate
The trend of a decreasing specific star formation rate with increasing stellar mass has been

confirmed using the star forming population of ROLES75, as shown in Figure 5.12 of §5.5. The $sSFR - M^*$ normalizations between the ROLES1, ROLES75, and the color-cut local SDSS samples are different but their shapes are comparable in the high stellar mass range. In the low stellar mass end, the observation of an 'upturn' confirms the same observation in ROLES1. This upturn is clearly not present in the local SDSS sample (see Figure 5.12).

Kolmogorov-Smirnov tests have verified that there is no indication that the presence of a high or low density local environment (structure or field, see Figures 5.13 and 5.14) influences the specific star formation rate of galaxies at $z \sim 0.75$.

The more interesting and tantalizing result is presented in Figure 5.15 where the ROLES75 $sSFR - M^*$ relation, divided into the low density field and high density structure populations, has been compared with the similar density segregated results at $z \sim 1$ and at present time. There is certainly an increase in the sSFR toward higher redshifts with decreasing stellar mass. However the observation which is the most exciting is the presence of a turnover effect of the sSFR dominant density regime as a function of redshift. At a redshift of $z \sim 1$ the $sSFR - M^*$ curve for the high density population lies above its low density counterpart across the stellar mass range they share in common. Oppositely, at present day the $sSFR - M^*$ curve of the high density population has shifted to a lower sSFR regime, with the low density $sSFR - M^*$ dominant across the stellar mass range they mutually explore. Perhaps coincidentally, at $z \sim 0.75$ explored by this work, the $sSFR - M^*$ curve for the high density structure population is consistent with the low density field $sSFR - M^*$ curve, with each overlapping. The prospect of detecting a critical evolutionary turnover is attractive, however given the difference in definitions of high and low density environments for the ROLES75 and ROLES1/SDSS samples, we must caution that this result is in further need of study.

The results of this work, highlighted in the previous sections, provide valuable insights into the processes governing galaxy formation at a redshift of $z \sim 0.75$. We find that galaxies which are evolving in high density environments (defined here as regions of known structure) will have their stellar mass functions modified according to the stellar mass distribution of the galaxies present in this high density environment, confirming the studies mentioned in the Introduction. This in turn correlates with the star formation rate density function observed for the same galaxies which are forming in a high density environment. However, neither the [OII] luminosity function nor the specific star formation rate of active galaxies are driven by the density of the local environment.

Plans are underway to extend the ROLES survey to a higher redshift of $z \sim 1.45$ in an effort to determine if the galaxy formation trends observed in the redshift range of

$0.62 < z < 1.15$ for dwarf galaxies continue out to higher redshift toward the critical epoch of galaxy formation at $z \sim 2$. The same observation strategy and analysis techniques would be employed, however a deep field with extensive multi-band photometry is necessary to determine stellar masses using SED fitting techniques. One such well studied field chosen for follow-up study is the UKIDSS-UDS in the northern hemisphere, for which we have been awarded ten hours of time at Gemini North to observe. This should be sufficient exposure time to prove the ROLES techniques at this higher redshift. Provided this testing concludes favorably, more time will be requested by the ROLES collaboration which hopes to explore the evolution of star forming galaxies and the role of environment during the epoch of galaxy formation at $z \sim 2$

The goal of this study was to address the issues and questions posed in the Introduction. Specifically, how does galaxy formation and evolution present itself overall in the low stellar mass regime of dwarf galaxies, which is not well understood in the mid-to-high redshift range. Also, what influence does the presence of an under- or overdense environment have on the formation and evolution of the low mass galaxies that reside within it? Some answers to these questions have been provided by the ROLES75 survey in the previous sections of this thesis. However the picture is far from complete. Further surveys which specifically target low mass galaxies residing in under and overdense environments are required as ROLES75 has only sampled a small fraction of the redshift and space volume required to address the issues of environmentally driven galaxy formation.

References

Abraham R. G., Glazebrook K., McCarthy P. J., Crampton D., Murowinski R., et al., 2004, The Astronomical Journal, 127, 2455

Arnouts S., Cristiani S., Moscardini L., Matarrese S., Lucchin F., Fontana A., Giallongo E., 1999, Monthly Notices of the Royal Astronomical Society, 310, 540 79

Baldry I. K., Glazebrook K., 2003, The Astrophysical Journal, 593, 258 57, 79

Baldry I. K., Glazebrook K., Driver S. P., 2008, Monthly Notices of the Royal Astronomical Society, 388, 945

Bauer A. E., Conselice C. J., Perez-Gonzalez P. G., Grutzbauch R., et al., 2011, arXiv Astrophysics e-print

Benson A. J., 2010, Physics Reports, 495, 33 2

Blanton M. R., Roweis S., 2007, The Astronomical Journal, 133, 734 80

Blumenthal G. R., Faber S. M., Primack J. R., Rees M. J., 1984, Nature, 311, 517 1

Bohlin R., Lindler D., 1992, Space Telescope Science Institute Newsletter, 9, 19 39

Bolzonella M., Kovac K., Pozzetti L., Zucca E., et al., 2010, Astronomy & Astrophysics, 524 5, 67

Bolzonella M., Miralles J., Pelló R., 2000, Astronomy & Astrophysics, 363, 476 78

Bouché N., Dekel A., Genzel R., et al., 2010, The Astrophysical Journal, 718, 1001 102

Boyle B. J., Terlevich R. J., 1998, Monthly Notices of the Royal Astronomical Society, 293, 49 102

Brinchmann J., Charlot S., White S. D. M., Tremonti C., Kauffmann G., Heckman T., Brinkmann J., 2004, Monthly Notices of the Royal Astronomical Society, 351, 1151 85, 94

Bruzual G., Charlot S., 2003, Monthly Notices of the Royal Astronomical Society, 344, 1000 79, 80

Bundy K., Ellis R. S., Conselice C. J., 2005, The Astrophysical Journal, 625, 621 103

Bundy K., Ellis R. S., Conselice C. J., Taylor J. E., Cooper M. C., et al., 2006, The Astrophysical Journal, 651, 120 3, 103

Calzetti D., Armus L., Bohlin R. C., Kinney A. L., et al., 2000, The Astrophysical Journal, 533, 682 79, 80

Cassata P., Giavalisco M., Guo Y., Renzini A., Ferguson H., et al., 2011, arXiv Astrophysics e-print

Chabrier G., 2003, Publications of the Astronomical Society of the Pacific, 115, 763 79

Chuter R. W., Almaini O., Hartley W. G., McLure R. J., et al., 2011, Monthly Notices of the Royal Astronomical Society, 413, 1678

Coelho P., Bruzual G., Charlot S., et al., 2007, Monthly Notices of the Royal Astronomical Society, 382, 498 80

Conselice C. J., Bundy K., Trujillo I., Coil A., Eisenhardt P., Ellis R. S., et al., 2007, Monthly Notices of the Royal Astronomical Society, 381, 962

Cowie L. L., Barger A. J., 2008, The Astrophysical Journal, 686, 72 2

Cowie L. L., Songaila A., Hu E. M., Cohen J. G., 1996, The Astronomical Journal, 112, 839 109

Crawford S. M., Wirth G. D., Bershady M. A., Hon K., 2011, arXiv Astrophysics e-print 10, 51, 55

Croton D. J., Farrar G. R., Norberg P., Colless M., et al., 2005, Monthly Notices of the Royal Astronomical Society, 356, 1155

Daddi E., Cimatti A., et al., 2004, The Astrophysical Journal, 617, 746 104

Damen M., Labbe I., Franx M., van Dokkum P. G., Taylor E. N., Gawiser E. J., 2009, ApJ, 690, 937 3

Davies G. T., Gilbank D. G., Glazebrook K., Bower R. G., et al., 2009, Monthly Notices of the Royal Astronomical Society Letters, 395, 76 7

Davis M., 2003, Proceedings of SPIE, 4834, 161 73

Demarco R., Gobat R., Rosati P., Lidman C., Rettura A., et al., 2010, The Astrophysical Journal, 725, 1252

Drory N., Bundy K., Leauthaud A., Scoville N., et al., 2009, The Astrophysical Journal, 707, 1595 5, 78, 79, 80, 81, 83, 84, 89

Dutton A. A., van den Bosch F. C., Dekel A., 2010, Monthly Notices of the Royal Astronomical Society, 405, 1690

Elbaz D., Daddi E., Le Borgne D., et al., 2007, Astronomy & Astrophysics, 468, 33 94

Ellis R. S., Colless M., Broadhurst T., Heyl J., Glazebrook K., 1996, Monthly Notices of the Royal Astronomical Society, 280, 235

Fasano G., Marmo C., Varela J., et al., 2006, Astronomy & Astrophysics, 445, 805

Fioc M., Rocca-Volmerange B., 1997, Astronomy & Astrophysics, 326, 950 56

Fontanot F., Lucia G. D., Monaco P., Somerville R. S., Santini P., 2009, Monthly Notices of the Royal Astronomical Society, 397, 1776 109

Förster Schreiber N. M. et al., 2006, The Astronomical Journal, 131, 1891 9, 10, 56, 67

Gallagher J., Bushouse H., Hunter D., 1989, The Astronomical Journal, 97, 700 7

Gallego J., García-Dabó C., Zamorano J., Aragón-Salamanca A., Rego M., 2002, The Astrophysical Journal, 570, 1

Gallego J., Zamorano J., Rego M., Alonso O., Vitores A. G., 1996, Astrophysical Journal Supplement Series., 120, 323

Gehrels N., 1986, The Astronomical Journal, 303, 336 72

Gilbank D. G., Baldry I. K., Balogh M. L., Glazebrook K., Bower R. G., 2010a, Monthly Notices of the Royal Astronomical Society, 405, 2594 7, 8, 57, 109

Gilbank D. G. et al., 2011, Monthly Notices of the Royal Astronomical Society, 414, 304 7, 8, 78, 79, 80, 92, 94, 109, 110

Gilbank D. G., et al., 2010b, Monthly Notices of the Royal Astronomical Society, 405, 2419 7, 8, 9, 10, 28, 73, 74, 76, 85, 86, 102, 109, 111

Gilli R., Cimatti A., Daddi E., Hasinger G., Rosati P., et al., 2003, The Astrophysical Journal, 592, 721 67

Glazebrook K. et al., 2004, Nature, 430, 181 56

Glazebrook K., Bland-Hawthorn J., 2001, Publications of the Astronomical Society of the Pacific, 113, 197 10

González V., Labbé I., Bouwens R. J., Illingworth G., Franx M., Kriek M., Brammer G. B., 2010, The Astrophysical Journal, 713, 115 3

Haas M., 2010, Thesis, `http://www.marcelhaas.com/thesis/`

Hamuy M., 1994, Publications of the Astronomical Society of the Pacific, 106, 566 39

Hogg D., 1999, arXiv Astrophysics e-print 64

Hogg D., Cohen J., Blandford R., et al., 1998, The Astrophysical Journal, 504, 622

Hopkins A. M., 2004, The Astrophysical Journal, 615, 209 89

Hopkins A. M., Beacom J. F., 2006, The Astrophysical Journal, 651, 142 3, 102

Ilbert O., Arnouts S., McCracken H. J., Bolzonella M., Bertin E., et al., 2006, Astronomy & Astrophysics, 457, 841 79

Ilbert O., Capak P., Salvato M., Aussel H., et al., 2009, The Astrophysical Journal, 690, 1236 80

Ilbert O., Salvato M., Floc'h E. L., Aussel H., Capak P., et al., 2010, The Astrophysical Journal, 709, 644

Juneau S. et al., 2005, The Astrophysical Journal, 619, 135 57, 85, 86, 87, 89, 90, 91, 93, 112

Karim A., Schinnere E., Martinez-Sansigre A., Sargent M. T., et al., 2011, The Astronomical Journal, 730, 730

Kennicutt R. C., 1983a, The Astrophysical Journal, 272, 54 6

Kennicutt R. C., 1983b, The Astronomical Journal, 88, 1094 6

Kennicutt R. C., 1992, The Astrophysical Journal, 388, 310 6

Kennicutt R. C., 1998, Annual Review of Astronomy and Astrophysics, 36, 189 7, 57

Kewley L. J., Geller M. J., Jansen R. A., 2004, The Astronomical Journal, 127, 2002 6

Khochfar S., Silk J., 2011, Monthly Notices of the Royal Astronomical Society: Letters, 410, 42 3

Lawrence A., Warren S., Almaini O., et al., 2007, Monthly Notices of the Royal Astronomical Society, 379, 1599 104

Le Fèvre O., Vettolani G., Paltani S., Tresse L., et al., 2004, Astronomy & Astrophysics, 428, 1043 67

Li I. H. et al., 2011, Monthly Notices of the Royal Astronomical Society, 411, 1869 7, 8, 97, 99, 100, 109

Lilly S. J., Le Fevre O., Renzini A., Zamorani G., Scodeggio M., et al., 2007, The Astrophysical Journal Supplement Series, 172, 70 78

Maier C., Lilly S. J., Zamorani G., Scodeggio M., et al., 2009, The Astrophysical Journal, 694, 1099

Mannucci F., Cresci G., Maiolino R., Marconi A., Gnerucci A., 2010, Monthly Notices of the Royal Astronomical Society, 408, 2115

Maraston C., 2005, Monthly Notices of the Royal Astronomical Society, 362, 799 79

Marchesini D., van Dokkum P. G., Frster Schreiber N. M., et al., 2009, ApJ, 701, 1765 3

McCarthy P. J., Carlberg R. G., Chen H.-W., Marzke R. O., Firth A. E., Ellis R. S., et al., 2001, The Astrophysical Journal, 560, 131

Mobasher B. et al., 2009, Astrophysical Journal, 690, 1074 9

Moresco M., Jimenez R., Cimatti A., Pozzetti L., 2011, Journal of Cosmology and Astroparticle Physics, 2011, 45

Mortlock A., Conselice C. J., Bluck A. F. L., Bauer A. E., et al., 2011, Monthly Notices of the Royal Astronomical Society, 413, 2845

Noeske K. G., Weiner B. J., Faber S. M., Papovich C., Koo D. C., et al., 2007, The Astrophysical Journal, 660, 43

Oke J., 1990, The Astronomical Journal, 99, 1621 39

Peng Y., Lilly S. J., Kovac K., Bolzonella M., Pozzetti L., et al., 2010, The Astrophysical Journal, 721, 193 3, 67, 78, 79, 80, 81, 82, 83

Peng Y., Lilly S. J., Renzini A., Carollo M., 2011, arXiv Astrophysics e-print 3, 5, 83, 84

Pilyugin L. S., Thuan T. X., 2011, Astrophysical Journal Letters, 726, 23

Popesso P., Rodighiero G., Saintonge A., et al., 2011, Astronomy & Astrophysics, 532, 145 67, 94

Pozzetti L., Bolzonella M., Lamareille F., Zamorani G., Franzetti P., et al., 2007, Astronomy & Astrophysics, 474, 443 78

Pozzetti L., Bolzonella M., Zucca E., Zamorani G., Lilly S., et al., 2009, The Astrophysical Journal, 184, 218 3, 78, 79, 80, 81

Quadri R. F., Williams R. J., Franx M., Hildebrandt H., 2011, arXiv Astrophysics e-print

Ravikumar C. D., Puech M., Flores H., Proust D., et al., 2006, arXiv Astrophysics e-print 67

Reddy N. A., Steidel C. C., 2009, The Astrophysical Journal, 692, 778

Rettura A., Mei S., Stanford S. A., Raichoor A., Moran S., et al., 2011, The Astrophysical Journal, 732, 94

RosaGonźalez D., Terlevich E., Terlevich R., 2002, Monthly Notices of the Royal Astronomical Society, 332, 283 7

Salpeter E. E., 1955, The Astrophysical Journal, 121, 161 57, 79

Sánchez H. D., Pozzi F., Gruppioni C., Cimatti A., Ilbert O., et al., 2011, Monthly Notices of the Royal Astronomical Society 78, 79, 80, 81

Sawicki M., Thompson D., 2006, The Astrophysical Journal, 642, 653

Sobral D., Best P., Smail I., Geach J., Cirasuolo M., Garn T., Dalton G. B., 2011, Monthly Notices of the Royal Astronomical Society, 411, 675

Somerville R. S., Lee K., Ferguson H. C., et al., 2004, The Astrophysical Journal, 600, 171

Straughn A. N., Kuntschner H., Kuemmel M., Walsh J. R., et al., 2011, The Astronomical Journal, 141, 14

Vanzella E. et al., 2008, Astronomy & Astrophysics, 478, 83 48, 64

Vanzella E., Cristiani S., Dickinson M., Kuntschner H., et al., 2005, Astronomy & Astrophysics, 434, 53 67

Villar V., Gallego J., Prez-Gonzlez P.-G., Barro G., et al., 2011, arXiv Astrophysics e-print

Vulcani B., Poggianti B. M., Aragón-Salamanca A., Fasano G., et al., 2011, Monthly Notices of the Royal Astronomical Society, 412, 246

White S. D. M., Clowe D. I., Simard L., Rudnick G., et al., 2005, Astronomy & Astrophysics, 444, 365

Wuyts S., Labb I., Förster Schreiber N. M., Franx M., Rudnick G., Brammer G. B., van Dokkum P. G., 2008, Astrophysical Journal, 682, 985 10, 44, 51, 56

Wuyts S., Schreiber N. M. F., Lutz D., et al., 2011, arXiv Astrophysics e-print 2

Zamorano J., Gallego J., Rego M., Vitores A. G., Alonso O., 1996, Astrophysical Journal Supplement Series., 105, 343

Zamorano J., Rego M., Gallego J. G., Vitores A. G., Gonzalez-Riestra R., Rodriguez-Caderot G., 1994, Astrophysical Journal Supplement Series., 95, 387

Zheng X. Z., Bell E. F., Papovich C., Wolf C., Meisenheimer K., et al., 2007, The Astrophysical Journal, 661, 41

Zhu G., Moustakas J., Blanton M. R., 2009, The Astrophysical Journal, 701, 86 72, 73, 74, 76, 111